Crashworthiness of Filament Wound CFRP Origami Tubes

James O'Neil

A dissertation
submitted in partial fulfillment of the
requirements for the degree of Aeronautics and Astronautics

Doctor of Philosophy

University of Washington

2024

Reading Committee:
Marco Salviato, Chair
Jinkyu Yang
Eunho Kim
Ed Habtour
Aniruddh Vashisth
Amir Taghvaei

Program Authorized to Offer Degree:
Aeronautics and Astronautics

University of Washington

Abstract

Crashworthiness of Filament Wound CFRP Origami Tubes

James O'Neil

Chair of the Supervisory Committee:
Professor Marco Salviato
Aeronautics and Astronautics

In recent years, the crashworthiness of thin-walled volumetric origami architectures have studied extensively as they have been found to provide more stable and progressive collapse modes compared with traditional straight-walled tubes. They can also dissipate similar levels of energy absorption per mass. Therefore, pre-folded origami tubes show great potential as crash boxes. They can be improved further by coupling them with composites which possess weight saving advantages over metals. The brittle failure of composites, which is not always conducive to improved energy absorption, can be improved with origami creases. However, the corrugated shapes are challenging to manufacture and current fabrication methods employ stamping and/or vacuum bagging which cannot be easily implemented on industrial scales.

In this work, we consider utilizing the Kresling origami architecture which possesses creases that can guide a smooth coupled axial-twisting collapse in its unit cells. We begin by detailing a novel filament winding method for efficient fabrication of these tubes from carbon fiber reinforced plastics (CFRPs). Second, we explore the quasi-static compressive behavior of the tubes by developing a finite element model that is calibrated using experimental data. A parametric analysis is conducted with an experimentally verified model to determine which geometric parameters are important to tune for superior crashworthiness to straight-walled cylinders.

As an extension of our parametric study, we will explore the compressive behavior of concave cylinders that are derived from Kresling origami unit cells when the number of sides are allowed to approach infinity. We slightly modify our manufacturing approach for these cylinders and compare their energy absorption capabilities with that of straight-walled cylinders.

Finally, we numerically and experimentally demonstrate the ability of CFRP Kresling origami tubes to provide a more stable collapse compared to straight-walled tubes while absorbing comparable amounts of energy per mass in the quasi-static collapse case. This requires a non-uniform unit cell geometry configuration. We only consider the quasi-static case due to limitations with our impact tester. We will confirm that this geometry can maintain its progressive cascading collapse under dynamic loading conditions to validate the superior crashworthiness of these composite Kresling origami tubes. With improved manufacturing, we believe our Kresling origami crash boxes can improve further and be utilized for industrial applications.

TABLE OF CONTENTS

Page

LIST OF FIGURES

Figure Number Page

LIST OF TABLES

ACKNOWLEDGMENTS

To begin, I would like to sincerely thank Professor Jinkyu Yang, my original advisor, for providing me the opportunity and academic freedom to pursue this research. He provided invaluable advice and guidance throughout not just this research, but my entire graduate career. I could not have completed this thesis without his support and generosity. I would also like to show my sincere appreciation for my current advisor, Professor Marco Salviato, who took up the task of my advisement in my final year and is the reason I was awarded the Geda and Phil Condit Endowed Graduate Fellowship. He guided much of my research with his expertise in the field of composites and crashworthiness. Furthermore, I thank my committee members, Professor Ed Habtour, Professor Jeffrey Lipton, Professor Amir Taghvaei, and Professor Aniruddh Vashisth for their insights and comments on my research.

I would like to show immense gratitude for Professor Eunho Kim (Jeonbuk National University and a committee member) who was instrumental toward my research efforts. His expert knowledge in composites and his assistance in my dynamic experiments were paramount to my success. I must also thank Dr. Antonio Deleo and Dr. Hiromi Yasuda for their mentorship and guidance in the early years of my graduate career. Bill Kuykendall, one of UW ME's lab engineers, trained me on the equipment for my experiments and assisted me in setting them up and I would like to sincerely thank him for that.

Finally, I would like to express my gratitude to the current and past members of the Laboratory for Engineered Materials and Structures (LEMS) for their friendship, support, and helpful comments.

DEDICATION

To my parents, siblings, nephews, niece, and my girlfriend, Jessica.

Chapter 1

INTRODUCTION

1.1 Background

Crash boxes are thin-walled structures that are utilized on vehicles for two purposes: 1. Redirect kinetic energy during collision away from the passenger by converting it into plastic strain energy or fracture and 2. Increase the collision time, thereby reducing the average forces transferred to the passengers based on the concept of impulse. [1, 2]. Traditionally, they have straight-walled designs and are manufactured from metals to form a "crumple zone" during collisions. Conventional straight-wall designs are simplistic and relatively simple to manufacture, hence why they were some of the first geometries considered for crash boxes. In earlier studies related to crashworthiness, a theory to predict the mean axial crushing force of cylindrical tubes was derived by Alexander [3] assuming a simple collapse mode. This was followed by derivations from Abramowicz, Wierzbicki, and Jones to calculate the mean axial crushing force of square tubes [4, 5]. There have been investigations into straight-walled tubes with differing polygonal cross sections [6] and tapered straight-walled tubes [7, 8] but the circular and square tube are treated in many studies as control geometries in which new designs are compared.

Many early studies focused on the fabrication of these tubes from metals. However, the use of composites in crashworthiness designs and therefore conventional tubes has been popular for decades [9]. Composites can offer higher strength-to-weight and stiffness-to-weight ratios compared to metals [10]. Composites also enable more design flexibility allowing designers to choose the materials of the fibers and matrix and the layup sequence of the composite. Therefore, composites can potentially provide superior specific energy absorption capabilities over metals [11]. Also, they can bring down the mass of vehicles which improves cost effectiveness and fuel economy. Metal tubes crush axially in the form of buckling and/or folding of the thin-walls which leads to significant energy absorption through extensive plastic deformation [12]. In contrast, composite tubes can progressively dissipate crushing energy through either unstable collapse modes characterized by extensive quasibrittle fracture or stable modes similar to metal tubes [12, 13]. The stable mode can be observed through careful selection of the tube's materials and geometry [14, 15]. Regardless of whether they are constructed from metal or composites, the axial crushing behavior of straight-walled cylinders is usually characterized by the following: a relatively high initial peak force and large force fluctuations in the force-displacement curve [16]. This represents a large deceleration followed by a potentially unstable collapse which may not be the safest mitigation strategy for passengers. Additionally, the weight-savings benefits of composite materials can be difficult to fully realize as straight-walled composite tubes can demonstrate significant brittle fracture leading to large load oscillations. This implies the inefficiency of the straight-walled tubes in their energy absorption performances.

Geometrical modifications can be made to conventional tubes to improve their energy absorption capabilities. This can include the introduction of stress concentrations at the edge of a thin-walled tube which are known as triggers. Triggers prevent direct load transfer to a structure by localizing initial failure at the edges resulting in progressive damage [17]. Another modification comes in the form of the corrugated thin-walled structure of which there are three kinds: Periodic Corrugated, Pre-Folded, and Grooved [18]. The class of corrugated structures we will focus on in this thesis are the Pre-Folded tubes or tubes that are constructed with origami patterns as they can induce highly favorable progressive deformation modes for increased energy absorption and force response when compared to conventional tubes [19]. The creases of these tubes act as geometric imperfections which reduce the initial peak forces while increasing its relative magnitude to the mean force of the collapse, resulting in a smoother collapse under compression. The creases can be designed to guide the collapse of the tubes into highly favorable progressive deformation modes which can provide superior energy absorption when compared to straight-walled geometries. This improves the safety of the crash box for passengers. Thorough work has been conducted on modifying square tubes so that they include pre-folded origami patterns which improve the energy absorption capabilities of the tubes by inducing a full diamond mode [19]. The full diamond mode is a non-symmetrical deformation mode that is desirable for pre-folded tubes that exhibit a relatively low initial peak force and high mean crushing force. Kite-shaped origami patterns can also produce thin-walled tubes with smooth reaction forces and improved energy absorption capabilities compared to conventional tubes [20, 21]. Kirigami variations have also been considered [22]. All of these works focused on metal or in some cases polymer [23, 24] pre-folded tubes.

Just as straight-walled tubes have been combined recently with composites in order to exploit the weight-savings advantages of composites [9], so too, have origami tube designs. Ye *et al.* fabricated a composite-walled Yoshimura tube for experimental verification of their numerical model [25] and found that not only could it outperform a numerically tested cylinder, it had superior energy absorption per mass compared with a metal counterpart. Ciampaglia *et al.* [26] fabricated an origami tube from composites using a 3D printed sacrificial mold that could be dissolved after curing of the composite walls. They explored the response of the origami tube both numerically and experimentally under axial impact and determined that it could reduce the initial peak force when compared to conventional square tubes. If optimized properly, it could also absorb about 10% more energy. Song *et al.* proposed a metal-composite hybrid diamond origami tube which improved on the energy absorption behavior of the tubes with strictly metal or strictly composite walls [27]. Researchers observed that using origami patterns can act as effective triggers for improving the energy absorption behavior of straight-walled metal-composite hybrid tubes [28]. These previous studies have reported numerically and/or experimentally that composite pre-folded tubes can outperform straight-walled tubes if their geometries are properly tuned. Load oscillations due to brittle fracture can be mitigated as well with pre-folded geometries.

A common limitation of pre-folded tubes, is that their manufacturing processes can be difficult to automate and implement on industrial scales. Pre-folded tubes with metal materials tend to use molds to stamp and generate one half of the tubes followed by welding [29] or mechanical fasteners [30] to join the halves together. This increases manufacturing complexity and cost, though it can be partly mitigated through the use of 3D printing [31]. However, these methods are time-consuming, and using metals means that we can only utilize the geometry of the origami to obtain advantages over straight-walled tubes. To be constructed from composites, pre-folded designs usually require either multiple dies [25], dissolvable 3D printed molds [26], or some other equipment that allows the composite walls to conform to the origami shape through applied pressure. This can include vacuum bagging or stamping. In order to get around this manufacturing limitation, we look to a different origami architecture: The Kresling origami fold pattern.

The Kresling origami architecture has received significant attention in recent years due to its unique coupled axial compression and twist rotation that was first observed in the buckling of cylinders subjected to axial compression and torsion [32]. Therefore, axial deformation is coupled with twisting motion in the unit cells (see Figure 1.1. During compression, the facets of Kresling origami tubes experience facet bending and folding along their creases, unlike rigid-foldable tubes which only experience deformation along their creases ideally [33]. Therefore, Kresling origami provides additional avenues for energy dissipation through its facets. The twist of the facets provides an efficient solution for careful guiding of the deformation under compression. The foldable compressive behavior of Kresling origami has been studied extensively [34, 35, 36] and it has been found that its geometric parameters offer a large design space that allows tunability of the stiffness [37, 38] and multi-stability of the collapse [39]. Kresling's tunability has been effectively utilized to generate rarefaction waves [40] under low-speed impacts. The multi-stability of the architecture has been employed for purposes of deployability [41, 42, 43] and mechanical memory [44]. Other investigations have looked into the chaotic dynamic behavior of Kresling as well as the effects of perforations on its creases [40, 45]. The fatigue behavior of a foldable antenna with the Kresling pattern has also been considered [46]. In terms of Kresling origami being used as an energy absorption device, the work done by Professor Hagiwara's research group has shown the effectiveness of metal thin-walled Kresling origami with unit cells that have alternating chirality in the tube. Wu *et al.* was one of the first groups to study the crushing behavior of Kresling tubes and even developed a model to smooth the surface of the tube using an interpolation and approximation subdivision scheme to make it more manufacturable [47, 48]. It was demonstrated that the tube produced with the interpolation scheme performed similarly to the original Kresling design. Subdivision methods were used again in Zhao *et al.* [49] to find an optimal geometry for a Kresling tube and to improve its characteristics over a conventional square tube. The optimization provided the group with a Kresling tube with a reduced initial peak load and reduced weight which absorbed 1.91 times the energy of the square tube. This paper presented a prototype for the tube formed from hydro forming. Li *et al.* conducted a computational parametric study on metal Kresling origami tubes and showed that the alternating chirality pattern absorbs slightly more energy than a Kresling tube with uniform chirality [50]. Additionally, the study observed the TCO tubes had a decreased initial peak force and mean force compared with their straight-walled counterparts and that reducing the twist in the tubes increased the total energy absorption. Increasing the number of sides of Kresling origami tubes for certain twist angles could improve the energy absorption capability of the tubes as well. Despite these interesting findings, Kresling origami tubes with isotropic materials for crash box applications is also very difficult to manufacture. A hydro forming manufacturing process was fully described in Kong *et al.* [51]. In order to avoid fracturing the tube during the hydro forming process, local thickening was introduced in certain creases in the tube. It was shown that this can increase the energy absorption of the tube. However, Zhao and Hagiwara [52] presented a torsion-forming method that is cheaper and produces metal Kresling tubes with more energy absorption than Kresling tubes fabricated from the hydro forming method.

It is at this point that we highlight the contributions of this thesis. Kresling origami has been shown to potentially have superior crashworthiness to straight-walled tubes but its manufacturing with metals is difficult. To get around this limitation, we propose fabricating the Kresling origami tubes with composite materials as they do have convex regions which

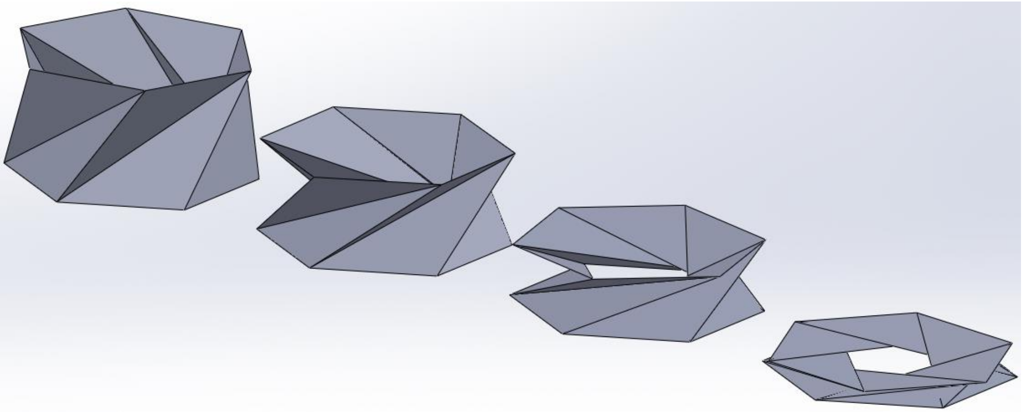

Figure 1.1: The Kresling origami unit cell.

are necessary for filament winding processes.

1.2 Purpose of this Thesis

In this thesis, we propose utilizing the Kresling origami architecture to efficiently manufacture corrugated thin-walled carbon fiber reinforced plastic (CFRP) crash box tubes and assess their crashworthiness. We present a novel manufacturing method for filament-wound CFRP Kresling origami thin-walled tubes and assess their crashworthiness. These tubes maintain uniform chirality throughout their length which provides convex regions resulting in filament winding being a feasible method for their fabrication. The goal is to improve on the energy absorption behavior of straight-walled tubes while providing a less brittle and more progressive collapse. The organization of the thesis is as follows: Chapter 2 details the manufacturing process of these tubes and studies their energy absorption performance through quasi-static compression tests. These experiments are used in this chapter to develop a finite element model capable of predicting important qualitative trends in the crushing behavior of the tubes. Chapter 3 will see a refinement of this model as it will be able to account for an excess resin imperfection that we did not account for in Chapter 2. The model will be experimentally verified and a parametric study exploring the effects of geometric variables on the crashworthiness of the Kresling origami tubes. The results are utilized to determine which geometric variables are important for considerably improving the energy absorption capabilities of the tubes in order to outperform straight-walled cylinders. Chapter 4 will act as an extension of our parametric study. As the number of sides of the Kresling origami tubes' cross-section approaches infinity, concave cylinders can be derived with their own unique curvature. We will explore their compressive behavior and determine their suitability for crash applications. In Chapter 5, we will propose a Kresling origami geometric configuration that not only outperforms a straight-walled cylinder in terms of energy absorption, but it can also demonstrate progressive collapse under dynamic loading conditions. This is important as we will have confirmation on the crashworthiness of the CFRP Kresling origami tubes. Finally, we will provide concluding remarks and potential future work in Chapter 6.

Chapter 2

FILAMENT WINDING METHOD FOR MANUFACTURING CFRP KRESLING ORIGAMI TUBES

In this chapter, we present a novel manufacturing method for filament-wound CFRP (carbon fiber reinforced plastic) Kresling origami thin-walled tubes. Our Kresling origami tubes have unit cells with uniform chirality, so filament winding is a feasible method for their fabrication. Based on the filament wound composite tubes fabricated in the Kresling pattern, we conduct compression tests to assess their energy absorption performance. We note in passing that previous studies have focused more on numerical investigations with metals forming the walls of the tubes, instead of experimental verifications on composite origami tubes [49, 53, 50]. One of the goals of energy absorbing thin-walled tubes should be to provide satisfactory load uniformity and to provide a predictable and stable performance [19]. A sacrifice of the layup sequence used is that the fibers are not oriented in the direction of loading. Nonetheless, we experimentally show that our composite Kresling origami tubes can meet these goals under axial quasi-static crushing due to their twisted geometry. We also verify the performance of our composite Kresling origami tubes by using a finite element model that can reproduce important experimental quasi-static trends observed in the prototypes tested.

Compared to the previous works about the energy absorption of structures with origami patterns including the Kresling pattern, the highlight of this study is as follows. First, we developed a novel filament winding fabrication process for CFRP origami tubes pre-folded specifically in the Kresling pattern. As mentioned previously, filament winding provides the potential for automation and therefore manufacturability for industrial scales. Second, we acquired the experimental data on the CFRP Kresling origami tubes for crashworthiness applications, which is in contrast to previous studies that primarily focused on numerical investigations with metals forming the walls of the tubes. The final highlight is the verification of the improved crushing efficiency of the Kresling tubes – particularly in terms of the mean force divided by the initial peak crushing force – compared with straight-walled configurations.

2.1 Geometrical Definitions

Two perspectives of a Kresling origami unit cell are shown in Figure 2.1. The unit cell height H_{unit} is defined in Figure 2.1a. The circumscribed radius around the cross-section of the unit cell R and the twist angle of the unit cell β is defined in Figure 2.1b. If β is 0°, the Kresling origami unit cell becomes a straight-walled tube. All of the mandrels in this study are designed with the same $R = 36$ mm around the center-line of their walls. The height of the Kresling origami tubes can be calculated by $H_{kresling} = n_{cell}H_{unit}$, where n_{cell} is the number of unit cells. We set $n_{cell} = 4$ for all of the Kresling origami tubes. Three Kresling origami geometries are produced and their dimensions including the average thickness of the manufactured tubes are summarized in Table 2.1. The first Kresling origami geometry, notated as G1, has the shortest unit cell height. The second and third Kresling origami geometries, notated as G2 and G3 respectively, were chosen for a limited investigation into how the height and twist angle of the unit cell affects the mechanical response of the Kresling origami tube. The three Kresling origami tubes are also compared to filament wound circular and square tubes (Table 2.1). While their circumscribed radii were kept the same as the Kresling origami tubes, their heights were chosen so that their volumes were similar to the G1 tube.

2.2 Manufacturing

All of the Kresling origami tubes are constructed with filament winding techniques as shown in Figure 2.2. A Kresling origami-shaped mandrel and a carbon fiber tow [54] are allowed to rotate about their axes. Additionally, the carbon fiber tow can translate along its axis.

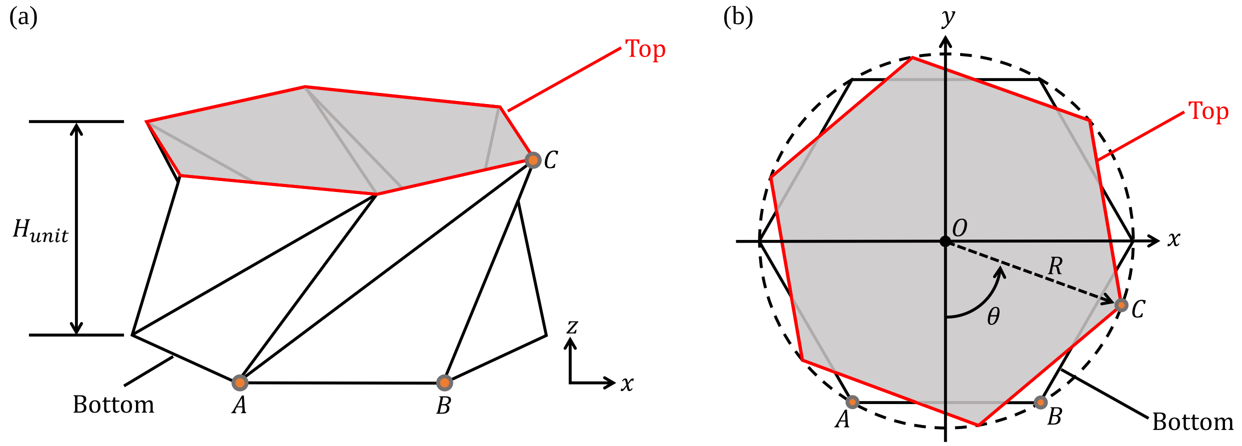

Figure 2.1: Geometrical parameters of the Kresling origami unit cell. (a) 3D view of a Kresling origami unit cell which defines the unit cell's height H_{unit}. (b) A top-down view of the Kresling origami unit cell that defines the unit cell's twist angle β and its circumscribed radius R.

Notice in Figure 2.2 that the axes of both the Kresling origami mandrel and the fiber tow are not parallel. This is to place the fibers easily on the mandrel and to help maintain tension on the fiber strand. Figure 2.2 also defines the mountain and valley folds for the mandrels. The fibers are oriented parallel with the valley creases to avoid fiber bridging across facets, since wrapping across the non-convex regions would require some form of pressure in addition to the tension of the fibers to conform to the Kresling geometry. Therefore, the proposed filament winding technique offers enhanced manufacturability and reduced costs in terms of time and complexity, though it may sacrifice structural performance (to be discussed further).

Table 2.1: Summary of test specimen properties

Specimen	H_{unit} (mm)	Height of Tube (mm)	$\beta(^\circ)$	Thickness (mm)	Standard Deviation in Thickness (mm)	Mass of Mandrel (g)	Total Mass (g)
G1	37.40	149.6	40	0.90	0.20	17.5	54.3
G2	52.55	210.2	40	0.99	0.16	22.6	70.6
G3	49.25	197.0	30	0.93	0.21	21.0	64.0
Circle	-	138.2	-	0.93	0.13	12.9	39.4
Square	-	146.3	-	1.03	0.24	14.5	44.8

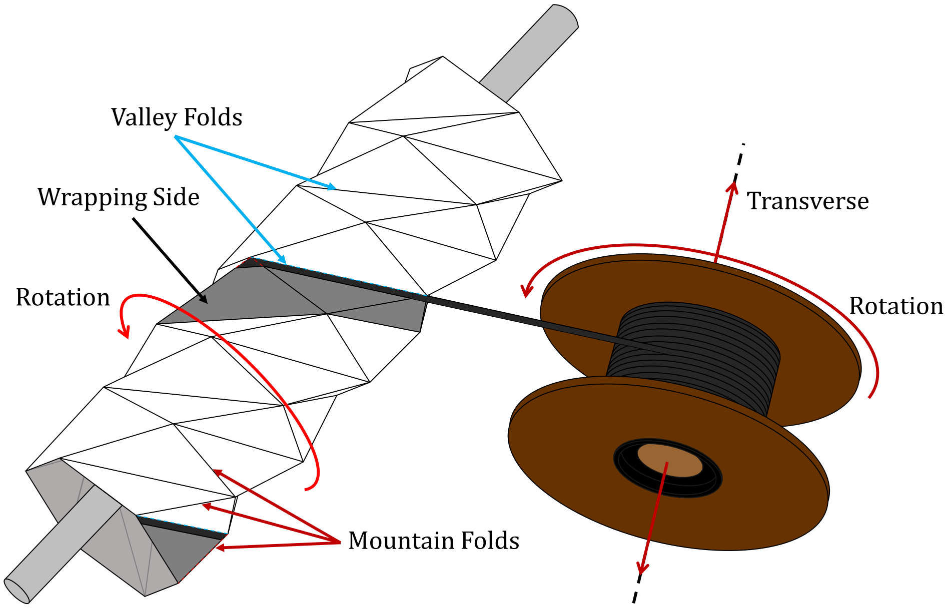

Figure 2.2: A schematic depicting the filament winding procedure for composite Kresling origami tubes. One side of the mandrel is wrapped at a time. The carbon fiber tow can translate and rotate about its axis.

Figure 2.3 describes the layup sequence of the composite Kresling origami tubes. The mandrel is constructed from 0.254 mm-thick polyethylene terephthalate (PET) [55] and coated with double-sided tape to prevent fiber slipping. As mentioned, the fibers of the Kresling origami tubes are oriented so that they are parallel with the valley creases of the Kresling origami tube.

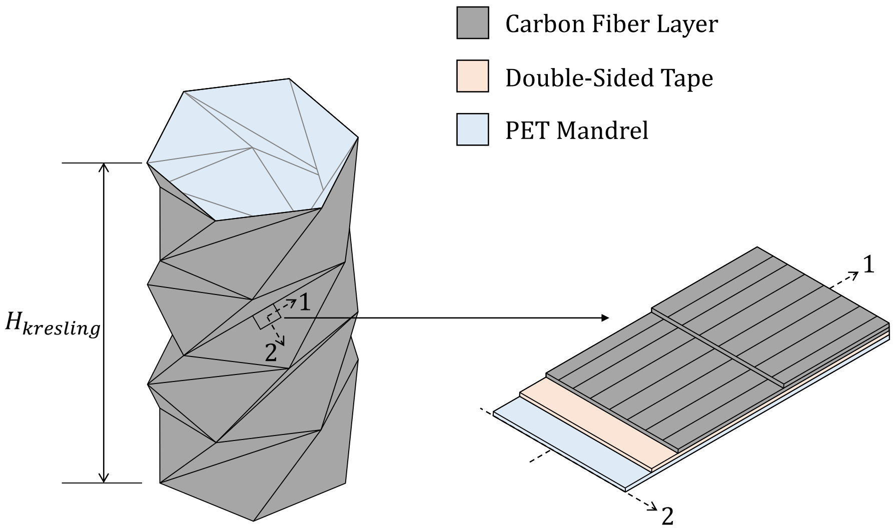

Figure 2.3: The layup sequence of the Kresling origami tubes.

Figure 2.4 shows the fold patterns utilized to construct the manufactured tubes in this study. The Kresling fold pattern requires two different types of engravings to be cut: valley and mountain fold engravings. Mountain folds generate outward creases while valley folds generate inward creases with respect to the tube. Both are engraved on only one side of the fold pattern. Circular cuts are then applied at each vertex of the fold pattern. Without these cuts, the facets near the vertices will not remain flat during folding. Each row of triangles in this pattern represent a unit cell while each column represents a side of the Kresling origami cross-section. The fold pattern for the circular tube does not need an engraving for folds. Instead, shallow engravings that do not allow for folding are applied around the mandrel to mark the location of the bonding region and to show the orientation of the first fiber layer. Similarly, the square tube fold pattern has the shallow engravings but must also have four additional mountain fold engravings to generate the square tube's four corners.

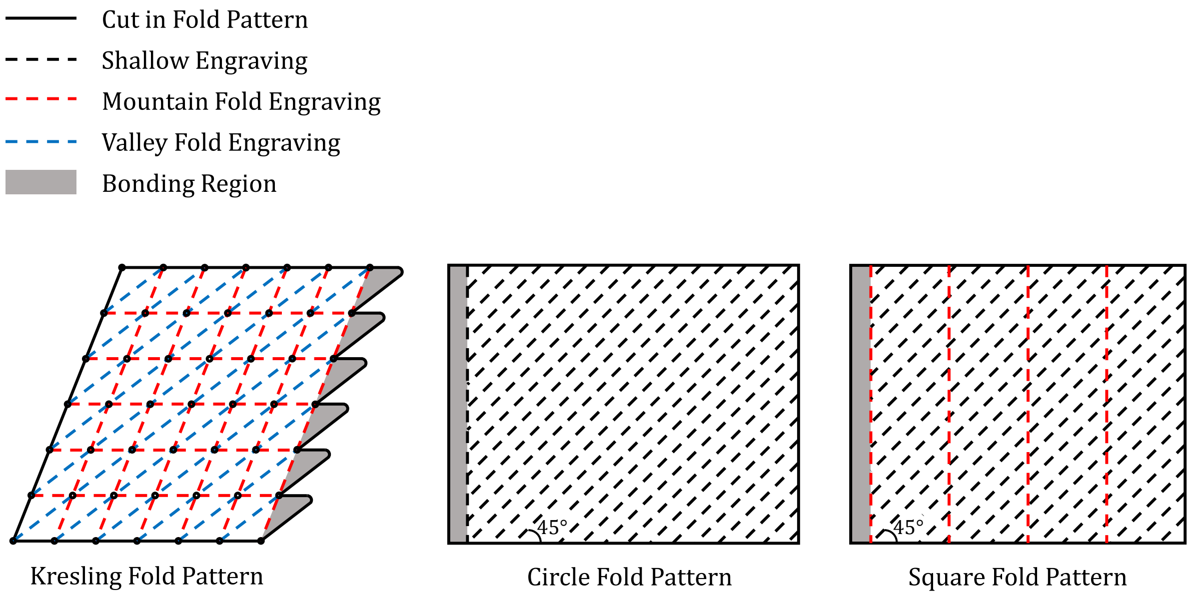

Kresling Fold Pattern

Circle Fold Pattern

Square Fold Pattern

Figure 2.4: The fold patterns for each mandrel geometry. All geometries require a bonding region for the mandrel to be closed and cuts for the shape of the pattern. Valley folds fold into the page and mountain folds fold out of the page. Both the circle and square tubes have shallow engravings on their surfaces set at 45° for the first layer of fibers to be properly oriented.

A Universal VLS-4.6 laser cutter is used to cut and engrave all three fold patterns. Figure 2.5a shows a Kresling origami fold pattern being cut from a PET sheet. After folding the pattern, Scotch® Permanent double-sided tape is applied at the bonding regions. The bonding regions are then made to overlap with the facets on the other side of the fold pattern as shown in Figure 2.5b, which finally closes the mandrel. A limitation from this step is the possibility of introducing misalignments in the facets of the fold pattern which affect the crushing behavior of the tube.

A difference between the preparation of the conventional tubes and the Kresling origami

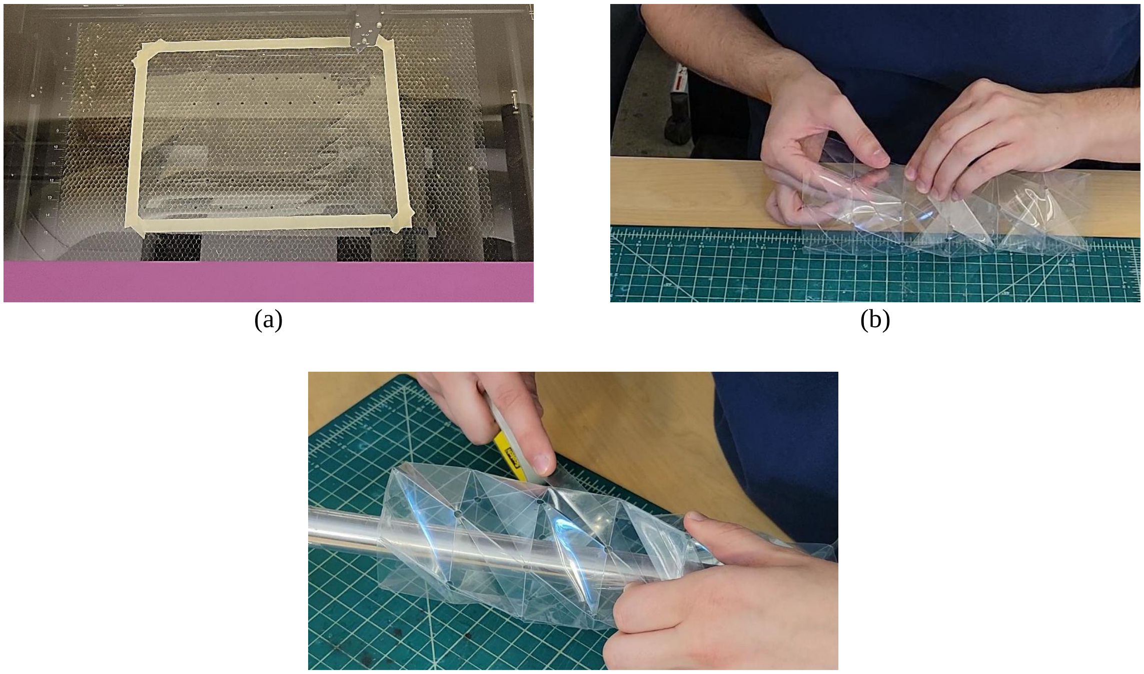

(a) (b) (c)

Figure 2.5: The steps to construct and prepare the mandrel for wrapping. (a) The desired fold pattern is engraved/cut from the PET roll using a Universal VLS-4.6 laser cutter. (b) The mandrel is folded along the desired engraved mountain and valley creases and closed using double-sided tape in its bonding regions. (c) The mandrel is covered with a layer of double-sided tape.

tubes comes from an additional step after the conventional tubes are closed: to maintain their shapes during wrapping, the conventional tubes have acrylic plates with their respective cross-sectional shape placed inside of them. The Kresling origami tubes do not need acrylic plates to maintain their cross-sectional shape due to the transverse stiffness introduced by their folds. In this step, it is possible that due to the soft PET material, the square tube will have rounded corners. For the circular tube, the cross-section will have a lip that spans the length of the tube due to the overlapping region of the PET sheet.

The mandrels must then be coated with the double-sided tape (Scotch® Permanent) to prevent fiber slippage during layup. For the Kresling origami tubes, the tape is wrapped parallel to the valley creases just as the fibers would be as shown in Figure 2.5c. For the conventional tubes, the tape is wrapped transversely around the mandrel. To prevent resin leakage in future steps, masking tape is placed on the inside of the Kresling origami mandrels to cover up the holes at the vertices (Figure 2.6a).

Figure 2.6 shows the rest of the manufacturing process. The first carbon fiber layer is wrapped around the mandrel as shown in Figure 2.6a. The tow utilized is a 24K carbon fiber tow from Fibre Glast® [54]. Masking tape is used to hold down one end of a fiber strand before it is finished being wrapped around the mandrel. After the strand has reached the other end of the mandrel, it is cut with scissors and held down with another piece of masking tape. This process is repeated until the mandrel is fully covered with a layer of fiber tows. The next step is to coat the dry fiber with resin (Figure 2.6b). The resin for the composite tubes used in this study is Fibre Glast® System 2000 Laminating Epoxy Resin cured with the 2120 Hardener which provides the resin a two-hour-long pot life [56]. The resin is applied with a China bristle brush. Then, the next carbon fiber layer is wrapped around the tube and coated with resin the same way as the previous fiber layer (Figures 2.6c-d).

After the two layers of layup, the tube is cured for 6 hours at 130°F in a convection oven (Figure 2.6e). We rotate the tube about 60° every five minutes for an hour to prevent the resin from forming hardened droplets along the tube. After that, the resin has sufficiently gelled, and the tube is rotated every thirty minutes until six rotations have been achieved. The tube is then stationary for the remaining time. After curing is completed, the tube is allowed to cool for twelve hours. A wet tile saw is used to remove the extra unit cells at the ends of the Kresling origami tube, thus leaving four cells only (Figure 2.6f).

For the circular and square tubes manufactured in this study, the first fiber layer is applied similarly to the Kresling origami tubes except that the first fiber layer is wrapped along the 45° lines engraved into the mandrel. The fibers are still held down with masking tape at both ends. The second layer is wrapped in the -45° direction to prevent twisting throughout the length of the tube under axial compression. Figure 2.7 shows the layup sequence of the

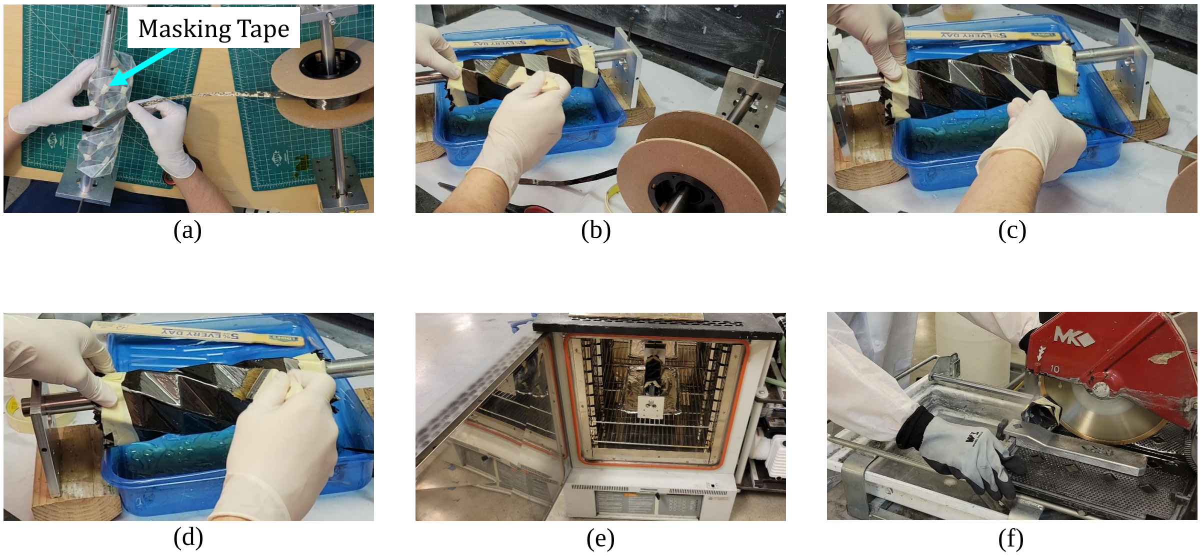

Figure 2.6: The layup steps and the final treatment of the Kresling origami tubes. (a) The first fiber layer is wrapped around the mandrel. (b) The first fiber layer is coated with epoxy resin. (c) The second fiber layer is wrapped parallel to the valley folds. (d) The second fiber layer is coated with the resin. (e) The mandrel is placed inside of a convective oven. (f) The two unit cells at the ends of the chain are removed using a wet tile saw.

conventional tubes in this study. Table 2.1 summarizes the masses of each mandrel as well as the total mass of each tube.

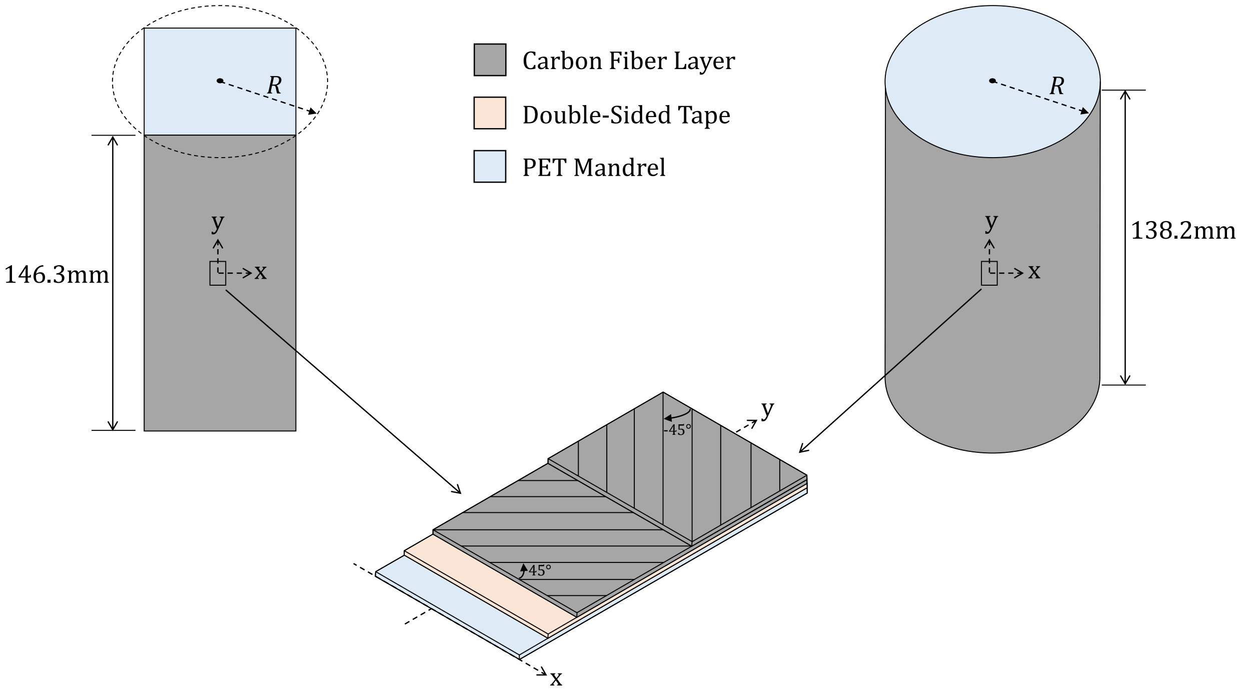

Figure 2.7: The layup sequence of the square tube (left) and circular tube (right).

The densities of the carbon fibers and epoxy resin are given in Table 2.2. Table 2.2 also summarizes both the provided and assumed elastic and mass properties for the fibers, resin, and PET. The fiber volume fraction in Table 2.3 is calculated using the masses and the densities of the carbon fibers and epoxy resin.

Table 2.2: Elastic and mass properties of the thin-walled tubes' constituent materials

Material	Young's Modulus, E (GPa)	Poisson's Ratio, ν	Density, ρ (kg/m^3)
Carbon Fiber	250 [a]	0.2	1800*
Epoxy Resin	17.3*	0.33	1301*
PET	2.25	0.33	1400

[a] Provided by manufacturer

Table 2.3: Summary of test specimen mass measurements

Specimen	Mass of Mandrel (g)	Mass of Fibers (g)	Mass of Resin (g)	Total Mass (g)	Fiber Volume Fraction, f
G1	17.5	14.0	22.8	54.3	0.307
G2	22.6	18.3	29.7	70.6	0.308
G3	21.0	18.7	24.3	64.0	0.357
Circle	12.9	14.4	12.1	39.4	0.462
Square	14.5	10.4	19.9	44.8	0.274

2.3 Methods of Investigation

In this investigation, we employ a finite element model to determine if the experimental crushing force responses of each tube can be reproduced numerically. The manufactured tubes are shown in Figure 2.8a and the experimental apparatus to test each one is detailed in Figure 2.8b. The experimental data is used to assist in fitting key parameters of the finite element model.

(a) (b)

Figure 2.8: (a) All of the thin-walled tubes tested for this study. From left to right - Kresling origami tube with geometry G1, Kresling origami tube with geometry G2, Kresling origami tube with geometry G3, the tube with a circular cross-section, and the tube with a square cross-section. (b) The experimental apparatus for quasi-static compression.

2.3.1 Experimental Approach

The quasi-static axial crushing tests were performed with an Instron 5585H electro-mechanical load frame with a 50 kN load cell with closed-loop control. The testing is displacement-controlled and is ended after densification becomes evident in the force-displacement curve. All tubes are compressed at a rate of 100 mm/min, and the bottom support platen for the tubes is allowed to rotate during compression. Experimental data was used to develop a finite element model.

2.3.2 Numerical Approach

In this investigation, we employ a finite element model to determine if the experimental crushing force responses of each tube can be reproduced numerically. The manufactured tubes are shown in Figure 2.8a and the experimental apparatus to test each one is detailed in Figure 2.8b. The experimental data is used to assist in fitting key parameters of the finite element model. The composite and PET layers of the tubes are modeled numerically but any tape present in the manufactured tubes are absent in the numerical model due to having relatively small stiffness compared to the other materials. Another simplification is made throughout the model: we do not round the creases and vertices in the Kresling origami tubes despite rounded creases and vertices being present in the composite layer of the manufactured tubes. It is not simple to resolve the conflicting curvature between mountain and valley creases at the vertices of the Kresling origami tubes. To maintain consistency between models, we also avoided rounding the corners of the square tube.

The numerical analysis was performed using the commercial FE solver Abaqus / Explicit (SIMULIA Corp., USA). The setup of the numerical simulations is shown in Figure 2.9. Each tube is modeled with separate composite and PET shell parts. The PET shell part has the designed circumscribed radius R of 36mm. The composite shell parts are assigned composite sections with two plies that have an identical thickness. The composite shell is given a radius R_{comp} that accounts for the thickness of the composite plies and PET layer so that there is no overlap or additional space between both parts of the models. The thicknesses of the composite plies are adjusted in each tube until the composite plies have approximately the same mass as in the manufactured tubes. The thicknesses of the plies in each tube are summarized in Table 2.4. Both the PET and composite parts are meshed with four-node reduced integration shell elements (S4R) as they are computationally efficient and relatively stable in modelling post-buckling behavior in nonlinear contact conditions [25]. A mesh convergence study was performed in order to determine a mesh density that provided a tradeoff between accuracy and feasible computational time. Based on the study, a global mesh size of 3mm was deemed acceptable for the Kresling origami tubes while a global mesh size of 2.5mm was chosen for the circular and square tubes. Abaqus' default criteria for element deletion is utilized for both the PET and composite layers. As an element is damaged, its stiffness components are degraded according to its respective damage evolution model. An element is deleted when all section points through its thickness at any one integration location have all stiffness components reduced to zero.

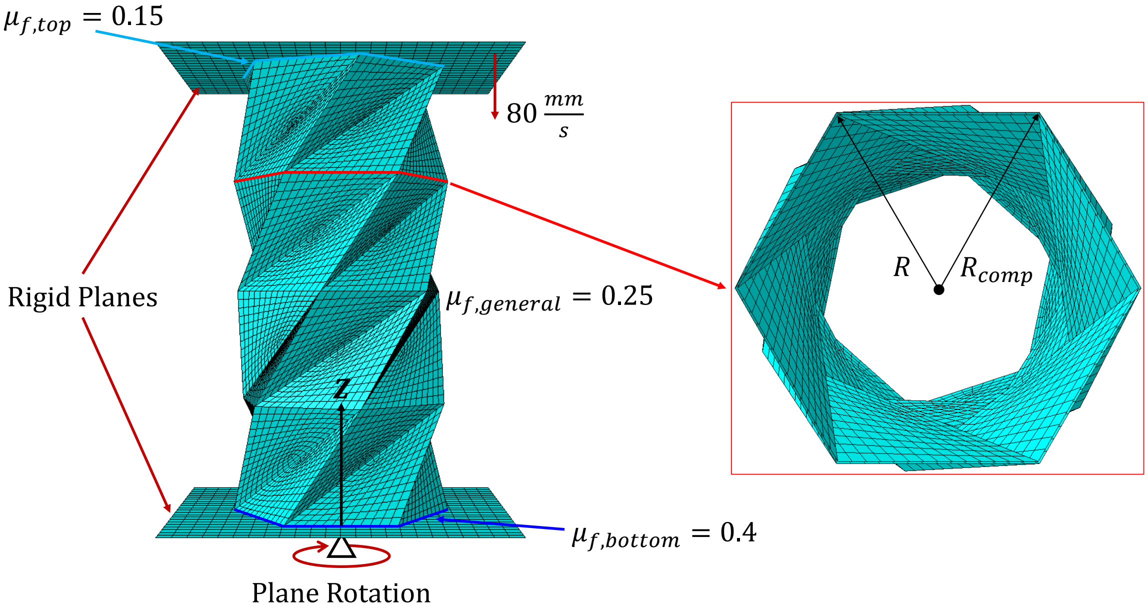

Figure 2.9: The setup of the finite element model.

Table 2.4: Thickness and mass properties for numerical simulations

Specimen	Ply Thickness (mm)	PET Thickness (mm)	Density of Composite, ρ_c (kg/m^3)
G1	0.34	0.2	1450
G2	0.34	0.2	1450
G3	0.33	0.2	1480
Circle	0.27	0.254	1530
Square	0.34	0.254	1440

The tubes are compressed between two rigid planes meshed with 4-node 3-D bilinear discrete rigid elements (R3D4) of global size 4.6mm. The bottom plane is restricted in translation along the Z-axis depicted in Figure 2.9. However, to meet the boundary conditions of the experimental setup, the bottom plane is allowed to rotate along this axis. As a way to account for the friction between the bottom platen and the rest of the experimental apparatus, the moment of inertia about the Z-axis is artificially increased. This allows us to avoid introducing more complex geometries and other friction parameters into the model. The moment of inertia is given in Table 2.5. The top plane applies the quasi-static axial compression to the tubes and its rotational motion is constrained. A mass scale factor of 100 was applied to the tubes to provide a balance between computational time and accuracy. A load rate study was conducted and it was found that 80 mm/s was an appropriate compression rate for the model as this prevented the kinetic energy of the model from increasing pass 5-10% of the internal energy of the model. Therefore, the model can remain quasi-static [57]. Three friction parameters are present in the model. The contact between the tube walls and the planes as well as self-contact between the tube walls is treated with a general contact algorithm with a coefficient of friction $\mu_{f,general}$ of 0.25. In the experimental apparatus, the top platen has a different surface finish than the bottom platen. Therefore, the friction between the top edge of the tubes and the top platen is different than the friction between the bottom edge of the tubes and the bottom platen. To capture this numerically, the coefficients of friction between the top cross-section of the tube and the top plane ($\mu_{f,top}$) and the bottom cross-section of the tube and the bottom plane ($\mu_{f,bottom}$) were modified until the numerical deformations achieved acceptable agreement with experimental deformations. Therefore, $\mu_{f,top}$ was set to 0.15 and $\mu_{f,bottom}$ was set to 0.4.

Table 2.5: Numerical properties of the FEM setup

Description	Variable	Value
General Contact Friction Coefficient	$\mu_{f,general}$	0.25
Friction Coefficient between Top Plane and Top of Composite Tubes	$\mu_{f,top}$	0.15
Friction Coefficient between Bottom Plane and Bottom of Composite Tubes	$\mu_{f,bottom}$	0.4
Mass of Bottom Plane (kg)	m_{bottom}	2.53
Moment of Inertia of Bottom Plane about Z-axis (10^{-6} g mm^2)	I_Z	25

The composite mechanical properties of each tube vary due to having different fiber volume fractions. Table 2.4 summarizes the mass and thickness properties in each tube while Table 2.6 summarizes the elastic properties utilized in each tube. Before calculation of these properties, we reduced the elastic moduli of the fibers and epoxy resin from Table 2.2. Since we cannot capture the initial stiffness of the tubes completely without introducing geometric defects, we saw this approach as a valid indirect way to capture the initial peak of the Kresling origami tubes. To determine how much to reduce them by, we scaled the moduli down on the Kresling origami simulations until the initial regions of all three Kresling origami tubes matched up as much as possible with the experimental results. It was determined that reducing the moduli by 20% worked the best across all three tubes. To maintain consistency, the approach was also used for the circular and square tubes. The reduced moduli are notated as $E_{f,red}$ and $E_{m,red}$ respectively. The Poisson's ratio of the fibers and epoxy resin are notated as ν_f and ν_m respectively and the respective density of both materials are notated as ρ_f and ρ_m. E_1, ν_{12}, and ρ_c are calculated using a rule of mixtures approach as follows:

$$E_1 = fE_{f,red} + (1-f)E_{m,red}, \tag{2.1}$$

$$\nu_{12} = f\nu_f + (1-f)\nu_m, \tag{2.2}$$

$$\rho_c = f\rho_f + (1-f)\rho_m, \tag{2.3}$$

Since we do not have measurements for void content, we neglect it as part of our calculations.

The rule of mixtures does not approximate other elastic properties well. As a consequence, we use the Halpin-Tsai equations to calculate E_2, G_{12}, G_{13} and G_{23} as these equations provide a better approximation [58]. We assume a reinforcement factor ξ_{E_2} of 2 for E_2 and a reinforcement factor $\xi_{G_{12}}$ of 1 for G_{12} as these are reasonable estimates when mechanical properties for the laminate are unknown [59]. As with the Young's modulus of the fibers and

Table 2.6: Elastic properties for numerical simulations

Specimen	Tensile Moduli		Shear Moduli		Poisson's Ratios	
	E_1 (GPa)	$E_2 = E_3$ (GPa)	$G_{12} = G_{13}$ (GPa)	G_{23} (GPa)	$\nu_{12} = \nu_{13}$	ν_{23}
G1	71.1	27.8	9.08	10.0	0.290	0.388
G2	71.2	27.8	9.09	10.0	0.290	0.388
G3	80.4	31.0	10.0	11.3	0.284	0.368
Circle	100	39.1	12.4	14.8	0.270	0.324
Square	64.9	25.8	8.52	9.22	0.294	0.401

matrix, we reduce the shear modulus of both materials by 20%. The modified shear moduli for the fibers and matrix are notated as $G_{f,red}$ and $G_{m,red}$ respectively. The equations for E_2 and G_{12} are:

$$E_2 = E_{m,red}\left(\frac{1 + \xi_{E_2}\eta_2 f}{1 - \eta_2 f}\right), \tag{2.4}$$

$$\eta_2 = \frac{E_{f,red}/E_{m,red} - 1}{E_{f,red}/E_{m,red} + \xi_{E_2}}, \tag{2.5}$$

$$G_{12} = G_{m,red}\left(\frac{1 + \xi_{G_{12}}\eta_{12} f}{1 - \eta_{12} f}\right), \tag{2.6}$$

$$\eta_{12} = \frac{G_{f,red}/G_{m,red} - 1}{G_{f,red}/G_{m,red} + \xi_{G_{12}}}, \tag{2.7}$$

K_f and K_m are the bulk moduli of the fibers and matrix respectively and are calculated using the reduced elastic moduli of both materials.

G_{23} requires more steps to calculate. A semi-empirical version of Halpin-Tsai is adopted. First, we need the bulk modulus of the composite, K:

$$K = \frac{1}{f/K_f + (1 - f)/K_m}, \tag{2.8}$$

Then, we need to calculate ν_{21} to find ν_{23}:

$$\nu_{21} = \frac{E_2}{E_1}\nu_{12}, \tag{2.9}$$

$$\nu_{23} = 1 - \nu_{21} - E_2/(3K), \tag{2.10}$$

G_{23} is finally calculated as:

$$G_{23} = \frac{E_2}{2(1+\nu_{23})}, \tag{2.11}$$

Since we are using uniaxial plies, $E_2 = E_3$, $\nu_{12} = \nu_{13}$, and $G_{12} = G_{13}$.

Abaqus' built-in Hashin failure criteria was adopted to model the failure of the composite walls. We referred to the composite failure stresses from Han [60] and scaled the stresses until numerical results more closely matched the experimental data.This required running numerous simulations while decreasing all of the stresses by the same factor. Ultimately, reducing the stresses by 20% was determined to be satisfactory for our study. Similarly, Abaqus' built-in linear softening energy damage evolution scheme was utilized for post-damage initiation. To avoid spurious mesh dependency in the presence of strain localization, the crack band model [61], successfully used in a variety of simulations on composites [62, 63, 64, 65], was adopted in this work. The fracture energies for this scheme were taken from Zheng [66] and scaled similarly to the failure stresses. For the fracture energies, reducing each by about 75% from the ones reported in [66] was satisfactory for this study. The failure stresses of the composites and the fracture energies are summarized in Table 2.7. Note: G^c_{1t} is reported as an average value as it is slightly different between all five tubes.

We refer to the paper by Gupta [67] for the stress-strain data, elastic material properties, and fracture energy of PET for use in our numerical model. This information is not wholly reflective of the PET in the manufactured specimens but it is complete with more information than what is provided by the manufacturer. The yield strength, fracture strain, and fracture toughness of the PET from Gupta [67] are summarized in Table 2.8. The built-in ductile

Table 2.7: Composite Failure Properties

Description	Variable	Value
Longitudinal Tensile Strength (MPa)	X_{1t}	1280
Longitudinal Compressive Strength (MPa)	X_{1c}	800
Transverse Tensile Strength (MPa)	X_{2t}	48.8
Transverse Compressive Strength (MPa)	X_{2c}	104
In-Plane Shear Strength (MPa)	S	73.6
Longitudinal Tensile Fracture Energy (N/mm)	G_{1t}^c	32.8
Longitudinal Compressive Fracture Energy (N/mm)	G_{1c}^c	36
Transverse Tensile Fracture Energy (N/mm)	G_{2t}^c	22.5
Transverse Compressive Fracture Energy (N/mm)	G_{2c}^c	35

damage criteria was utilized along with a linear energy-based damage evolution scheme to model the damage in the PET layer. Additionally, the density of the PET is increased by 7.1% so that the mass of the PET layer also accounts for the mass of the tape used to construct the mandrel.

Table 2.8: PET Failure Properties

Description	Variable	Value
PET Yield Strength (MPa)	σ_y	28.85
PET Plastic Fracture Strain (mm/mm)	$\varepsilon_{fracture}$	0.0872
PET Fracture Energy (MPa)	G_f	3.18

Some simplifications are applied to the PET layer. The first simplification is related to the PET thickness. The manufactured Kresling origami tubes relied on laser cutting the creases and removing the vertices. Therefore, the amount of material bending at the creases is less than the original thickness of the PET. Rather than creating cells along the creases in the numerical model which introduces more dimensional and meshing parameters, the thickness of the entire PET layer in the Kresling origami tubes is reduced to 0.2mm from the original 0.254mm. This thickness was chosen after a study was conducted to see how decreasing the thickness affected the initial peak of the response for the Kresling origami tubes. Although the square tube also has creases at its corners, we do not reduce the thickness of the PET as these creases are not used to facilitate folding. Another simplification concerning thickness includes the overlapping PET regions where the thickness of the PET is doubled. To determine if the overlaps were necessary, we ran tests on the conventional tubes and the G1 tube to see if doubling the PET in the appropriate regions significantly affected the results. Ultimately, we decided to neglect these regions as there was an insignificant change in the force-displacement and deformation results. The final simplification with the PET layer concerns any pre-existing damage in the creases from its folding. As we do not have a way to predict this damage, it is not included in the numerical model.

To model the bond between the PET and composite regions of the tubes, we utilize a cohesive contact formulation with elastic and failure properties summarized in Table 2.9. Abaqus' built-in quadratic traction failure initiation scheme is used to model the initial failure of the cohesive contact and a linear energy-based Benzeggagh-Kenane fracture criterion is used to model the resulting damage evolution. We refer to Han [60] for these cohesive properties. However, the authors of this paper use a value of 10^6 N/mm^3 to model the cohesive elastic stiffness of their cohesive layers. For the stiffness of our cohesive contact, we reduce this value by a factor of 100. We compared the responses of the circular tube and G1 with both values of cohesive elastic stiffness and found that reducing the stiffness does not significantly affect the results. We treat this as a suitable compromise between computational expense and results accuracy.

2.3.3 Axial Crush Indicators

In both experimental and numerical investigations, we keep track of key parameters that indicate the crushing performance of the thin-walled tubes. Energy absorption is a parameter that measures a structure's ability to dissipate crushing energy and can be calculated from

Table 2.9: Cohesive Properties

Description	Variable	Value
Elastic Properties (N/mm^3)	$K^0_{nn} = K^0_{ss} = K^0_{tt}$	10^4
Normal Damage Initiation (MPa)	t^0_n	40
Shear Damage Initiation (MPa)	$t^0_s = t^0_t$	50
Normal Fracture Energy (N/mm)	G_{Ic}	0.25
Shear Fracture Energies (N/mm)	$G_{IIc} = G_{IIIc}$	0.75
BK Exponent	η	1.45

integrating the force-displacement curve from axial loading tests: $EA = \int_0^\delta F(s)\,\mathrm{d}s$ [18]. In this equation, δ is the displacement experienced by the plate at the top of the tube, F is the crushing force, and s represents the displacement path. The calculation of the total EA from full compression can be seen visually in Figure 2.10. We can compare the dissipative effects of different structural designs by calculating their respective specific energy absorption [18]: $SEA = \frac{EA}{m}$, where m is the mass of the composite tube. The SEA is affected by both the structure's geometry and material properties.

The mean force exerted by a structure through its entire compression is related to the energy absorption of the structure [18]: $F_{mean} = \frac{EA}{\delta_{max}}$, where δ_{max} is the maximum compressive displacement. Additionally, we consider the peak force of the structure during initial failure, $IPCF$. Often times, it is crucial to reduce $IPCF$ to minimize the initial impact applied to a target object (e.g., impact applied to a pedestrian by an automotive bumper) [68]. Visual definitions F_{mean} and $IPCF$ are also provided in Figure 2.10. We must also consider the relative size of F_{mean} compared to $IPCF$. If F_{mean} is significantly smaller than $IPCF$, this means there are significant load variations in the force-displacement response and that the compression after the initial peak may not efficiently absorb energy. If F_{mean} is relatively close in value with $IPCF$, we have less load variations and more of the compression is effectively dissipating the crushing energy. This also suggests a more stable collapse. We measure these load variations through a parameter known as the crushing force efficiency:

$CFE = \frac{F_{mean}}{IPCF}$ [18]. We strive to design structures that make the CFE as close to one as possible, such that a structure can absorb a significant amount of energy without sacrificing the efficiency of the compressive deformation.

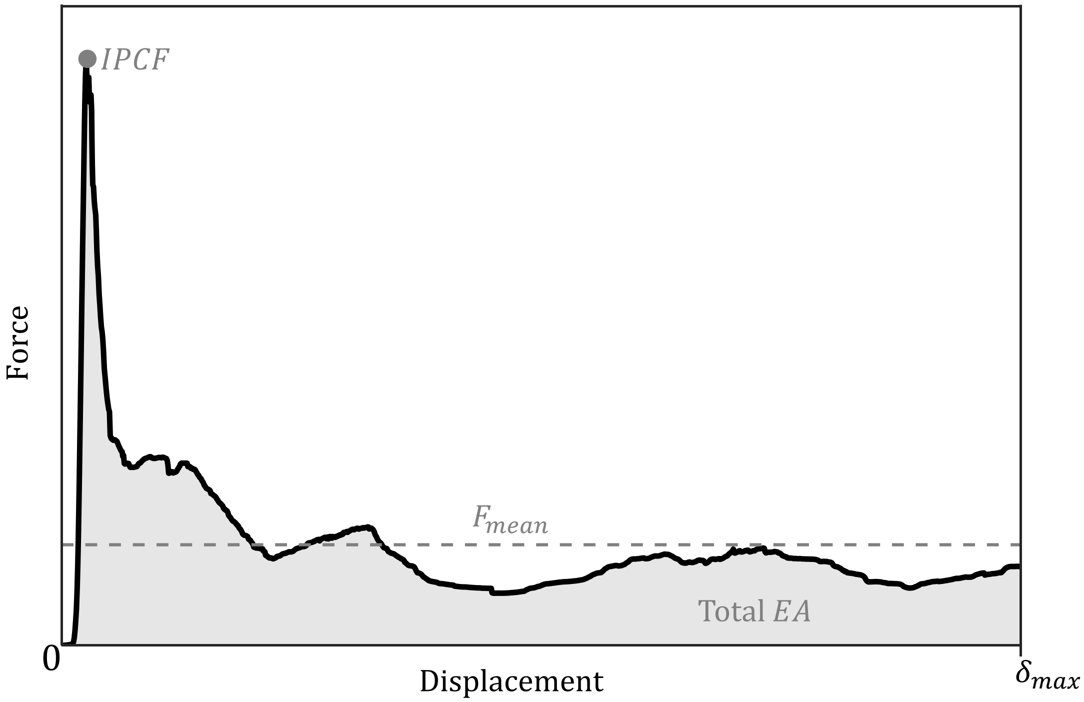

Figure 2.10: An example force-displacement curve of an axially loaded tube with axial indicators labelled.

2.4 *Results and Discussion*

2.4.1 Responses of Composite Tubes Under Compression

We proceed by investigating each tube's experimental and numerical responses one by one beginning with the conventional tubes. Figures 2.11-2.15 focus on each composite tube's quasi-static compression results individually. Each figure has three components: a) the significant deformation modes during the experimental crushing process, b) top- and side-views of the tube after it has been removed from the load frame and its final numerical deformations, and c) the experimental and numerical force-displacement curves superimposed together. Superimposed plots of the experimental and numerical responses and the stress contours for the final numerical deformations can be found in Appendix A.

The circular tube in Figure 2.11a (Images 1-2) initially fails with a near diamond-like buckling pattern through its walls. This corresponds to the initial peak seen in its experimental force-displacement curve and the drastic drop in force (Figure 2.11c). This deformation mode gives it the largest $IPCF$ observed of 6.30 kN. After this initial buckling, what we see in Figure 2.11a (Images 3-4) are walls that are inclined after the initial buckling and these walls are not able to offer significant resistance to the compression. This part of the deformation accounts for a large region of the force-displacement curve. Noticeable fracturing in the composite layers also begins to appear in Figure 2.11a (Image 4). Figure 2.11a (Image 5) shows the state of the cylinder at the end of the compression. In Figure 2.11b, we see how the composite layers fractured around the walls of the tube. The fracture is mainly concentrated along the creases generated by the local buckling of the tubes' walls. The fracture can be observed through both angled plies in these regions and can either be parallel to the fibers in the layer or nearly perpendicular to the fibers. Delamination between plies as well as delamination from the PET mandrel are present as well.

In numerical simulations, significant fracture only occurs at the top of the tube and in localized areas. Additionally, local wall buckling is not observed in the simulation during initial failure, possibly due to the absence of imperfections introduced from the manufacturing. This explains why the initial peak is over-estimated by the FE model. It has been widely documented in previous studies that cylindrical shells are imperfection sensitive and that their axial compressive failure loads can be reduced significantly by imperfections [69]. The discrepancy between the experimental and numerical initial peak loads affects the reliability and sensitivity of the axial indicators that we are investigating, but the general trends in each indicator are still maintained as we will discuss later. The initial peak discrepancy can be mitigated by fabricating the prototypes more precisely with filament winding machines.

This would have the effect of reducing any imperfections introduced by manufacturing and could increase the initial peak load. Additionally, we could reduce the initial peak force from numerical simulations by accounting for the manufacturing imperfections evident from the manufactured tubes. The rest of the numerical force-displacement curve shows relatively good agreement with the experimentally measured curve.

Similar to the circular tube, the square tube fails initially with local wall buckling near the top and bottom of the tube (Figure 2.12a (Images 1-2)). The square tube has a slightly smaller $IPCF$ of 5.51 kN compared to the circular tube (Figure 2.12c). The composite layers proceed to fracture at the top end of the square tube (Figure 2.12a (Image 3)). In Figure 2.12a (Image 4), the un-crushed part of the square tube recovers some stiffness and forms a second peak between ∼40-60 mm of compression. After this point, more local buckling and fracture at the bottom of the tube reduces its stiffness. The tube also begins to lean (Figure 2.12a (Image 5-6)) which is most likely a result of variations in composite wall thickness and minor misalignments in the edges at the ends of the tube. Figure 2.12b shows significant fracturing in the composite walls. The recovery of stiffness in multiple places in the force-displacement curve provides the square tube with a larger F_{mean} of 1.99 kN compared to the F_{mean} of the circular tube of 1.22 kN. Similar to the circular tube, the numerical results only show significant fracture at the top of the tube and in certain localized areas. As a result, the numerical model overestimates the initial peak just as it does the circular tube for the same reasons.

The crushing behavior of the Kresling origami is highly distinctive from that of the conventional tubes. Starting with the G1 Kresling origami tube, Figure 2.13a (Images 1-2) shows the initial failure in the Kresling origami structure with the only apparent signs of failure occurring when the top unit cell begins to twist. The G1 tube has a smaller peak force ($IPCF = 1.48$ kN) than the tested conventional tubes because of the presence of creases. The pattern of collapse in the G1 tube is also unlike the collapsing behavior seen in conventional tubes. The unit cells in G1 collapse in a cascading fashion throughout the compression. The top unit cell is the first unit cell to be completely crushed (Figure 2.13a (Image 3)). This

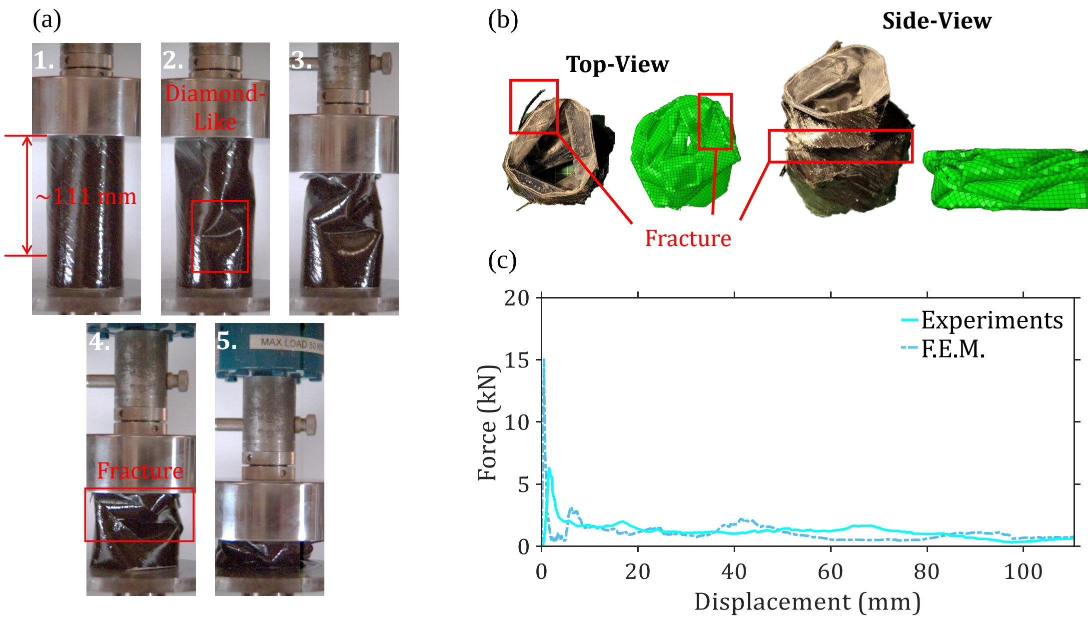

Figure 2.11: (a) The significant deformations of the tube with a circular cross-section under compression. Effective compression distance of the tube is labelled. (b) Top- and side- views of the tube after it is removed from the load frame and its final numerical deformation. (c) The experimental and numerical force-displacement plots of the tube

is followed by the full collapse of the second-from-the-top unit cell (Figure 2.13a (Image 4)) and then the bottom unit cell (Figure 2.13a (image 5)). The third-from-the-top unit cell is the final one to be crushed (Figure 2.13a (Image 6)). The pre-folded creases in the Kresling origami tube guide the structural cell-by-cell collapse under compression and will fold when the composite layer in the creases fail on a material level.

The cascading effect results in a smoother collapse compared with the conventional tubes. This is supported by observing the final geometry of the fractured tubes between Figures 2.11b, 2.12b, and 2.13b. In contrast to the conventional tubes that have fractures in many locations along the surface of the tubes, G1 Kresling tube has cracking and fractures mainly concentrated at the creases. This resulted in a partial recovery of the tubular shape of the

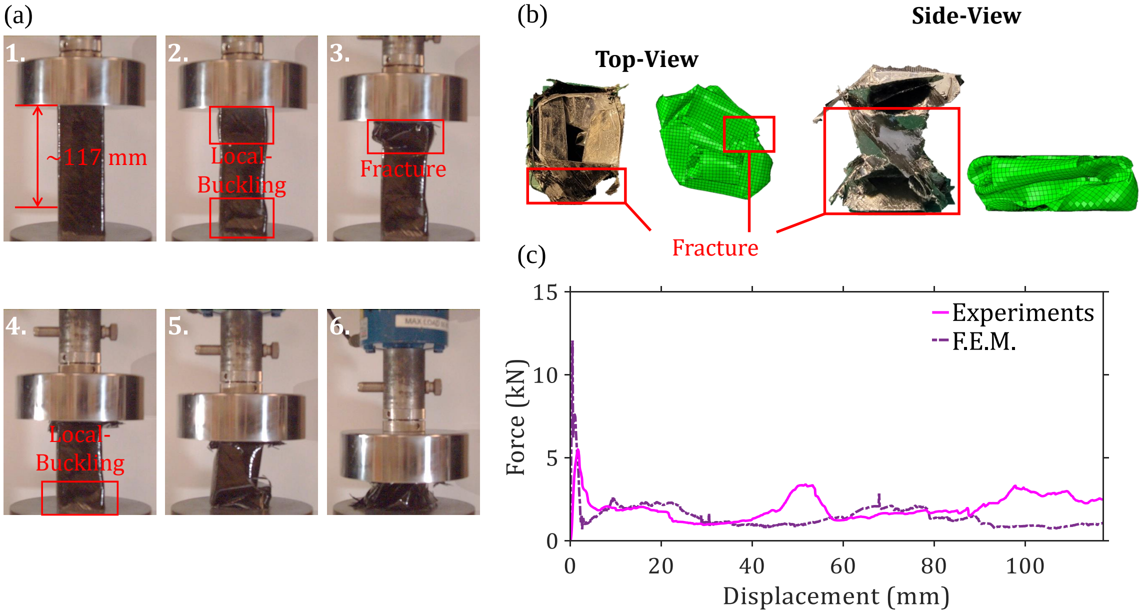

Figure 2.12: (a) The significant deformations of the tube with a square cross-section under compression. Effective compression distance of the tube is labelled. (b) Top- and side- views of the tube after it is removed from the load frame and its final numerical deformation. (c) The experimental and numerical force-displacement plots of the tube.

G1 prototype after being removed from the load frame (see the upright posture of the G1 prototype in Figure 2.13b compared to the severely crushed conventional tubes in Figures 2.11b and 2.12b). Additionally, the force-displacement curve of G1 also suggests a stable collapse provided by the cascading effect (Figure 2.13c). The first peak coincides with the initial material failure of the tube. After the initial failure, the top unit cell cannot provide as much resistance against the load resulting in a valley region. The second peak forms when the walls of the top unit cell begin to press down on the second unit cell which has not failed yet. The structure recovers stiffness comparable to its initial cell collapsing state. The top of the second peak occurs around complete collapse of the top unit cell and coincides with failure of the second unit cell. This process repeats until the collapse of the last unit cell. The numerical model captured this cascading collapse for G1 satisfactorily despite some deviations in the deformation modes.

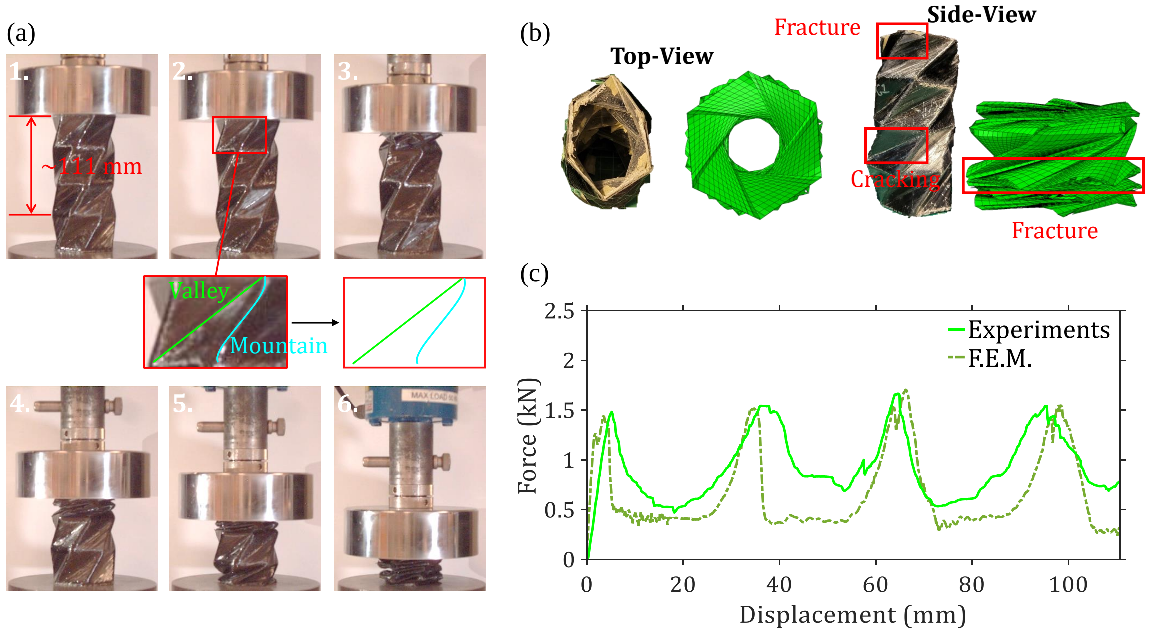

Figure 2.13: (a) The significant deformations of the G1 Kresling origami under compression. Effective compression distance of the tube is labelled. An inset shows the initial shapes of the top unit cell's mountain and valley creases. (b) Top- and side- views of the tube after it is removed from the load frame and its final numerical deformation. (c) The experimental and numerical force-displacement plots of the tube.

The collapsing behavior of G2 is similar to G1 in terms of the cell-by-cell cascading collapse (Figure 2.14a). There are, however, some noticeable differences as a result of increasing the height of the unit cells. Insets are provided in the second images of Figures 2.13a and 2.14a to illustrate the shape of the diagonal mountain and valley creases in the respective top unit cells after initial failure. The G1 tube appears to maintain mostly straight creases during failure with noticeable curvature near the vertices whereas G2 has curvature more through the middle of the diagonal mountain crease. The differences between the two suggest that G2 undergoes more significant facet bending. To explain why this happens, we define the twist rate of a Kresling unit cell as β/H_{unit}. It has been shown before that increasing this value either by decreasing the height or increasing the twist angle can facilitate more compliance in a Kresling unit cell [44]. In one extreme case that β (i.e., the twist rate) becomes zero, we have a straight-walled tube whereby all of the compressive load is resisted by the walls. For the cases where β is not zero, increasing the height while maintaining the twist angle and circumscribed radius also reduces the twist rate and increases the fold angles between facets. As a result, the structure increases in stiffness as more of the compressive load is resisted by the facets. In the case of G2, the height has been increased compared to G1 and the twist rate has been decreased by nearly 30%. As the height increases, more facet bending must occur to facilitate collapse and less deformation is concentrated along the creases. The idea that a lower twist rate increases the stiffness of the structure is also supported by the initial peak force of G2 ($IPCF = 1.87$ kN) being larger than G1's and still significantly smaller than the conventional tubes tested.

As a result of decreasing the twist rate, we witness more severe fracture along the diagonal and horizontal creases in G2 compared to G1 (Figure 2.14b). In Figure 2.13b, we see that G1 maintains some portion of its elasticity after being removed from the load frame. In contrast, half of G2's unit cells remain mostly collapsed. Both experimentally and numerically, more fractures are evident along the horizontal creases in G2 whereas G1's horizontal creases remain mostly intact. This behavior also explains the twin-peak behavior in the numerical force-displacement curve of G2 (Figure 2.14c). After the first valley region following the initial peak, the force begins to surge upwards as the first unit cell to collapse begins to transfer the force to the next unit cell through bending along the horizontal creases. Once the horizontal creases fracture, the force drops and picks up again, as the walls of the collapsed unit cell begin to densify and press down on the next unit cell. This process repeats unit cell to unit cell. Experimentally, when the horizontal creases fracture, the drop in stiffness is not as severe so we do not witness two peaks of similar size.

In Figure 2.15a, it is evident that G3 also follows a cascading cell-by-cell collapse but

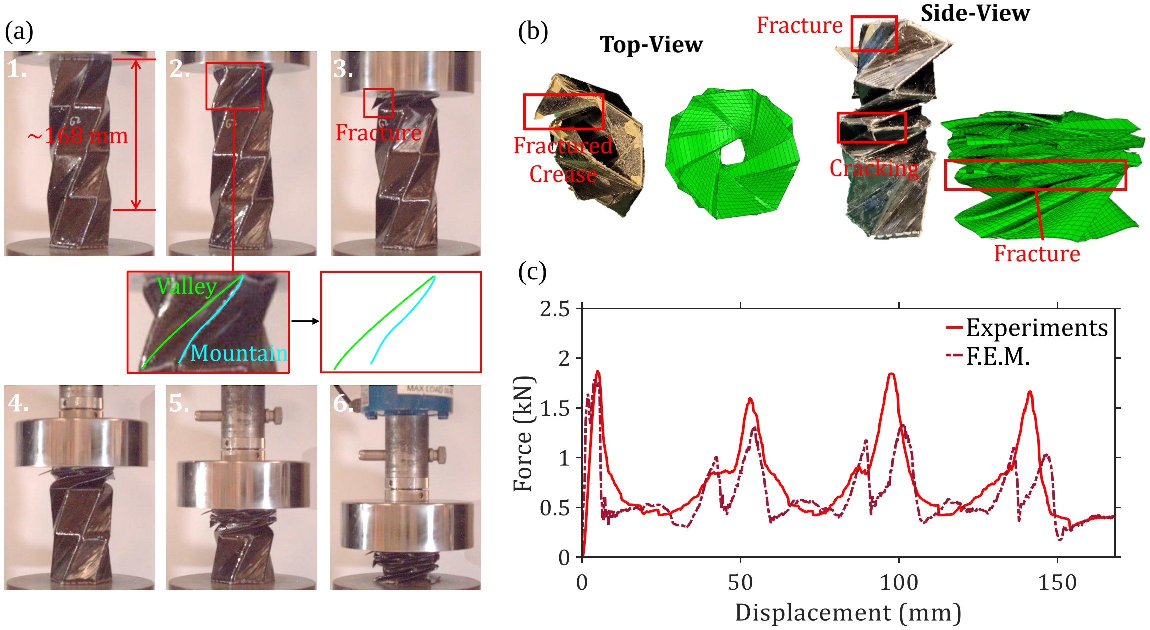

Figure 2.14: (a) The significant deformations of the G2 Kresling origami under compression. Effective compression distance of the tube is labelled. An inset shows the initial shapes of the top unit cell's mountain and valley creases. (b) Top- and side- views of the tube after it is removed from the load frame and its final numerical deformation. (c) The experimental and numerical force-displacement plots of the tube.

reducing the twist angle resulted in some qualitative differences between G3 and the other Kresling origami tubes. Reducing the twist angle decreased the twist rate of the tube about 20% compared to G2 and brought the facets more in line with the direction of loading. As a result, facet bending became more prominent in G3 than G2 which is supported by the inset for the second image of Figure 2.15a. In this inset, an additional fold line is generated in the facet, and the diagonal mountain crease curves noticeably during compression. The orientation of the facets facilitated increased resistance to the loading and promoted more structural stiffness compared to G1 and G2. This is seen in Figure 2.15c where the experimental initial peak force is 2.20 kN which is ~18% greater than that of G2. The decrease in the twist angle evidently facilitated more fracture in the creases of G3 compared with G2 (Figure 2.15b). As a result, none of the unit cells of G3 were able to expand as much as the unit cells in G1 or half the unit cells of G2. All of the unit cells of G3 remain mostly collapsed. The force-displacement curves of G3 are similar to G2's in that the fracture of the horizontal creases results in regions where the force begins to increase but then drops due to the loss of resistance (Figure 2.15c). Once again, these regions manifest slightly differently in numerical and experimental force-displacement curves. Common to both curves are larger valley regions compared to G2's force-displacement responses because the fracture is more significant in G3.

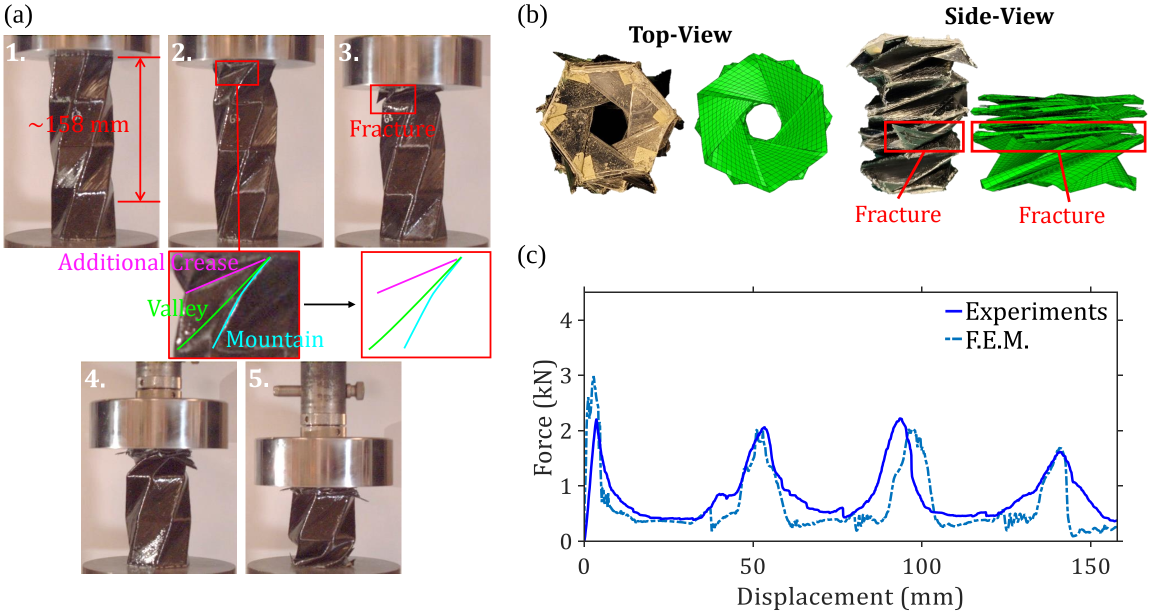

Figure 2.15: (a) The significant deformations of the G3 Kresling origami under compression. Effective compression distance of the tube is labelled. An inset shows the initial shapes of the top unit cell's mountain and valley creases. An additional crease is generated in the facets. (b) Top- and side- views of the tube after it is removed from the load frame and its final numerical deformation. (c) The experimental and numerical force-displacement plots of the tube.

2.4.2 Extracted Parameters

We now look at the energy absorption capabilities of the composite tubes. Figures 2.16a and 2.16b depict the experimental and numerical evolution of the SEA for all of the composite tubes through their compression, respectively. For this calculation, we have excluded the mass of the PET mandrels and have accounted only for the CFRP masses because the CFRP takes the majority of the loads compared to the mandrels. See the "Additional Results" section of the supplementary information for the specific energy absorption results with the total mass of the tube. The conventional tubes have very similar qualitative changes in their respective SEA's up to ∼80 mm of displacement in both plots. As a result of the square tube recovering some stiffness after this point experimentally, its SEA increases at a larger rate than the circular tube. From both approaches, the order of magnitude is similar between the conventional tubes as well as the qualitative end behavior.

The Kresling origami tubes maintain relatively close levels of SEA through most of their respective compression cycle up to the end of G1's compression. Due to not having deep valleys in its force-displacement curve, the G1 tube develops a larger mean force compared with the other two Kresling origami tubes and has the largest SEA up to its full compression. The G2 tube appears to have the smallest SEA evolution out of the three Kresling origami tubes due to its smaller peaks compared to G3. Both the circular and square tubes maintain larger SEA capabilities throughout their entire compression compared to all three Kresling origami geometries tested.

Figure 2.17a illustrates the difference between the final SEA of all the composite tubes from both the experimental and numerical responses. The square tube dissipates the most crushing energy followed by the circular tube. The circular tube dissipates about 2/3 of the energy of the square tube experimentally and about 80% numerically. The Kresling origami tubes only dissipate a little more than 1/3 of the square tube's energy. For the case of the Kresling origami geometries tested, we do not gain an advantage in terms of specific energy absorption. Based on G3's energy absorption compared to G2 both numerically and exper-

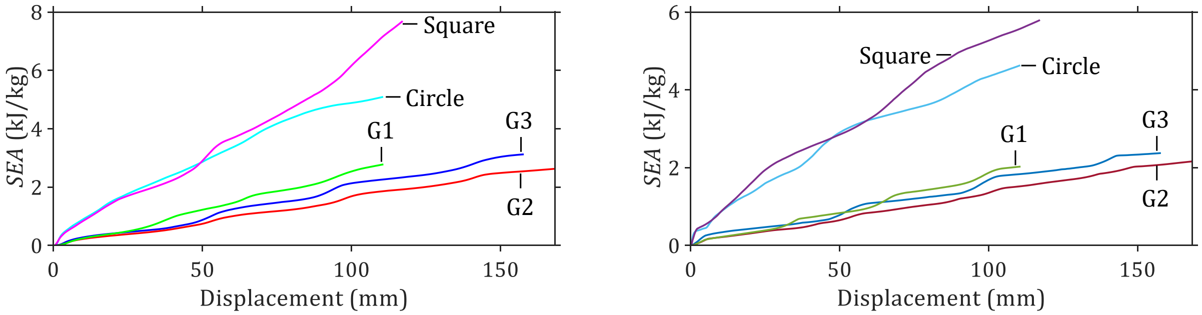

(a) (b)

Figure 2.16: The variation of the specific energy absorption for all thin-walled tubes without accounting for the mandrel mass for (a) experimental results and for (b) numerical results.

imentally, it may be more beneficial to reduce the twist angle of the Kresling origami tube since more of the load is resisted by the facets rather than the creases. Additionally, as the G1 and G2 tubes absorb very similar amounts of energy per mass, there may be diminishing returns on increasing the unit cell height because the tube mass increases. Moreover, it seems increasing the unit cell height is not as effective in increasing energy absorption as reducing the twist in the unit cell.

In Figure 2.17b, we compare the $IPCF$ values of all of the tubes both experimentally and numerically. Immediately observable is how the conventional tubes both have significantly higher peaks compared with the Kresling origami tubes. Experimentally, the square tube only decreases the $IPCF$ of the cylinder by 12.5% but the G1 tube decreases it by 76.5%, the G2 tube by 70.3%, and the G3 tube by 65.0%. The numerical results support this trend but the differences between the Kresling origami and conventional tubes $IPCF$ is more drastic due to the overestimation of the conventional tubes' $IPCF$. Overall, the Kresling origami tubes are efficient in reducing the initial peak force during the crushing process due to their corrugated geometries. We also see that to reduce the initial peak of the response, the twist in the unit cell must be increased. Decreasing the height has the same effect.

The Kresling origami composite tubes do not have an advantage in terms of F_{mean} (Figure 2.17c). In both experimental and numerical cases, the square tube has the largest F_{mean} followed by the circular tube. The circular tube reduces the mean force by 38.7% experimentally and 25.9% numerically. The Kresling origami tubes only maintain a little less than half of the mean force of the square tube. If we only look at the Kresling origami tubes, G1 has the largest mean force. Interestingly, the increase in unit cell height resulted in larger peak forces for G2 and G3 but due to shallower valley regions, the change in geometry translated into a smaller F_{mean} compared to the G1 tube. Having larger peaks than G2 did provide G3 with an advantage in terms of F_{mean}.

In Figure 2.17d, we compare the CFE between all of the composite tubes. G1 has the most efficient crushing force response both experimentally and numerically. G2 and G3 are the next most efficient tubes. Experimentally, they have a reduction from G1's CFE of 35.7% and 38.1% respectively, whereas numerically the reductions are 24.3% and 52.2% respectively. Therefore, not only is G1 more efficient than the conventional tubes, it is the most efficient Kresling geometry among the three prototypes tested. When facet bending becomes more significant, as in the case of G2 and G3, the efficiency decreases because of increased initial stiffness of the structure followed by more damage in the unit cells after they fail. Moreover, reducing the twist in the unit cell also results in more damage at similar heights explaining the reduction of efficiency between G2 and G3.

Although the conventional tubes hold an advantage in terms of energy absorption, the Kresling tubes have a superior crushing force efficiency, meaning a more uniform response. Energy absorption of the Kresling tubes could be improved by re-orienting the fibers so that the valley creases offer increased resistance. However, this would add steps to the manufacturing process that may sacrifice manufacturability for future automation. It may be possible for improvements to be achieved through tuning the Kresling geometry without changing the manufacturing approach.

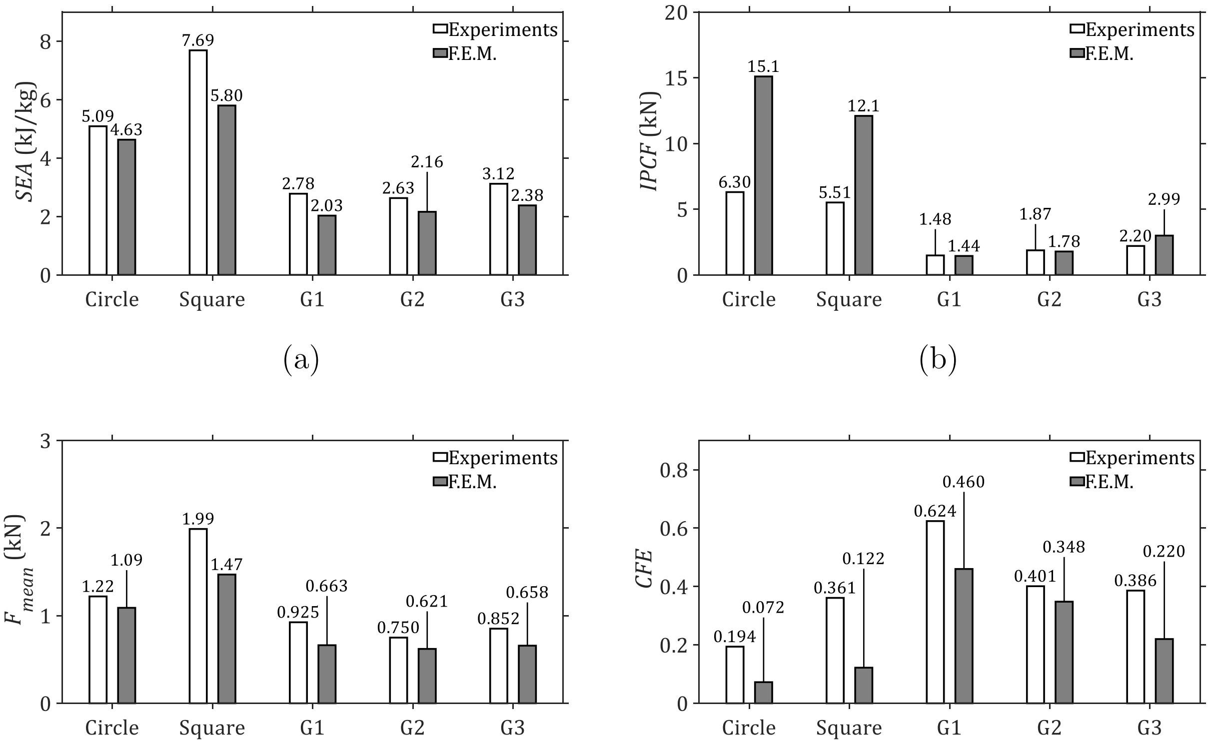

(a) (b)

(c) (d)

Figure 2.17: Comparison of (a) SEA, (b) $IPCF$, (c) F_{mean}, and (d) CFE from the experimental and numerical results between the thin-walled composite tubes.

2.5 *Conclusions*

This chapter's investigation introduced a novel filament winding method for fabricating CFRP thin-walled tubes pre-folded in the Kresling pattern. The method reduces the complexity and cost of manufacturing pre-folded tubes, while possibly limiting the structural performance of the tube. We manufactured three of these tubes with differing geometries and demonstrated their experimental quasi-static axial crushing behavior. Their response was compared to that of a circular and square tube manufactured from the same method. The experimental data was used to develop a finite element model with the ability to reproduce important trends observed experimentally.

Through the experimental and numerical approaches, we showed that the initial peak forces were significantly reduced using the Kresling origami architecture. Also, the Kresling origami tubes tested did not exhibit superior energy absorption capabilities. However, they did possess a greater crushing force efficiency compared to conventional tubes. This means that the Kresling origami tubes have less load variation and a more stable collapse. Additional findings suggest a smaller twist angle increases the stiffness of a Kresling origami tube because of decreased leaning of the facets from the direction of loading. This also increases the energy absorption per mass of the tube because it exhibits increased facet bending. With a larger twist angle, more of the load is resisted by folding of the creases. When this happens, the crushing force efficiency and load uniformity of the tube improves. Increasing the height can also result in more facet bending and a decrease in crushing force efficiency. Increased height may not provide improved energy absorption per mass. Overall, it is shown that the geometry with the smallest unit cell height and largest twist has the largest crushing force efficiency of the three Kresling origami tubes. These additional findings are preliminary due to the limited number of samples fabricated and tested in this study.

Our next step is to conduct a comprehensive parametric study to acquire more data on how the geometrical parameters of the Kresling origami tubes affect their compressive behavior. The results will be used to identify a more optimal Kresling origami geometry with superior specific energy absorption compared to conventional tubes.

2.6 Contribution

This chapter is based on the paper: J. O'Neil, M. Salviato, and J. Yang, "Energy absorption behavior of filament wound CFRP origami tubes pre-folded in Kresling pattern," *Composite Structures* 304, 116376, 2023 [70]. J. O'Neil and J. Yang conceived the idea of this project. The numerical studies were carried out by J. O'Neil. J. O'Neil also conducted the experiments and wrote the manuscript. J. Yang supervised the project. All authors contributed with valuable inputs.

Chapter 3

GEOMETRIC EFFECTS ON THE CRASHWORTHINESS OF COMPOSITE KRESLING ORIGAMI TUBES

In the previous chapter, it was shown that we could overcome the manufacturing difficulties of thin-walled pre-folded tubes using the Kresling origami architecture while simultaneously exploiting the benefits of carbon fiber reinforced plastic (CFRP) through the use of filament winding [70]. We also examined the crushing behavior of these tubes and compared their crushing behavior to that of conventional tubes without pre-folds. Only a limited number of Kresling origami tubes were used to demonstrate a stable cascading collapse of the composite tubes fabricated with the proposed manual filament winding method. The Kresling origami tubes were capable of smoother collapses but did not have as much energy absorption compared with the tested cylinders. Hagiwara's research group has studied the energy absorption of metal Kresling origami tubes and has proposed methods to manufacture them [47, 48, 51, 52]. Wang *et al.* studied optimization of multi-cell Kresling origami tubes for crashworthiness [53], and Li *et al.* performed a numerical parametric study of the Kresling origami tubes as well [50]. All of these Kresling origami studies for energy absorption were performed based on numerical methods using ductile metal material properties. It is notable that the energy absorption in the crushing behavior of a thin walled-tube made from brittle composite materials is different from that in a ductile tube because of different failure modes. Despite this, these previous studies revealed the potential for Kresling origami to absorb more energy per mass than straight-walled tubes by properly tuning the geometry of the tubes.

In this chapter's investigation, we numerically conduct a parametric study on CFRP Kresling origami tubes to understand the geometric parameters on the crushing behavior, such as twist angle, the height of unit cells, the number of sides of the cross-section, and the number of unit cells in a tube. We fabricate three composite Kresling origami tubes with different geometries and experimentally validate their crushing behavior and energy absorption characteristics. In this investigation, we characterize the crushing behavior by adopting three performance indicators: the initial peak crushing force, the specific energy absorption, and the crushing force efficiency and compare the indicators of the Kresling origami tubes with those of CFRP cylinder tubes.

3.1 Kresling Origami Tubes and Geometric Parameters

In this section, we introduce the geometry of the Kresling origami tubes (Section 3.1.1) and provide an overview of how we use the geometric parameters to study their effects on the crushing behavior of the tubes (Section 3.1.2).

3.1.1 Kresling Origami Tube

A Kresling origami tube with N unit cells stacked from bottom-to-top is depicted in Figure 3.1a. Each unit cell has a height of H_{unit} and the tube itself has a total height of $H = NH_{unit}$. Each unit cell is further characterized by their circumscribed radius, R, twist angle, β, and number of cross-sectional sides n as shown in Figure 3.1b. The unit cells of the tube in Figure 3.1 have six cross-sectional sides, and the corresponding fold pattern (the valley and mountain folds) of six cells is shown in Figure 3.1c. The fold pattern is required to generate the volumetric form of the Kresling origami tube. In this study, we manufacture polyethylene terephthalate (PET) mandrel by following this Kresling pattern.

Among the geometric parameters, β is one of the most important parameters for determining the shape of the unit cells and has a limited range of values. If $\beta = 0°$, the points B and C directly overlap each other in Figure 3.1b, which means the walls of the tube are straight and thus, we no longer have a twisted Kresling origami unit cell. Alternatively, if $\beta = \frac{\pi}{n}(n-2)$, the facets of the Kresling origami unit cell are overlapping even before any compression is applied to the tube. Therefore, Kresling origami unit cells can only be defined if: $0 < \beta < \frac{\pi}{n}(n-2)$. We also define a twist rate of the unit cell, β/H_{unit}, to consider a combined effect of β and H_{unit} on the mechanical performance of a unit cell. When the twist rate approaches zero, Kresling tube becomes similar to a straight-walled tube.

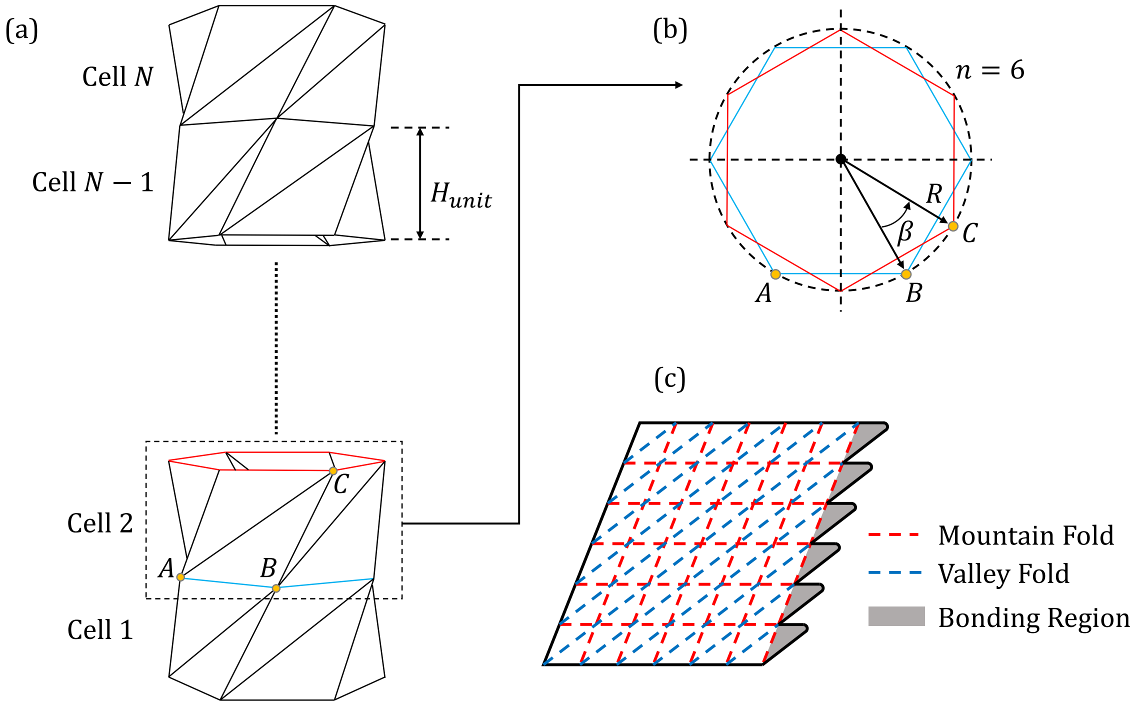

Figure 3.1: **Geometry of folded and unfolded Kresling tubes.** (a) A Kresling tube with N unit cells of height H_{unit}. (b) A cross-sectional cut of the tube showing its $n = 6$ sides, twist angle β, and circumscribed radius R. (c) Fold pattern of the Kresling tubes which depicts where mountain folds (fold outward) and valley folds (fold inward) are located. Bonding regions overlapped with facets on the other side of the fold pattern to generate a Kresling tube.

3.1.2 Geometric Parameters for Investigation

In this research, we numerically study various Kresling tubes having different β, H_{unit}, n, and N values to understand how these parameters affect the force-displacement response and specific energy absorption behavior of Kresling origami tubes. We keep $R = 36$ mm for all tubes. This radius was chosen as it provides an acceptable compromise between a realistic tube shape for crashworthiness applications and ease of manufacturing. It is also similar to radii in previous studies for the applications of impact mitigation [31, 51, 25, 71]. The tubes consist of a PET mandrel layer inside and two layers of CFRP composite wrapped outside of the mandrel. The total thickness of the composite wall is maintained around ∼1 mm for manufactured tubes. The numerical tubes have a slightly smaller thickness (0.95 mm) as we will explain when we give a detailed description of our finite element model. For a more detailed description of our manufacturing procedure, please see the "Manufacturing" section of Appendix B.1.

To investigate the role of β and H_{unit} on the mechanical response of the Kresling origami tubes, we compare nine tubes having two cells ($N = 2$) with six cross-sectional sides ($n = 6$) as shown in Figure 3.2a. There are three groups of tubes with different unit cell heights, $H_{unit} = 18$ mm, 36 mm, and 54 mm, respectively. This provides aspect ratios, H/R, of 0.5, 1, and 1.5 and allows us to see the effect of making the unit cell height smaller, similar, and larger to its radius. In each group, the tubes have three different twist angles ($\beta = 10^\circ, 20^\circ, 30^\circ$), which are relatively small twist angles. Previous papers showed that a smaller β in metal Kresling origami tubes leads to more energy absorption [50, 49]. Therefore, we limit our study to small values of the twist angle but vary the twist angle enough to understand how sensitive the compressive behavior is to this parameter. The three tubes with unit cell heights of $H_{unit} = 36$ mm are fabricated and tested to provide experimental validation of our numerical model.

We also study the role of the number of cross-sectional sides n by comparing three tubes at two different twist angles $\beta = 10^\circ$ and 30°, respectively (see Figure 3.2b). An n value of 3 was selected since this is the smallest number of sides that can be used to construct a Kresling tube. n values of 6 and 9 were chosen as these are common values to apply to Kresling shapes [71, 42] and they show what happens as we double and triple the smallest value needed to construct a Kresling tube. A β of 20° was not used for this study as we were only concerned about how the number of cross-sectional sides would be effected by the smallest and highest values of β utilized in this study. Here we keep $H_{unit} = 36$ mm, and $N = 2$ for ease of comparison.

Moreover, to understand the effect of the number of cells N in a tube with a given height, we compare two cases as shown in Figure 3.2c. In the first case, we set the twist angle of the unit cells to be all the same ($\beta = 10°$). The reason for this twist angle being selected will be discussed in Section 4.5. Thus, as the number of cells increases in a tube, the unit cell height decreases, and the overall twist rate of the tube increases. In the second case, we maintain the total twist rate in the tube by having the total twist from the bottom cross-section to the top be 10°.

The performance of our Kresling tubes is also compared with experimentally-tested straight-walled cross-ply cylinder tubes with fibers oriented 45° off the axis of the cylinders and with three heights $H = 36, 72, 108$ mm. We did not numerically simulate them due to the local-wall buckling during initial failure of the tubes which is difficult to numerically capture.

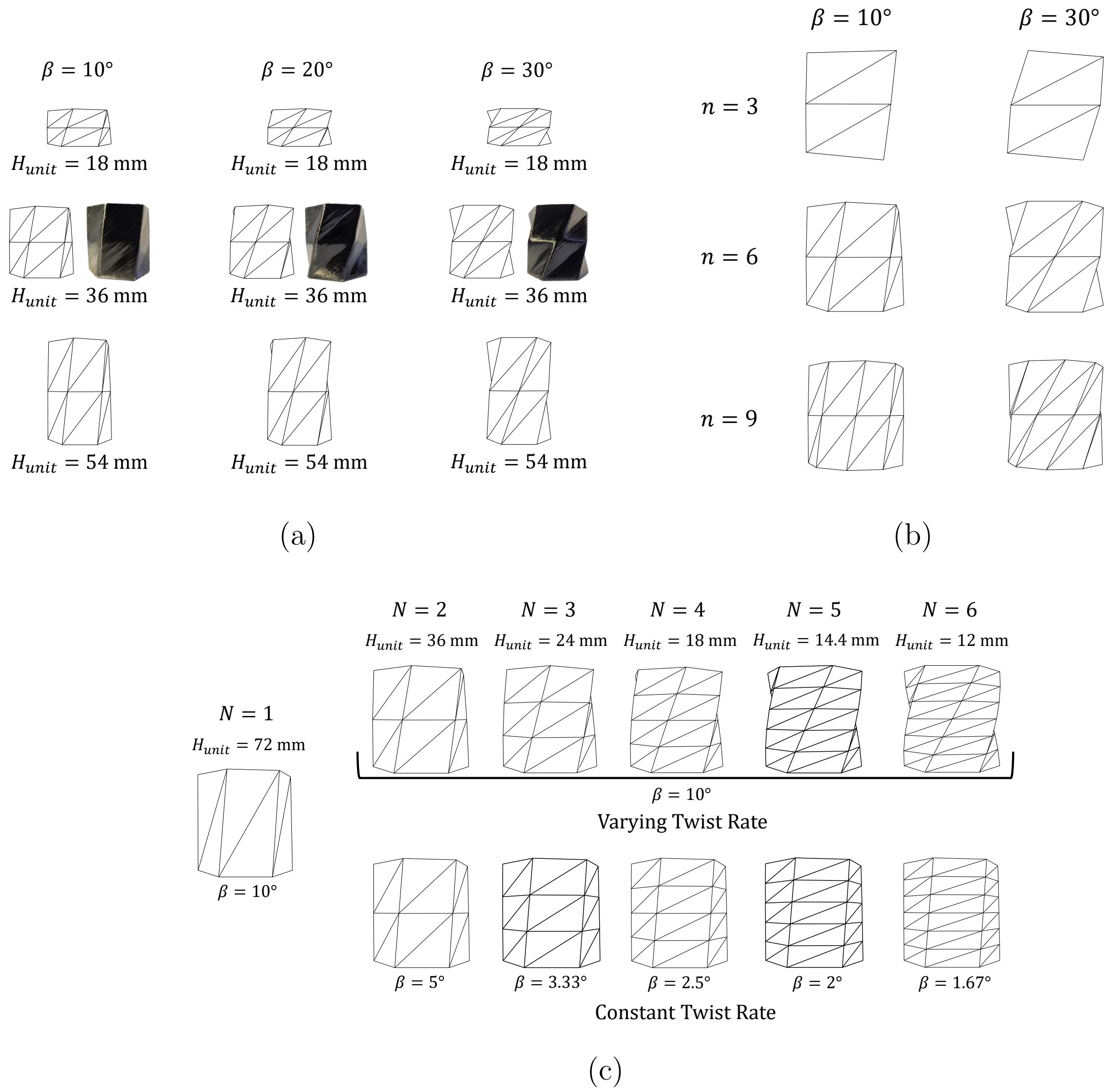

Figure 3.2: **Simulated and experimentally tested geometries.** (a) The geometric configurations for the parametric studies of the β angle (10°, 20°, 30°) and unit cell height H_{unit} (18 mm, 36 mm, 54 mm). (b) The geometric configurations for the parametric study on the number of side walls, n (3, 6, 9). (c) The geometric configurations for the parametric study on the number of unit cells, N (1 to 6). Two types of configurations are used: varying twist rate and constant twist rate. For tubes that were experimentally tested, images of the manufactured tubes are provided.

3.2 Experiment and Numerical Analysis

In this section, we first describe the experimental setup for our quasi-static experiments (Section 3.2.1). We then provide an overview of the finite element model utilized for this study (Section 3.2.2). Finally, we describe the performance indicators used to evaluate the crashworthiness of the tubes (Section 3.2.3).

3.2.1 Quasi-Static Compression Test

Quasi-static axial compression tests are utilized to validate our finite element model. The tests are conducted using an Instron 5585H electro-mechanical load frame and a 50 kN load cell as shown in Figure 3.3(a). The bottom platen was fixed to support the tube, while the top plate, connected to a 50 kN load cell, was constrained to prevent rotation during the test. The top plate compressed the tubes at a constant rate of 20 mm/min using displacement control. Given the high stiffness and low mass of the CFRP composite tubes, we assume the compression is quasi-static. While the compression rate under collision conditions can affect the crushing behavior and energy absorption of the tubes, this study focuses on the quasi-static domain to rigorously examine the effect of geometric parameters.

We experimentally tested three tubes with a unity aspect ratio ($H_{unit} = 36$ mm) and measured the force-displacement behaviors. We compared their compression behaviors and performance indicators with those obtained from numerical analysis to develop and validate an efficient numerical model.

3.2.2 Numerical Simulation

We developed our finite element (FE) model with the commercial software ABAQUS / EXPLICIT. The tubes are relatively thin compared to their other dimensions, thus we developed the model with shell elements which are less computationally expensive and more efficient to capture the overall collapse behavior of the tubes compared with solid elements. It should be noted that if one needed to simulate precise composite damage during the crushing of the tubes, a detailed solid element model would be preferable even though it requires extensive computational costs [72, 73].

In this study, we simplified our previous approach in O'Neil [70] as it was determined that cohesive contact was not necessary to capture the overall collapse behavior of the tubes since the PET does not play a major role in the energy absorption. We use only one part for the Kresling tube that is assigned a section with three materials through-the-thickness (Figure 3.3(a)). These include, from the outside to the inside of the tube, excess resin, composite layer, and the PET. The excess resin is a result of some resin not falling off of the mandrel during curing of the tube. By keeping track of the masses of each material through fabrication of the tested tubes, we can still use a micromechanics approach outlined in the supplementary material of O'Neil [70] to estimate the elastic properties of the composite layer, given in Table 3.4. The elastic properties of the resin are provided by the manufacturer [56]. The thickness of the excess resin and PET is 0.2 mm. The composite thickness is 0.45 mm in the top unit cell and decreased by about 5% in the bottom unit cell to ensure a cascading collapse without loss of generality. If more unit cells are present, the thickness of each one is uniformly reduced until there is a 5% reduction in the bottom unit cell. In reality, the thickness in the manufactured tubes vary and the first unit cell collapse is determined based on which one has less stiffness. The Kresling tube is meshed with four-node reduced integration shell elements (S4R). Through a mesh convergence study, it was determined that a global mesh size of 2 mm was a sufficient compromise between computational cost and accuracy.

The PET material is assigned with an elastic modulus of E=2.25 GPa, Poisson's ratio ν=0.33, and density ρ=1400 kg/m^3. The elastic properties of the CFRP are summarized in Table 3.4. The excess resin has an elastic modulus of 2.9 GPa and a Poisson's ratio of 0.33. In addition, we take into account the damage to each material in the simulation, because we observe damage in the experiments and its effect on the crushing behavior is not negligible. For the CFRP layer, the Hashin failure criteria is used for the damage initiation and an energy-based damage evolution law with linear softening is used for the damage evolution.

For the PET layer and excess resin, Abaqus' built-in ductile damage scheme is used. We also apply the crack band model [61, 62, 63, 64, 65] to avoid spurious mesh dependency. The failure properties of the composite and PET layers are summarized in Table 3.1 and Table 3.2 respectively. The failure stresses are taken from data acquired by Performance Composites Ltd. [74]. The fracture energies were acquired from Yoon [75]. The fiber fracture energies were scaled down by half to better match experiments and the transverse tensile fracture energy was made similar to the resin's fracture energy in the model. The PET failure properties were taken from Gupta [67]. The failure properties of the resin are given in Table 4.3 and the yield strength is provided by the manufacturer [56]. We do not have data on its stress-strain behavior, so we assume it behaves elastic-perfectly plastic. The fracture energy of the excess resin was estimated until good agreement with experiments was achieved.

Table 3.1: Composite Failure Properties

Description	Variable	Value
Longitudinal Tensile Strength (MPa)	X_{1t}	1500
Longitudinal Compressive Strength (MPa)	X_{1c}	1200
Transverse Tensile Strength (MPa)	X_{2t}	50
Transverse Compressive Strength (MPa)	X_{2c}	200
In-Plane Shear Strength (MPa)	S	70
Longitudinal Tensile Fracture Energy (N/mm)	G_{1t}^c	90
Longitudinal Compressive Fracture Energy (N/mm)	G_{1c}^c	60
Transverse Tensile Fracture Energy (N/mm)	G_{2t}^c	1
Transverse Compressive Fracture Energy (N/mm)	G_{2c}^c	1.71

In the Kresling origami tube, the axial motion is coupled with twisting motion due to its folding pattern. Thus, the degree of constraint of the rotation in the boundary can affect the crushing behavior under compression. A rigid plane, modelled with four-node rigid R3D4 elements of global size 4.6 mm, is used for the bottom platen to support the tube and a fixed boundary condition is applied to it. A top plane is also modelled with rigid elements

Table 3.2: PET Failure Properties

Description	Variable	Value
PET Yield Strength (MPa)	σ_y	28.85
PET Plastic Fracture Strain (mm/mm)	$\varepsilon_{fracture,PET}$	0.0872
PET Fracture Energy (MPa)	$G_{f,PET}$	3.18

Table 3.3: Resin Material Properties

Description	Variable	Value
Resin Yield Strength (MPa)	σ_y	68
Resin Fracture Energy (MPa)	$G_{fracture,R}$	1
Density (kg/m^3)	ρ_R	1110

and is only allowed to move in a vertical direction to compress the tube. A general contact friction coefficient of 0.3 is assigned to the model. To reduce numerical instabilities, a smaller coefficient of friction between the bottom platen and the tube of 0.2 is assigned. To maintain quasi-static conditions, the tubes are compressed with a load rate of 65 mm/s.

Each tube is compressed until the beginning of densification. The data are used to calculate various performance indicators to be described in Section 3.3.

3.2.3 Performance Indicators

We characterize the crushing performance of the tubes through three key parameters. The first is the initial peak crushing force ($IPCF$), or the peak force at the initial failure of the tube as depicted in Figure 3.4 which provides an exemplary force-displacement curve for a thin-walled tube being crushed. This is a measure of the load carrying capacity of the tube as well as its stiffness and it is crucial that it is reduced as much as possible to minimize the average compressive force acting through an impact [68]. Additionally, we must compare the relative size of $IPCF$ to the mean force F_{mean} of the compressive response, also depicted in

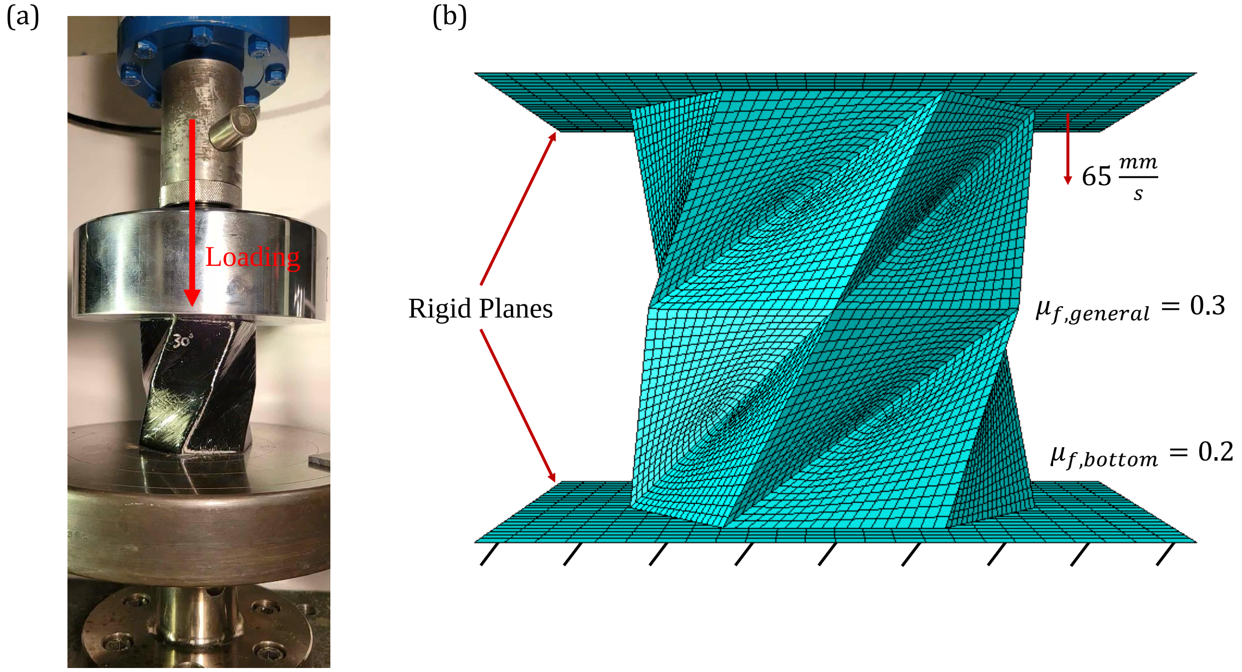

Figure 3.3: **Experimental and numerical setup.** (a) The FEM setup for quasi-static compression. (b) The experimental apparatus for the quasi-static compression tests.

Figure 3.4, as this provides for us a measure of the load variations of the force-displacement curve. To calculate the mean force, we must first calculate the energy absorption (EA) of the thin-walled tube, which is a measure of a structure's ability to dissipate crushing energy. The energy absorption can be calculated by taking the area under the force-displacement curve as shown in Figure 3.4. Mathematically, it can be given as: $EA = \int_0^{\delta_{max}} F(s)\,\mathrm{d}s$. F is the crushing force, s is the displacement path, and δ_{max} is the maximum displacement experienced by the plate at the top of the tube that is used for calculations. The mean force is then: $F_{mean} = EA/\delta_{max}$. To determine what δ_{max} should be, and to compare the axial indicators between different tubes with as much consistency as possible, we utilize the deformation efficiency, f, which is the ratio of energy absorbed to F_{max}, or the maximum force in the crushing distance, δ [18]: $f = \frac{\int_0^{\delta} F(s)\,\mathrm{d}s}{F_{max}}$. In most tubes, f will continue to increase until densification occurs. At this point, the crushing force exceeds the $IPCF$ and then f begins to drop. We set δ_{max} at the displacement where f peaks. Note that the Kresling origami tubes compress with a progressive cell cascading collapse where one unit cell is fully compressed at a time (see Section 4.1). Since the stiffness can be recovered by un-compressed unit cells during the crushing process, it is possible for f to drop before densification. Therefore, there will be multiple displacements in the compression where f drops. If this is the case, δ_{max} will be placed at the final displacement where f decreases, which corresponds to a decrease due to densification.

With δ_{max} determined, and F_{mean} and $IPCF$ defined, we can now calculate the crushing force efficiency of the tube as: $CFE = F_{mean}/IPCF$. If this value is relatively small, there are significant load variations in the force-displacement curve and compression after the initial peak may not efficiently absorb energy. The closer this value is to unity, the less load variations are present and the more effective the compression is at absorbing energy and the more stable the collapse. We strive to design tubes that make the CFE as close to unity as possible without sacrificing the structure's specific energy absorption: $SEA = EA/m$ where m is the mass of the tube. We can compare the energy absorption capabilities of tubes with different masses and structural designs by using this parameter. It is affected by both the structure's geometry and material properties. We desire to increase a structure's SEA as much as possible.

Table 3.4: Composite properties and thickness for numerical simulations

Tensile Moduli		Shear Moduli		Poisson's Ratios		Ply Thickness	Density, ρ_c
E_1 (GPa)	$E_2 = E_3$ (GPa)	$G_{12} = G_{13}$ (GPa)	G_{23} (GPa)	$\nu_{12} = \nu_{13}$	ν_{23}	(mm)	(kg/m^3)
74.4	6.33	1.97	2.09	0.264	0.510	0.45	1220

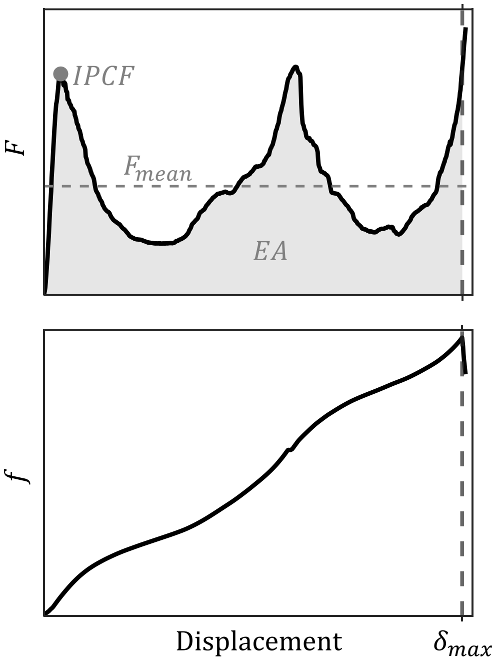

Figure 3.4: **Example force-displacement (top) and deformation efficiency (bottom) plots for an axially loaded Kresling tube with two unit cells.** The top plot identifies some important performance indicators. The bottom plot shows how to identify maximum displacement.

3.3 Results and Discussion

In this section we first validate our numerical model while also providing an overview of the crushing behavior of composite Kresling origami tubes (Section 3.3.1). We then discuss the effect of geometric parameters on the crushing behavior and energy absorption of the Kresling origami tubes using force-displacement data and performance indicators (Sections 3.3.2-3.3.4). We also compare the performance indicators of cylinders to the Kresling origami tubes. Information on the mass of these tubes can be found in the "Mass Data" section of Appendix B.2.

3.3.1 Experimental Validation and Crushing Behavior

To validate our finite element (FE) model, we compared experimental data from three tubes with a unit cell height of 36 mm against numerical simulation data, as shown in Figure 3.5. Figure 3.5(a) illustrates the comparison of crushing force-displacement profiles for the tube with $\beta = 30°$. Overall, the finite element model data aligns well with the experimental data and both demonstrate a progressive cascading collapse. We can characterize the crushing behavior of the Kresling tube by dividing it into five sections, as indicated by the numbers in the graph. The crushing shapes at these five points are compared in Figure 3.5(b). In section 1-2, linear compression occurs without damage to the tube. We observe that the linear compressive stiffness of the tubes is nearly identical between the experimental and simulation data. At point 2, critical damage begins to appear at the vertices on the bottom boundary of the tube, where stress concentration occurs due to boundary conditions such as contact with hard steel support and friction between them. Micro defects also contribute to the initial damage. The finite element (FE) simulation confirms that the first failure mode is a matrix crack. Notably, the first damage always happens either top or bottom boundaries in the experiment. In section 2-3, the damage propagates along the creases, leading to noticeable facet bending and tilting, which results in reduced axial stiffness and collapse of the bottom unit cell. Once the bottom unit cell collapse enough around point 3, the top unit cell resist the axial force and the force increases in section 3-4. Multiple peaks in FE simulation in this region is due to sudden slips between the tubes and the plates. At point 4, the vertices of top unit cell at the interface with the bottom unit cell start to shows critical damages which propagates to point 5 resulting in facet bending and tilting showing similar collapsing patterns with section 2-3. After full collapse of the two cells, densification starts to happen from point 5.

It is notable that when each cell collapses (in sections 2-3 and 4-5), the force drop is more drastic in the FE model compared to the experimental data. This is because the damage propagation along the creases occurs much faster in the FE model. Once the vertices lose stiffness, compression causes the unit cells to transition to a folded state, which is another stable state, exhibiting a snap-through-like motion. This behavior occurs in foldable bistable Kresling geometries when the vertices are free to rotate, as reported in [39, 44]. We presume that the relatively slower damage propagation at the creases in the experiment is due to less stress concentration in their curved shapes and thickness variations introduced by the manual fabrication process.

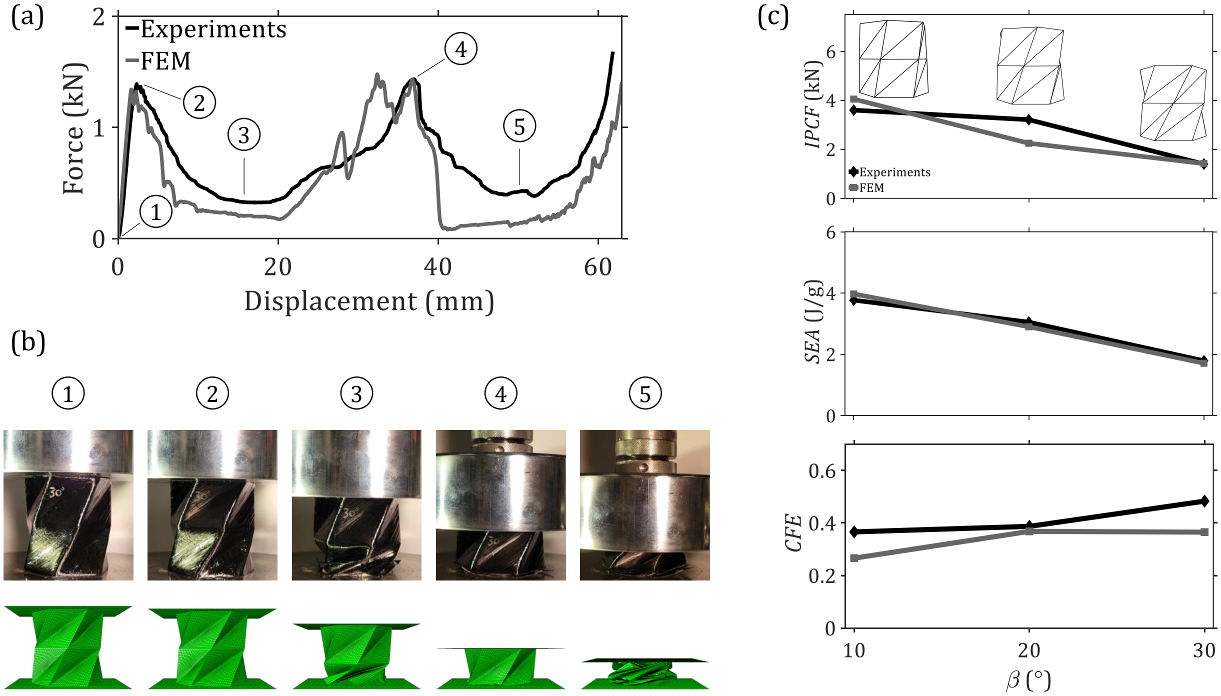

Figure 3.5: **Experimental validation of numerical model and cascading collapse.** (a) Comparison of the experimental and numerical force-displacement curves with important points along the curve labelled. (b) The collapse modes of the tube at the labelled points. (c) The performance indicators of the experimental and numerical tubes.

Figure 3.5(c) compares three performance indicators ($IPCF$, SEA, and CFE) of the three tubes with different β angles. The numerical results agree well with the experimental data. The effects of β on the crushing performance will be discussed in the following section.

3.3.2 Effects of β and H_{unit}

β is an important parameter that generates the twist in the Kresling unit cells under compression. If $\beta = 0°$, the tubes become straight-walled, with no geometric coupling between axial and twisting motion. We compare force-displacement profiles for three β angle, 10°, 20°, and 30°, for each unit cell hights H_{unit} = 18, 36, 54 mm in Figure 3.6(a), (b), and (c), respectively. We observe that all of them shows cascading crushing behaviors and force magnitudes overall decreases as β increases. This is because the twist angle tends to reduce the overall stiffness of the tubes; as the twist angle is increased, the plane of the facets is less parallel with the direction of loading, and the load bearing capability of the facets decreases.

We compare the Kresling origami tubes and cylinders in Figure 3.7(a) using performance indicators. The axial indicators of each tested cylinder were very similar as well as the collapse behavior. Therefore, we averaged their data and provide the mean behavior of these tubes with their respective standard deviation envelope. We observe that all of the $IPCF$'s of Kresling origami are less than that of a cylinders and that the $IPCF$ drops as β increases due to decreasing axial stiffness. This effect is also observed in SEA; as the twist angle is increased, the amount of energy absorption decreases due to the decrease of force magnitude during its crushing up to the same compression displacement. As the twist angle increases, the unit cell collapse shifts from exhibiting significant facet bending and crease folding to more emphasis on crease folding which reduces an important absorption mechanism. The cylinder's exhibited larger variations in their SEA values as their full compression depends on minor defects and the local-wall buckling pattern triggered [76, 77, 78, 79]. Notably, the Kresling origami tubes with $\beta = 10°$ all have similar amounts of SEA with the cylinders, falling within the standard deviation envelope. Based on the results, the twist angle has a significant role in determining the energy absorption of composite Kresling origami tubes. Increasing the twist angle by 10° can reduce the specific energy absorption by almost 40%. A clear trend of CFE with respect to β is not observed. This is because the $IPCF$ and mean crushing force decreases together with β increase. Interestingly, at the largest unit cell height, β does not appear to affect the CFE and the CFE itself is maintained within the envelope of the cylinder data.

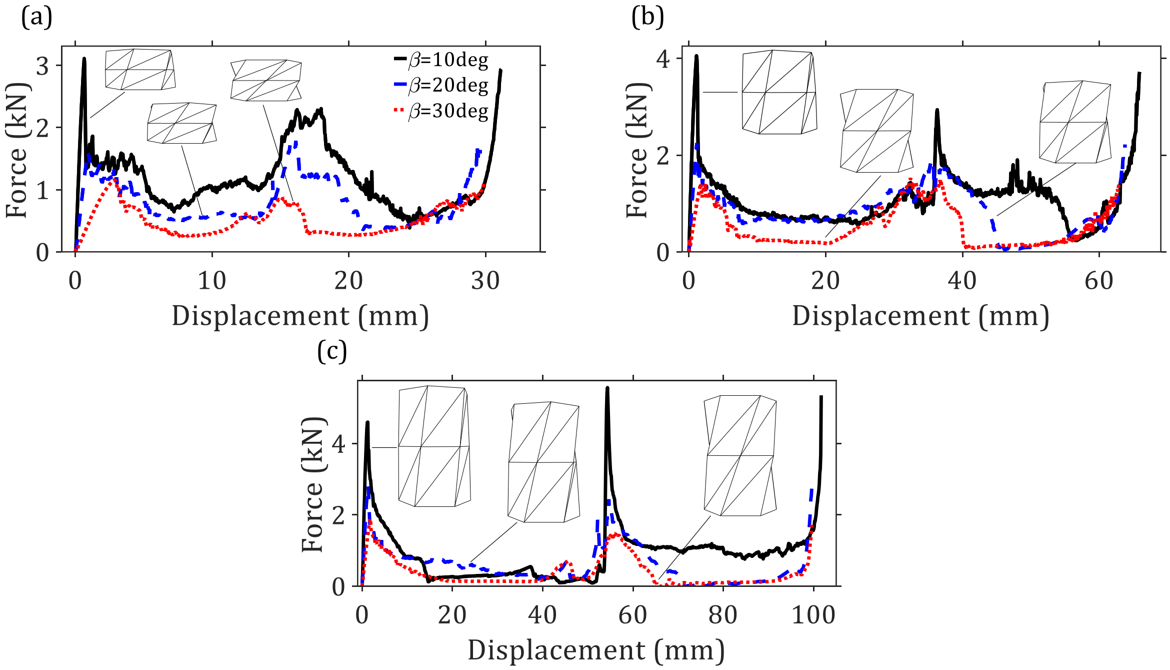

Figure 3.6: **Force-displacement results for Kresling origami tubes in the β and H_{unit} study.** The force-displacement of (a) $H_{unit} = 18$ mm, (b) $H_{unit} = 36$ mm, and (c) $H_{unit} = 54$ mm are depicted. Insets showing the geometry of each tube are provided.

We compare the same performance indicators in terms of unit cell heights H_{unit} in Figure 3.7(b). Here we observe that the $IPCF$ increases as H_{unit} increases. This is because the facets become more parallel with the direction of loading as the unit cell height increases at a given β angle, resulting in higher stiffness. This has an observable effect on the CFE; we observe that the CFE reduces as the unit cell height increases. Interestingly, when looking at the effects of H_{unit} on SEA, it does not appear to change it much in the smallest and largest twist angle cases. The maximum difference in the $\beta = 20°$ curve between the smallest and largest SEA is about 20%. Therefore, the unit cell height does not appear to have nearly the same effect on the energy absorption capabilities of the tubes as the twist angle does but

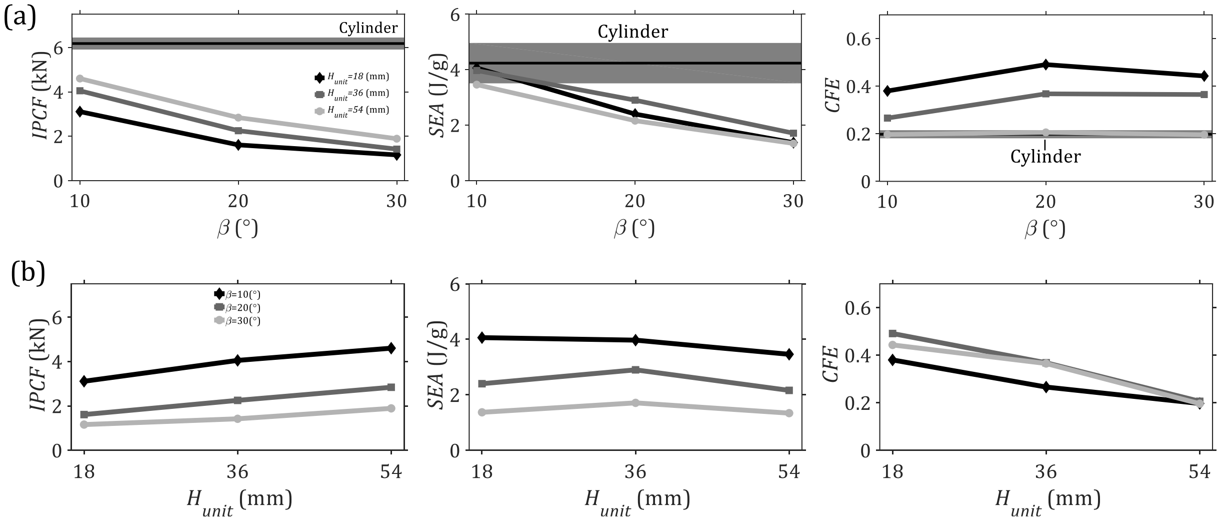

Figure 3.7: **Extracted performance indicators for Kresling origami tubes in the β and H_{unit} study.** The performance indicators are plotted with respect to (a) β and (b) H_{unit}. Cylinder data provided is averaged and a standard deviation envelope is provided.

it can affect the overall stability of the collapse.

From this parametric study, we observe that the Kresling origami tube can be designed to outperform cylinders in terms of crashworthiness. For instance, the tubes with $\beta = 10°$ show similar energy absorption per mass (SEA) while exhibiting a smaller initial peak force ($IPCF$) to composite cylinders. Furthermore, the tubes with unit cell height to radius ratios of 0.5 and 1 possess better crushing force efficiency (CFE) compared to composite cylinders. Moreover, the Kresling tube demonstrates stable and predictable crushing behavior, whereas cylinders exhibit more unstable crushing behavior with large variations in performance indicators.

3.3.3 *Effects of n*

In this section, we study the effect of the number of cross-sectional sides, n, on the crushing behavior using the models shown in Figure 3.2(b). We compare the force-displacement profiles for three cases, $n = 3, 6, 9$, at two β angles, 10° and 30°, as illustrated in Figure 3.8(a) and (b), respectively. As the number of side increases, the initial stiffness and overall force magnitude increases, which is consistent with a previous study [50]. This is because adding more cross-sectional sides decreases the initial folding angle between facets in each unit cell, which has the effect of aligning the facet walls more in the direction of loading (see the geometry in Figure 3.2(b)). We observe that the Kresling origami tube with $n = 9$ and $\beta = 10^\circ$ achieves a similar $IPCF$ to the tested cylinders. This suggests there may be a point where adding more sides to Kresling origami unit cell stiffens the tube as much or more than a cylinder.

The specific energy absorption (SEA) also increases with n due to the rise in force response. This indicates that the increase in energy absorption resulting from the higher force is more substantial than the increase in total mass as n increases (see SI). For the $\beta = 10^\circ$ case, the specific energy absorption (SEA) appears to be approaching a plateau, possibly suggesting diminishing returns after nine sides. For the $\beta = 30^\circ$ case, the overall SEA values are smaller than those of the $\beta = 10^\circ$ cases due to a softer crushing response. However, the SEA consistently increases as n increases within the range of $n = 3$ to 9. Additionally, the $n = 6$ and $n = 9$ tubes with the smaller twist angle are capable of absorbing similar amounts of energy per mass as the cylinders.

The CFE values for the three $\beta = 10^\circ$ cases are similar to each other, indicating that the initial peak force and average force magnitude increase at a similar rate. Their CFE values are also similar to that of the tested cylinders. For the $\beta = 30^\circ$ cases, the CFE values for $n = 6$ and 9 are similar, while the value for $n = 3$ is larger than those for $n = 6$ and 9.

3.3.4 Effects of N

In this section, we study the effects of the number of unit cells N under a constant tube height. There are two ways we vary the number of unit cells; the first case is varying N keeping the twist angle of the unit cell β constant (the twist rate of the whole tube increases as N increases), and the second case is varying N keeping the total twist rate of the whole

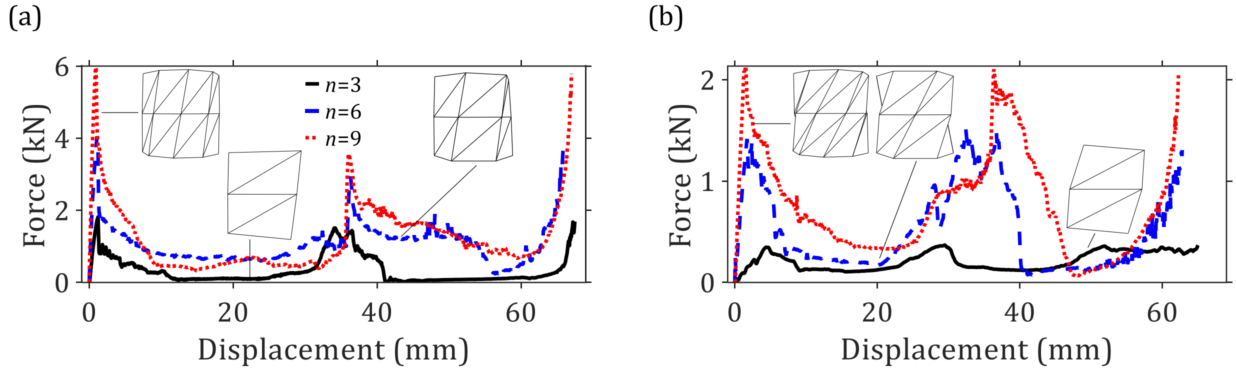

Figure 3.8: **Force-displacement results for Kresling origami tubes in the n study.** We separate the plots by twist angle (a) $\beta = 10°$ and (b) $\beta = 30°$. Insets showing the geometry of each tube are provided.

tube constant (the twist angle of the unit cell decreases as N increases).

We first look into the varying twist rate case whose force-displacement profiles are in Figure 3.10(a). They have the same tube height of 72 mm and the unit cell's twist angle of $\beta = 10°$. We use this twist angle since it has been shown to provide the most SEA out of the twist angles tested and we explore if changing the number of unit cells will improve the energy absorption performance. The model with one unit cell ($N = 1$) shows the highest initial peak force followed by a drop in the force until densification begins due to having the smallest twist rate of the tubes. With only one unit cell, the tube is unable to recover any stiffness before densification. As we increase unit cells, the initial peak force decreases because the total twist rate increases with the number of cells (see $IPCF$ in Figure 3.11). We observe cascading collapse of the unit cells under compression, which results in multiple peaks (force rising) before the tube is completely collapsed. This elevates the tube's energy absorption capability. However, as the number of unit cell increases, overall stiffness of the tube decreases due to the increase of the total twist rate, which eventually negatively affects the energy absorption capability. This makes that SEA increase up to $N = 4$ and then

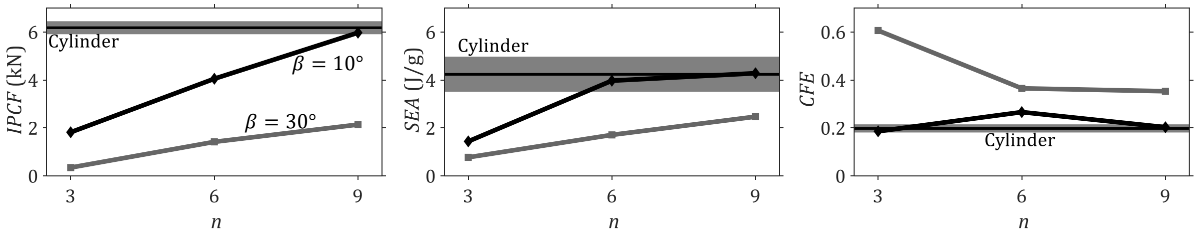

Figure 3.9: **Extracted performance indicators for Kresling origami tubes in the n study.** Included in each plot are results for $\beta = 10°$ and 30°. Cylinder data provided is averaged and a standard deviation envelope is provided.

slightly reduced at $N = 5, 6$ due to a softening effect (see SEA in Figure 3.11). Additionally, with more unit cells, the total surface area of the tube increases and so does its mass. We can confirm the combined effects of $IPCF$ and SEA in CFE (see CFE in Figure 3.11); the CFE increases up to $N = 4$ and then it is slightly reduced. Notably, at three and four unit cells, the tube achieves greater specific energy absorption than an average cylinder with far more stability.

We also simulate the second case (varying N while keeping the twist rate of the whole tube constant). In this case, the unit cell's twist angle decreases as the number of cells N increases (see β in Figure 3.10(b)). In the force-displacement profile (Figure 3.10(b)), we observed that initial stiffness (i.e., slope before the first peak) and the first peak force does not much changes compare to the varying twist rate cases (see also $IPCF$ in Figure 3.11). This is because the overall twist rate is the same for all the tubes in this case. Notably, distinguishing multiple peaks in the force-displacement profile becomes challenging after $N = 2$. Instead, the curve remains elevated and flattens as the number of unit cells increases. The collapse behavior is also different. Although there is still a cascading collapse, the twisting deformation is absent so crease folding is not present. This results in a compression closer in behavior to straight-walled tubes but the creases prevent a full-length buckling affect allowing for a more progressive "concertina" type collapse. Interestingly, the SEA keeps increase as N increases, eventually surpassing the energy absorption of the straight-walled cylinder. We presume that if the facet area becomes smaller than that of the local buckling area of a cylindrical tube, the absorbed energy will increase, resulting in a more complex crushing shape. However, in this scenario, the initial peak force also increases together will maintain closer to the $IPCF$ of the tested cylinders. Thus, CFE is overall smaller than in the varying twist rate cases yet it still is larger than the tested cylinders, and the CFE appears to asymptotically approach a certain value.

In this parametric study, we confirm that increasing the number of unit cells within a given height of a tube, thereby decreasing the unit cell height, can overall increase the energy absorption capability. Additionally, we confirm that both the total twist rate and the unit cell's twist angle significantly affect the crushing behavior. The overall twist rate of the tube significantly influences the initial peak force, while the unit cell's twist angle has a greater effect on the multiple peak forces during cascading collapse. Notably, cascading collapse becomes less distinct when the unit cell's twist angle is too small. Based on the effects of parameters, β, H_{unit}, n, and N, on the crushing behavior of the Kresling origami tube, we propose a design direction for enhancing the crashworthiness performance compared to cylindrical tubes. For high specific energy absorption (SEA), we can design the tube to have multiple smaller unit cells with a small β angle and many cross-sectional sides n. This configuration can either exhibit cascading collapse with smaller $IPCF$ or higher $IPCF$ without distinct cascading behavior.

3.4 Conclusions

In this investigation, we conducted a parametric analysis to understand the effects of four geometric parameters on the energy absorption capability of Kresling origami CFRP thin-walled tubes and to determine if they could achieve superior crashworthiness to composite cylinders. The response of the Kresling origami tubes were compared with cylinders of the same height and radius using performance indicators. We conducted this study with a finite element model that was validated with experimental data.

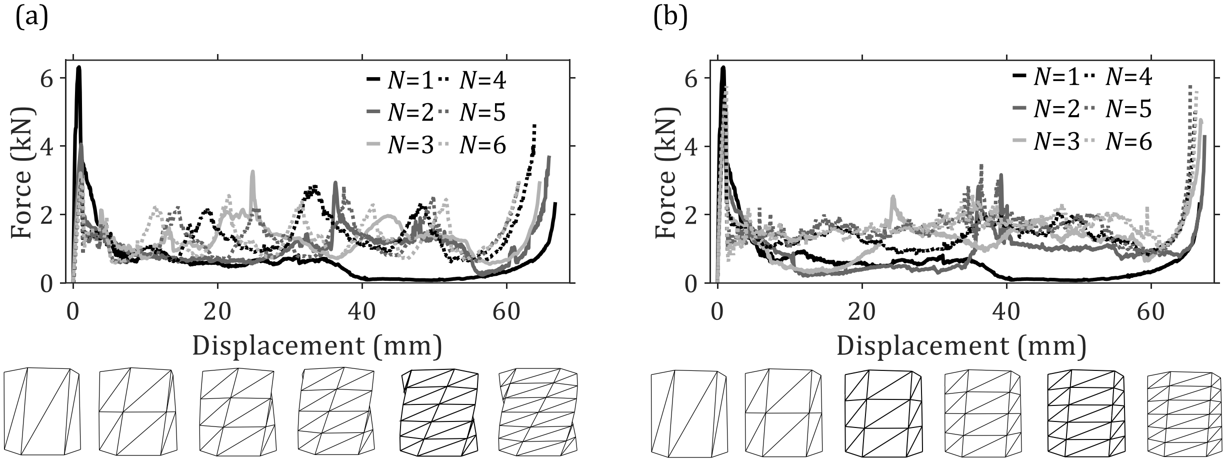

Figure 3.10: **Force-displacement curves for Kresling origami tubes with varying N.** (a) The varying twist rate case. (b) The constant twist rate case. Insets showing the geometry of each tube are provided.

If the twist angle of the Kresling tubes (β) increases, the facets become less aligned with the loading direction. Thus, the tube becomes softer and both $IPCF$ and SEA reduce. This parameter was found to have the largest impact on the energy absorption behavior of the tubes. The unit cell height was not found to affect the specific energy absorption much but did increase the stiffness of the tubes as it aligns the facets more with the loading. The number of cross-sectional sides (n) significantly affected the specific energy absorption and adding more could increase it but it could also provide tubes stiffer than cylinders. We also found that increasing the number of unit cells in a tube of given height enhances the SEA. Two distinct crushing modes were identified. When the total twist rate of the tube is relatively large, multiple cascading crushing behaviors occur due to the multiple unit cells, which increase the force magnitude and absorbed energy. Conversely, when the twist rate is relatively small, the force profile is elevated without distinct cascading crushing behavior. In this case, the $IPCF$ is also high, resulting in reduced CFE. We observe that both crushing

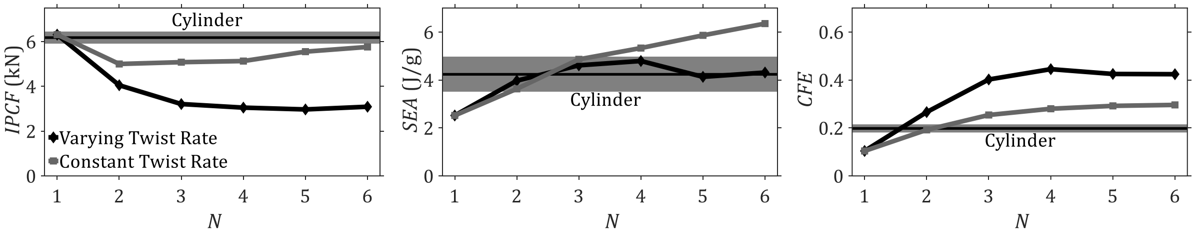

Figure 3.11: **Extracted performance indicators for Kresling origami tubes with varying N.** The results for both varying twist rate and constant twist rate cases are provided. Cylinder data provided is averaged and a standard deviation envelope is provided.

modes can be utilized to design crash tubes that outperform conventional cylindrical tubes in terms of crashworthiness.

It should be noted that the collapse behavior of the tube depends greatly on the presence on imperfections and so future work should have a focus on understanding how these can affect the performance of the tubes. Also, we need to understand the dynamic crushing behavior at various impact energies and the compression rates.

Chapter 4

COMPRESSIVE BEHAVIOR OF CONCAVE CYLINDERS DEFINED BY KRESLING GEOMETRY

In the previous chapter, we found that the number of sides of the cross-section of the Kresling origami tubes have a significant effect on the force-displacement behavior of the composite tubes. Other researchers had similar findings for numerical studies on metal Kresling origami tubes.([50, 42] and Chapter 3). As more sides are added, the stiffness of the tube increases and there is potential for increased energy absorption per mass. However, it is not clear if the energy absorption behavior is still favorable as more sides are added. These studies have only considered up to eight or nine sides at most. As we will show, as the number of sides approaches infinity, a concave cylinder, or a cylinder with negative Gaussian curvature, can be derived which is manufacturable. We will refer to these cylinders as Kresling cylinders as they have their own unique axial curvature.

Compressive studies of concave cylinders have been conducted in the past. Early investigations sought to understand the buckling behavior of toroid sections using classical linear analysis [80, 81]. These investigations found that in general, increasing the concavity of toroid sections reduced the buckling load as the curvature acted as a geometric imperfection. Haluk and Kocabas expanded on these studies and numerically derived an elastic load limit for steel concave shells after experimentally validating their model [82]. They also found a drop-off in the buckling load with more concavity, more width, and less tube height. The authors are not aware of any buckling analyses that have been conducted with anisotropic materials but as we will show with our Kresling cylinders, buckling is exhibited. With anisotropic materials such as CFRP, accurate modelling of buckling behavior in thin-straight-walled cylinders usually requires knowledge of the manufacturing imperfections of the tube [76, 77, 78, 79].

This is because buckling behavior is very sensitive to these imperfections and can reduce the predicted buckling loads of cylinders by almost 30% [83]. The energy absorption behavior of composite cone-cone intersection shells was investigated by Mahdi *et al.*. These tubes failed due to the development of cracks without any local wall buckling. Under this conditions, the researchers concluded that the concave cylinders provided super energy absorption compared with a straight-walled tube. Material failure was also the mechanism for initiating collapse in additively manufactured tubes in [84]. The concave cylinders tested were thicker than the straight-walled tubes in this investigation but they appeared to have provide more energy absorption per mass.

In this investigation, we will look at the compressive behavior of CFRP Kresling cylinders and compare their energy absorption behavior to that of a straight-walled cylinder. We utilize filament winding to fabricate the cylinders and assess the energy absorption behavior with three axial indicators: The specific energy absorption (SEA), initial peak crushing force ($IPCF$), and the crushing force efficiency (CFE). The energy absorption and collapse behavior is studied using both experiments and simulations conducted in the commercial software Abaqus/Explicit. Using these simulations, we will show that in most of the tubes, imperfections are required to capture the buckling behavior. In this study, we will also assess how the compressive behavior changes with concavity and determine if there is potential for Kresling cylinders to be used for energy absorption applications.

4.1 Derivation of the Kresling Cylinder

A standard Kresling origami unit cell is shown in Figure 4.1a. The dimensions that define the unit cell are β, the twist angle of the tube, R, the circumscribed radius of the cross-section, H_{unit}, the height of the unit cell, and n, the number of sides of the cross-section. In the figure, a six-sided unit cell is shown. When $\beta = 0°$, the unit cell is a straight-walled hexagonal tube. We set the x-axis to be along the axial direction of the unit cell.

If we allow n to approach ∞, we end up with a Kresling cylinder unless $\beta = 0°$, in which case we achieve a straight-walled cylinder. A slimmer version of the Kresling cylinder is

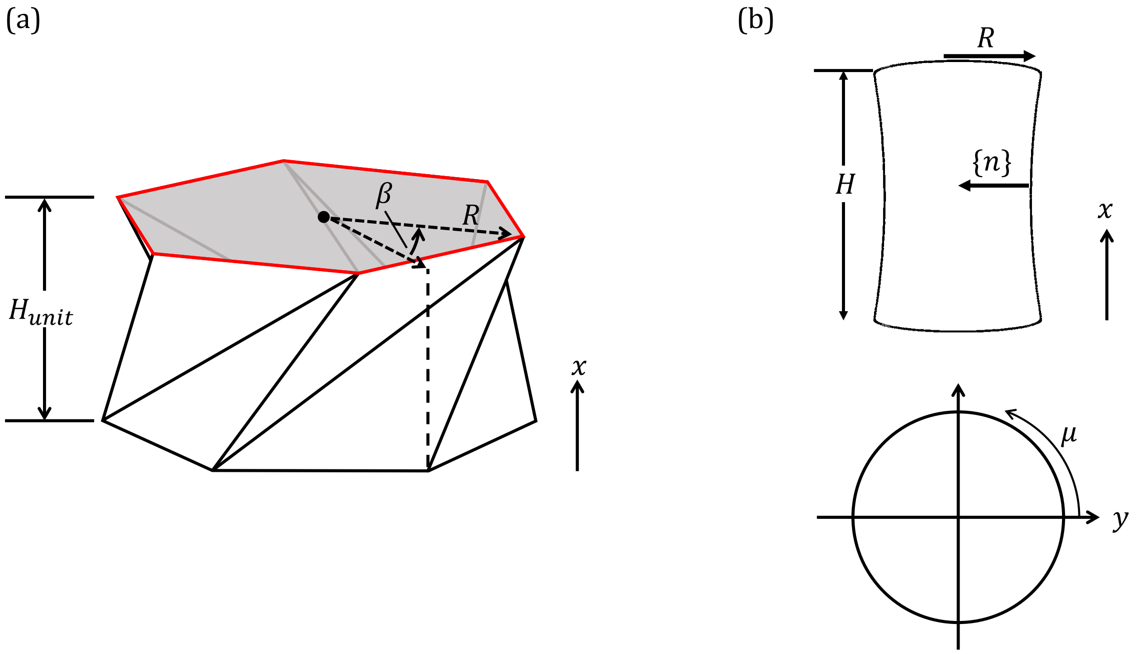

Figure 4.1: (a) A six-sided Kresling origami unit cell with important geometric dimensions labelled and (b) a Kresling cylinder with important dimensions labelled (top) and its top cross-section with μ (bottom).

depicted in Figure 4.1b. Its height will be notated as H, the normal vector at the center of the Kresling cylinder as n, and the angle that traces the circumference of the Kresling cylinder as μ. The parametric equations for the Kresling cylinder are given as:

$$\{r(x,y,z)\} = \begin{Bmatrix} x(\mu,\lambda) \\ y(\mu,\lambda) \\ z(\mu,\lambda) \end{Bmatrix} = \begin{Bmatrix} \lambda H \\ Rcos(\mu) + \lambda R[cos(\beta-\mu) - cos(\mu)] \\ -Rsin(\mu) + \lambda R[sin(\beta-\mu) + cos(\mu)] \end{Bmatrix}, \tag{4.1}$$

where $\lambda = x/H$ and is a normalized parameter that allows us to track a point along the length of the Kresling cylinder. We can show that the cross-section of the Kresling cylinder is circular everywhere along its length by squaring the second and third components of Eq.

(4.1) and adding them together:

$$y^2 + z^2 = R^2 \left[1 + 2\left(\frac{x}{H}\right)\left(\frac{x}{H} - 1\right)(1 - cos(\beta))\right], \tag{4.2}$$

In this equation, we see that the radius at the top and bottom cross-sections is equal to R and at the middle of the Kresling cylinder, the radius is equal to $R\sqrt{\frac{1+cos(\beta)}{2}}$ or $Rcos(\beta/2)$. In Eq. (4.2), if we set $z = 0$, we can derive the equation of the side walls of the Kresling cylinder that intersects the xy-plane as:

$$y = f(x) = R\sqrt{1 + 2\left(\frac{x}{H}\right)\left(\frac{x}{H} - 1\right)(1 - cos(\beta))}, \tag{4.3}$$

Eq. (4.3) is the generatrix, or the curve that when revolved about the axis of the cylinder, forms its shape. At $\beta = 0°$, the generatrix reduces to $y = R$, resulting in a straight-walled cylinder. Increasing β from here, will increase the concavity of the Kresling cylinder until $\beta = 180°$. At this β, the concavity will be very large and it is not likely to have many, if any at all, engineering applications.

4.2 Manufacturing

4.2.1 Fiber Angle Layup

In previous studies, Kresling origami tubes are wrapped so that fibers are parallel to the valley creases of length b (see Fig. 4.2) of the tubes. The angle these fibers make with respect to the horizontal c creases is θ_f. As the number of sides approaches infinity, c approaches zero and the mountain creases with length a approach the same length of the valley creases and even overlaps them. Therefore, we can keep track of θ_f and use its value as it approaches infinity, $\theta_{f,\infty}$, and calculate the winding angle with respect to the axis of the Kresling cylinder, $\theta_w = 90° - \theta_{f,\infty}$. However, we must check if we can wrap along this angle while avoiding fiber bridging along the Kresling cylinder. To do this, we adopt the methodology of Wu et al [85].

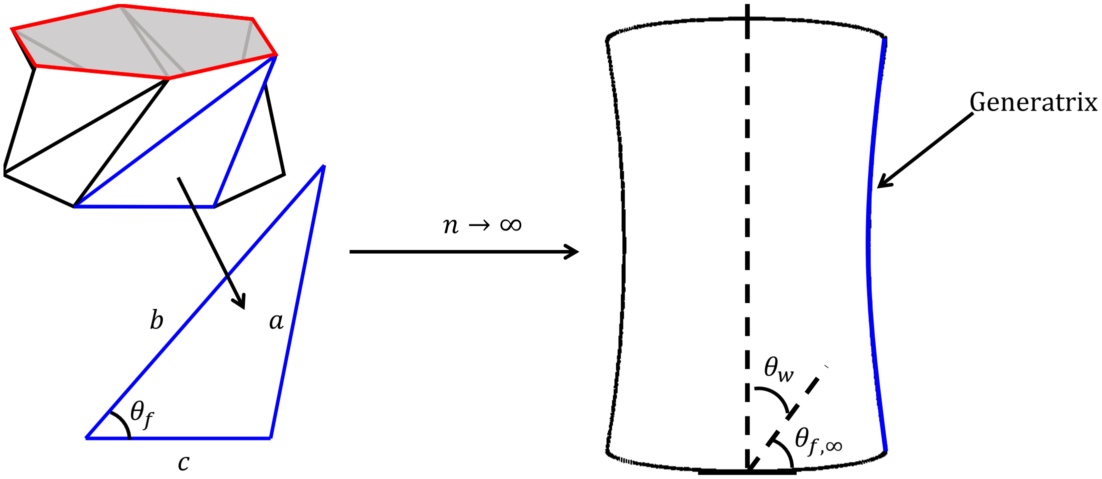

Figure 4.2: Definition of the winding angle for the Kresling cylinder.

The curvature of the Kresling cylinder changes along its length. Consequently, the smallest fiber angle that can be wrapped around the Kresling cylinder changes as we travel from one end to the next. Therefore, we calculated the minimum angle along the length and determined that the smallest angle is always at the center of the length ($x = H/2$). What we found is that for larger twist angles ($\beta > 40°$), the calculated θ_w is smaller than the calculated smallest angle that can be wrapped around the Kresling cylinder. Our goal is to be able to compare different geometric configurations in as consistent a way as possible. As a result, we decided not to use the $\theta_{f,\infty}$ for determining the winding angle.

The smallest winding angle is less than 45° in all geometries considered in this study. Additionally, preliminary research showed that wrapping these Kresling cylinders with a unidirectional layup would result in unstable fracture parallel to the fibers. This unstable fracture prevented full axial compression of the Kresling cylinders. It was decided that the layup of all Kresling cylinders would be cross-ply $\theta_w = [45°/-45°]$ with the positive 45° layer being on the inside of the Kresling cylinder. This layup provided a more stable fracture and also allowed us to more easily compare the performance of Kresling cylinders with that of straight-walled cylinders. Additionally, only two layers of fibers are considered as the Kresling cylinders are manufactured by hand with a room-temp epoxy resin that has a two-hour pot life.

4.2.2 Filament Winding Process

The Kresling cylinders are manufactured using a modified version of the filament winding approach for Kresling origami tubes [70]. A carbon fiber tow from Fibreglast [54] contained the fibers and the epoxy resin used as the matrix is the system 2000 Laminating Epoxy Resin cured with the 2120 Hardener [56]. To begin, a removable mandrel with two ends, one that screws into the other, is 3D printed (Fig. 4.3a) with PLA in an Ultimaker 3. The two ends are then assembled (Fig. 4.3b) and any significant imperfections that may affect tube geometry are sanded off. The mandrel is then carefully covered in pre-release ply to minimize wrinkles and overlaps (Fig. 4.3c). Subsequently, double-sided tape is applied along the pre-release ply to prevent fibers from slipping during the layup procedure. A 3D printed stencil that takes the shape of a section of one-half of the tube is utilized to draw +45° lines around the tube (Fig. 4.3d) so that the first fiber layer can be correctly wrapped (Fig. 4.4a).

The first fiber layer is secured using masking tape on both ends of the mandrel. After the first fiber layer is wrapped, another 3D printed stencil that possesses the -45° path is utilized to draw lines for the second fiber layer (Fig. 4.4b). Epoxy resin is applied over the first fiber layer using a China bristle brush (Fig. 4.4c). Another fiber layer in the -45° direction is wrapped and more resin is applied to the outside of the tube (Fig. 4.4d-e). The wetted tube is placed in a convective oven with the same cure cycle outlined in O'Neil [70] (Fig. 4.4f). After curing, the ends of the composite layer are removed with a wet tile saw (Fig. 4.4g) and the mandrel is removing using a vice grip and c-clamp (Fig.4.4h). Pre-release ply still attached to the tube is removed and the tube is ready for testing.

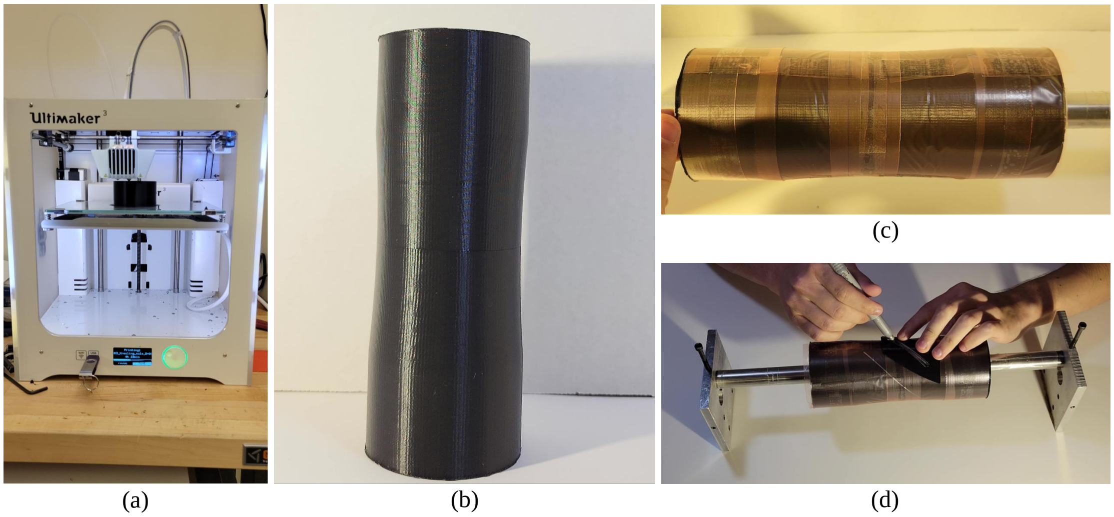

(a) (b) (c) (d)

Figure 4.3: The steps to fabricate and prepare the mandrel for wrapping. (a) 3D print both halves of mandrel that has Kresling cylinder's geometry. (b) Assemble 3D printed halves. (c) Wrap mandrel with pre-release ply and apply double-sided tape to parts of the mandrel for fibers to attach to. (d) Use 3D printed stencil to apply 45° lines.

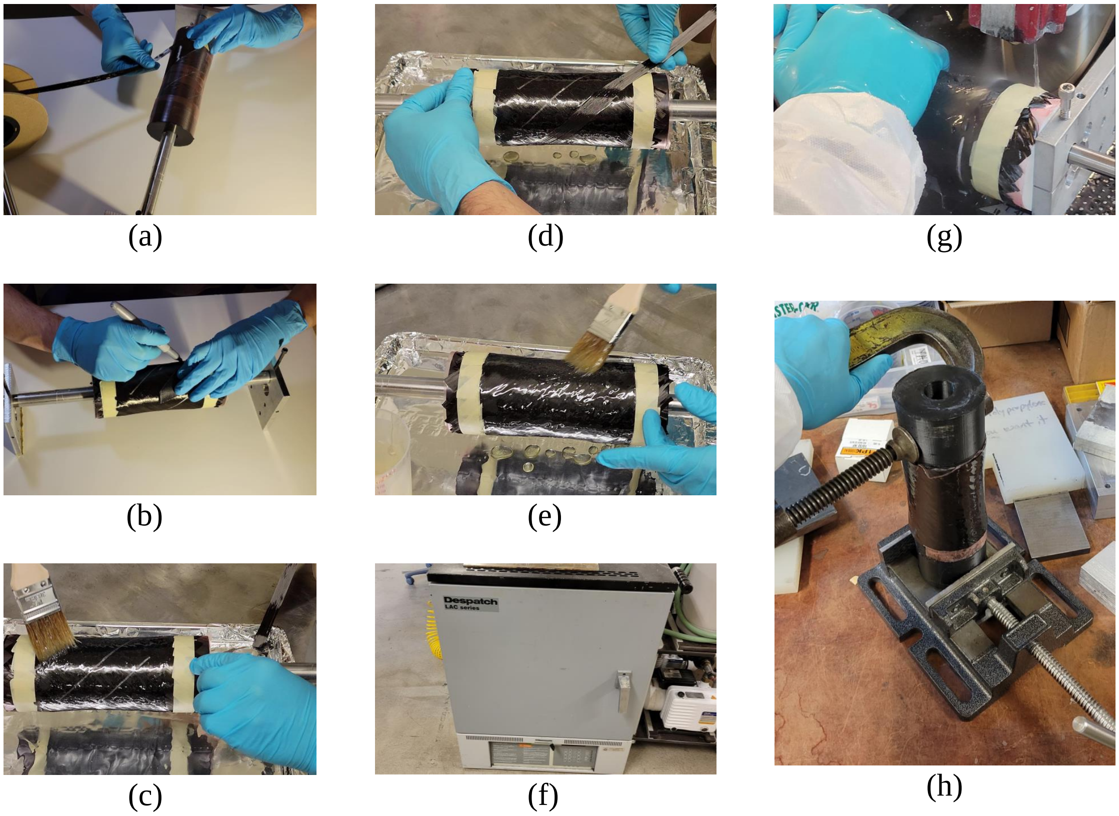

(a) (b) (c) (d) (e) (f) (g) (h)

4.3 Methods of Investigation

In this section we detail the approaches we take to investigating the energy absorption behavior of the composite Kresling cylinder. We begin by outlining the axial indicators we will use to evaluate the energy absorption behavior of the tubes (Section 4.3.1). We then provide an overview of the experimental testing procedure of this study (Section 4.3.2) as well as a description of the finite element model we use to get a deeper understanding of the compressive behavior (Section 4.3.3). Finally, we end this section by describing the geometric configurations we tested for this investigation (Section 4.3.4).

4.3.1 Axial Indicators

The energy absorption behavior of the tubes are evaluated through three key axial indicators: The initial peak crushing force ($IPCF$), the crushing force efficiency (CFE), and the specific energy absorption of the compression (SEA). Fig. 4.5 depicts an example force-displacement curve for an arbitrary tube. For this study, δ_{max} is set to 80 mm to avoid the densification region of the curve.

The $IPCF$, as shown in Fig. 4.5, represents the initial failure load of the Kresling cylinder. The $IPCF$ can be used as a measurement of the stiffness of a tube under compression as well as its load carrying capacity. We must compare the $IPCF$ to the average compressive force of the tube, F_{mean} (labelled in Fig. 4.5), using the crushing force efficiency, $CFE = \frac{F_{mean}}{IPCF}$. The CFE is an indicator of the smoothness and stability of the collapse of the tube. The closer the value is to unity, the more progressive the collapse is. The smaller the value gets, the more load variations there are during collapse. In order to calculate the mean force, we need the area under the curve which represents the energy absorption of the tube, $EA = \int_0^{\delta_{max}} F(s)\,\mathrm{d}s$ (labelled in Fig. 4.5). s is a dummy variable for the displacement in this expression and δ_{max} is the maximum compressive displacement (labelled in Fig. 4.5). EA is a measure of the cylinder's ability to dissipate crushing energy. The mean force is then calculated as $F_{mean} = EA/\delta_{max}$. EA is also used to track the last important axial

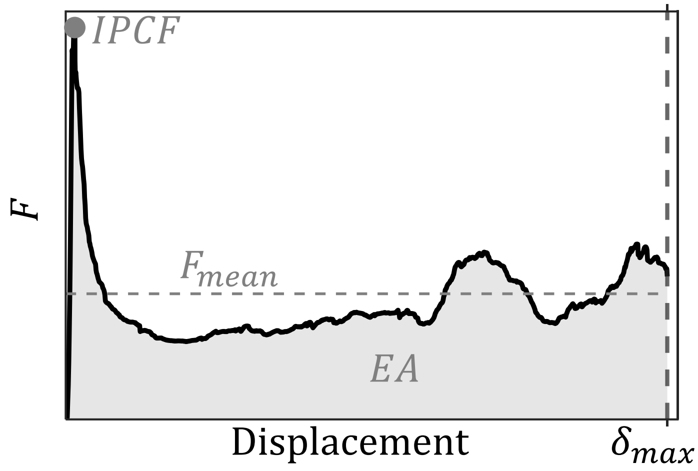

Figure 4.5: An example force-displacement curve with two of the three axial indicators used to evaluate the energy absorption behavior of composite Kresling cylinders.

indicator, the specific energy absorption. The calculation is $SEA = EA/m_{tube}$ where m_{tube} is the mass of the tube. This indicator allows us to compare the energy absorption of structures of different masses and geometric designs. It is desired to make this value as high as possible. Using SEA is important for this study since we will compare the energy absorption behavior of manufactured and simulated tubes. The manufactured and simulated cylinders have thicknesses and masses that differ slightly between each other.

4.3.2 Experimental Approach

Experimental compression tests are conducted with an Instron 5585H electromechanical load frame and a 50 kN load cell with closed-loop control. The compression is displacement-controlled and ended until either densification is triggered or until a cylinder no longer is exhibiting complete axial compression. As shown in Fig. 4.6a, cylinders are simply rested on top of a fixed platen while another platen above the tube applies compression. The rate of compression is 10 mm/min. Due to the high stiffness and low mass of the cylinders, we assume this load rate provides a quasi-static response. We restrict ourselves to the quasi-static realm in this study in order to focus on the qualitative energy absorption behavior of the cylinders without strain-rate dependency. Additionally, we sought a smaller load rate than in our previous studies on Kresling origami tubes [70] as a result of buckling mode shapes that appear during compression in these cylinders. We desired to carefully capture this buckling pattern with a slow motion camera for further study.

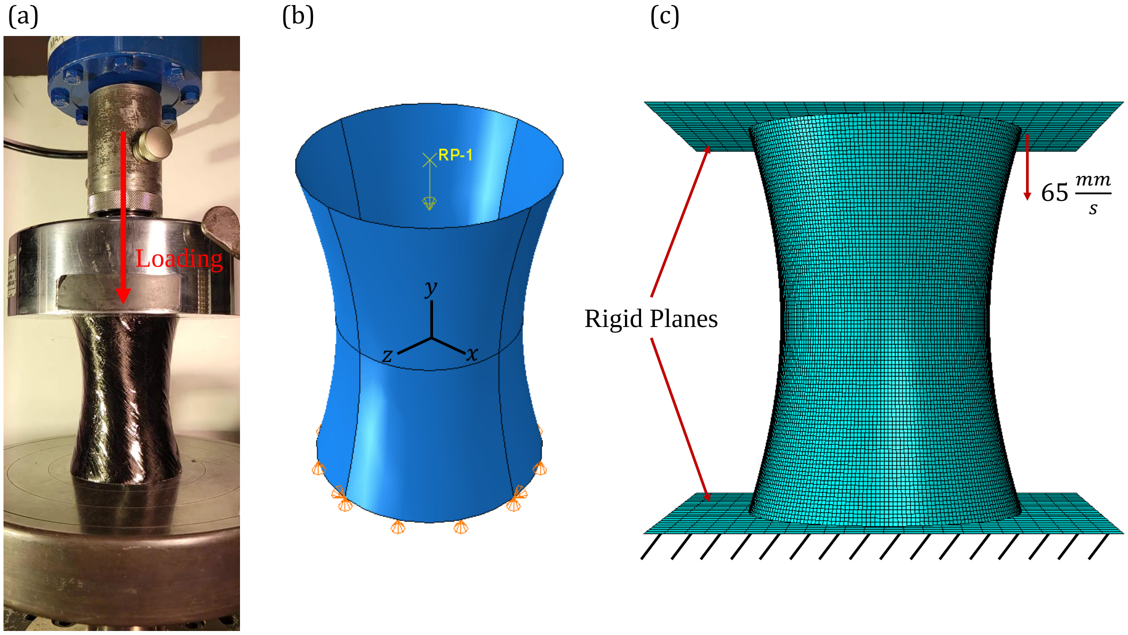

Figure 4.6: (a) The apparatus used for quasi-static compression tests. The bottom platen is fixed and the top platen applies compression. The Kresling cylinder rests simply on the bottom platen. (b) The setup for the linear-buckling analysis that is used to seed imperfections for the full-compression model. (c) The setup for the full-compression model of the cylinders with boundary conditions and load rate provided.

4.3.3 Finite Element Model

To determine if the experimental behavior of the cylinders can be numerically captured, with the potential to be studied further, we utilize a finite element model developed with the commercial software Abaqus/Explicit.

In the model, two materials are incorporated: the composite formed from filament winding and the excess resin on the outside of the composite which did not come off of the cylinder during curing. This excess resin could not be ignored as it is approximately 50% of the thickness of a cylinder. Each cylinder is assigned a composite section that that has two 0.15 mm layers of composite material, with one oriented in the $+45°$ and $-45°$ directions. The excess resin is applied to the outside and assigned 0.3 mm of thickness. In reality, the thickness of our tubes vary but their average thicknesses are 0.62 ± 0.11 mm. To estimate the elastic properties of our cylinders, micromechanics models were employed, similar to those outlined in O'Neil et al [70], with the exception of reducing material properties by 20% to account for imperfections. The elastic properties utilized for simulations are given in Table 4.1. The strength and damage properties of the composite sections are also provided in Table 4.2. The resin material properties are given in Table 4.3 and are taken from the data sheet provided by the manufacturer [86]. The damage initiation of the composite layers are governed by the built-in Hashin failure criteria while an energy-based linear-softening approach dictated the damage evolution. The resin was treated as an elastic-perfectly plastic material due to the absence of significant fracture in the tubes.

Table 4.1: Composite properties and thickness for numerical simulations

Tensile Moduli		Shear Moduli		Poisson's Ratios		Ply Thickness	Density, ρ_c
E_1 (GPa)	$E_2 = E_3$ (GPa)	$G_{12} = G_{13}$ (GPa)	G_{23} (GPa)	$\nu_{12} = \nu_{13}$	ν_{23}	(mm)	(kg/m^3)
74.4	6.33	1.97	2.09	0.264	0.388	0.15	1220

Table 4.2: Composite Failure Properties

Description	Variable	Value
Longitudinal Tensile Strength (MPa)	X_{1t}	750
Longitudinal Compressive Strength (MPa)	X_{1c}	600
Transverse Tensile Strength (MPa)	X_{2t}	50
Transverse Compressive Strength (MPa)	X_{2c}	250
In-Plane Shear Strength (MPa)	S	35
Longitudinal Tensile Fracture Energy (N/mm)	G^c_{1t}	90
Longitudinal Compressive Fracture Energy (N/mm)	G^c_{1c}	60
Transverse Tensile Fracture Energy (N/mm)	G^c_{2t}	0.3
Transverse Compressive Fracture Energy (N/mm)	G^c_{2c}	1.71

Table 4.3: Resin Material Properties

Description	Variable	Value
Elastic Modulus (GPa)	E_R	2.9
Poisson's Ratio	ν_R	0.33
Yield Strength (MPa)	σ_y	68
Density (kg/m^3)	ρ_R	1110

Each cylinder is meshed with four-node reduced-integration (S4R) shell elements which were selected because thickness of the tubes is relatively small compared to their size. To ensure a uniform structured mesh, the cylinders are partitioned into eight regions that bisect the cylinders in the $xy-$, $xz-$, and $yz-$ planes. A mesh convergence study revealed that a global mesh size of 1 mm was a sufficient trade-off between simulation time and accuracy.

As it will be shown in a later section, most of the geometries tested have an initial failure due to local-wall buckling, a structural instability that a model without geometric imperfections cannot capture. For these cylinders, a linear buckling analysis is conducted with the boundary conditions shown in Figure 4.6b. The bottom cross-section of the tubes are fixed in the out-of-plane direction while four individual points around the cylinders, where the partitions intersect the bottom cross-section, are also fixed tangentially to prevent rotation. The top cross-section and the reference point in the figure are given a rigid-tie constraint and the load is applied at the reference point. The first fifteen buckling loads/modes are solved for and we select only the most physically meaningful ones to seed as imperfections in a full-compression model (see Figure 4.6c). The modes selected, as well as their scale factors, are given in Table 4.4. The criteria for being physically meaningful depended on what was seen experimentally. The scale factor of the buckling mode selected as being most meaningful depended on when it showed to have some affect on the initial peak crushing force. The rest of the scale factors were reduced uniformly.

Table 4.4: Buckling modes and scale factors of the simulated tubes

$\beta(^\circ)$	Buckling Mode	Scale Factor (mm)
0	10	0.2
	11	0.175
	12	0.15
40	4	0.2
	5	0.2
	6	0.35
	7	0.35
60	1	0.2
	2	0.175
	3	0.15
	4	0.125
	5	0.1
	6	0.075
	7	0.05
	8	0.025
	9	0.02
	10	0.0175
	11	0.015
	12	0.0125

The full-compression model in Figure 4.6c is similar to the linear-buckling analysis except that the analysis type is changed to dynamic-explicit. The cylinder has its boundary conditions removed and instead is placed on top of a platen that is fixed in all degrees-of-freedom. The cylinder is crushed by a top-platen, which is restricted to only move vertically, that is given a load-rate of 65 mm/s which was selected as it provided reasonable simulation times while keeping the kinetic energy under 10% of the internal energy of the model. Both platens are meshed with rigid elements that have a global size of 4.6 mm. A general contact algorithm was applied to the model with a friction coefficient of 0.25.

4.3.4 Geometries studied

In this study, we look at five geometric configurations of the Kresling cylinder through both approaches. All five cylinders have a total height of $H = 100$ mm and an outer radius radius of $R = 36$ mm. The outer radius was selected to maintain some consistency with the Kresling origami tubes of our previous studies [70] while the height was selected based on a tradeoff between feasible shapes we could 3D print and that could be compressed without inducing Euler buckling modes. From here, we decided on four one-unit-cell geometries with β values of 0°, 40°, 60°, and 80°. A β of 0° is just a straight-walled cylinder and acts as a control to compare other geometries against. Values of β between 0°-40° are very close in behavior to a cylinder and do not have much concavity. Therefore, we ignore them for this study. Kresling cylinders with $\beta > 80°$ are very difficult to wrap and were not considered. Finally, all cylinders have a thickness of about 0.62 ± 0.11 mm.

4.4 Discussion of Results

This section will be divided as follows: we will first discuss the collapse behaviors of each cylinder individually and discuss how well the modelling approaches captured the experimental collapse. If the numerical model provides any further insight, we will comment on that as well. Finally, we will compare the collapse behaviors between each cylinder using their force-displacement and axial indicator data.

4.4.1 Collapse Behavior

The control of our study, the straight-walled cylinder with a $\beta = 0°$, exhibited an initial failure triggered by local-wall buckling as depicted in Fig. 4.7a in an experimental test. The buckling is localized to the lower half of the cylinder and forms a near diamond-like shape that results in fracture along the upper fold lines. Often times, diamond-like buckling patterns will form throughout the length of a cylinder [76, 77, 78, 79]. However, the exact buckling mode is highly dependent on geometric imperfections, local material properties, and boundary conditions. The localized buckling allows the upper-half of the tube to recover some stiffness and elevate the rest of the force-displacement curve.

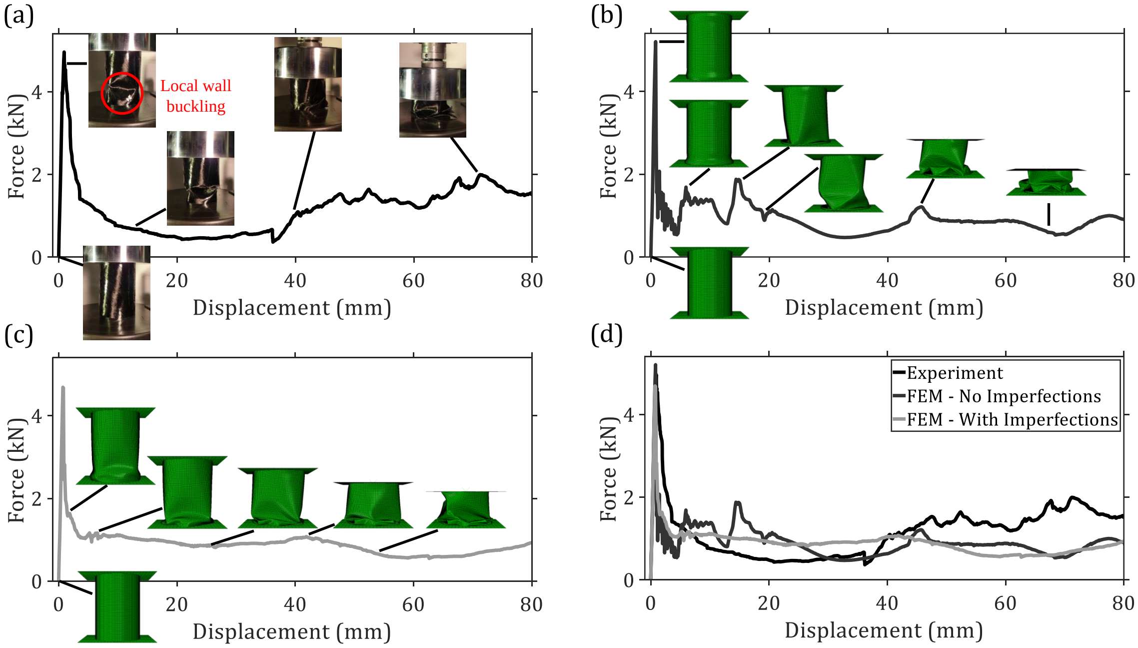

Figure 4.7: Experimental force-displacement behavior of the $\beta = 0°$ cylinder with significant deformation modes, including the initial local wall buckling mode, depicted.

From Fig. 4.7b, we notice that the initial failure of the straight-walled cylinder is triggered due to material failure by the widening and folding of the lower cross-section of the tube. Buckling is only triggered after enough compression. Therefore, buckling modes are required to properly capture this cylinder's collapse. Fig. 4.7c provides the result of seeding imperfections in the cylinder. We are able trigger buckling in the bottom portion of the cylinder as seen experimentally. The buckling pattern is not exactly captured. This represents a limitation of the model. To more accurately capture the experimental behavior, we need more information on local fiber orientation, local material properties, the thickness distribution, and boundary conditions. Despite this, the model with imperfections seeded does capture the smoother collapse seen in experiments and has good agreement in the initial peak (Fig. 4.7)d. Therefore, it does appear that this cylinder is imperfection sensitive and requires imperfections for a better predicition of its collapse.

The $\beta = 40°$ Kresling cylinder had a similar buckling pattern materialize experimentally with the appearance of near diamond-like dimples at the bottom portion of the cylinder (Fig. 4.8a). Unlike the straight-walled cylinder, the upper portion of the $\beta = 40°$ cylinder also sees the walls buckle inward on one side. The other side of the cylinder does not buckle at the top and is responsible for the elevated portion of the force-displacement curve that begins at 20 mm. The buckling mode did eventually result in the cylinder leaning and not having an axial collapse later in the compression which is where the test was ended. Other attempts to test this cylinder resulted in similar excessive leaning.

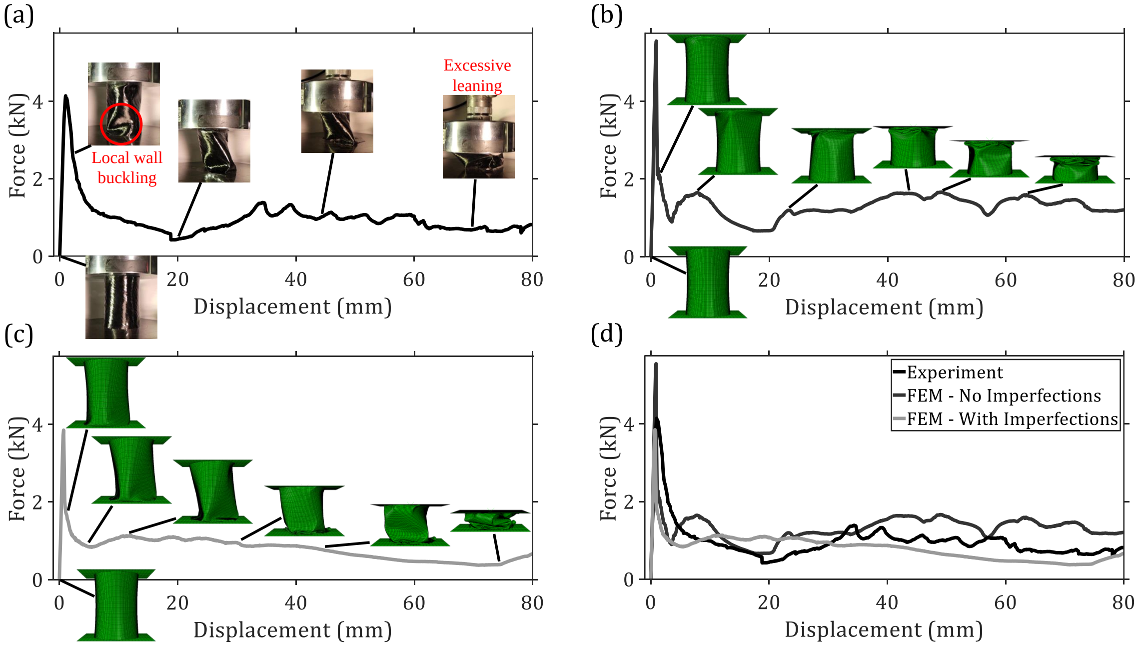

Figure 4.8: Experimental force-displacement behavior of the $\beta = 40°$ cylinder with significant deformation modes, including the initial local wall buckling mode, depicted.

Without imperfections seeded, the simulated $\beta = 40°$ cylinder shows a similar initial collapse to the straight-walled cylinder that is triggered by material failure (Fig. 4.8b). After initial failure, we observe buckling followed by a collapse of a good portion of the cylinder and more buckling in the latter part of the collapse. We notice that without imperfections, this cylinder has a larger initial peak compared with its experimental counterpart and even that of the straight-walled cylinder. This suggests that the orientation of the fibers can actually strengthen the cylinder when concavity is added. Despite this, the experimental cylinder does not exhibit the same properties. After adding imperfections, the initial peak is reduced and the collapse more closely matches the experimental cylinder, even if there is no excessive leaning (Fig. 4.8c). The force-displacement of the imperfect cylinder does appear to have better agreement with the experimental curve as shown in Fig. 4.8d.

As with the previous cylinders, the $\beta = 60°$ cylinder undergoes local-wall buckling during initial failure. Its buckling pattern is near diamond-like at both the top and bottom of the tube and its compression remains fully axial (Fig. 4.9). The buckling pattern stiffens the tube post-peak as its force-displacement response stays elevated at about half of the initial peak until approximately 30 mm of compression. Modelling the $\beta = 60°$ cylinder was difficult. As can be seen in Fig. 4.9b, with no imperfections the force-displacement response seems to qualitatively capture the elevated regions between 10-30 mm. However, its initial failure is in the materials, not due to structural instability. Even if only the axial buckling modes are selected for this cylinder, these buckling modes have to be scaled considerably to prevent the cylinder from leaning and reducing the force-displacement response considerably. Therefore, in Fig. 4.9c, all of the first 12 buckling modes of the $\beta = 60°$ cylinder are utilized and scaled in a way that achieves an axial collapse even with the presence of buckling. This does not result in a force-displacement curve that achieves good agreement with experiments (Fig. 4.9d). Other imperfections are needed to improve this result.

Finally, the $\beta = 80°$ cylinder exhibited a drastically different failure mode compared with the other geometries. Its experimental collapse did not show signs of local-wall buckling at initial failure. Instead, as shown in Fig. 4.10a, the cylinder initially fails due to stresses in the composite and resin materials. This results in the bottom cross-section spreading out and folding in on itself. This explains the presence of two smaller peaks after the initial one

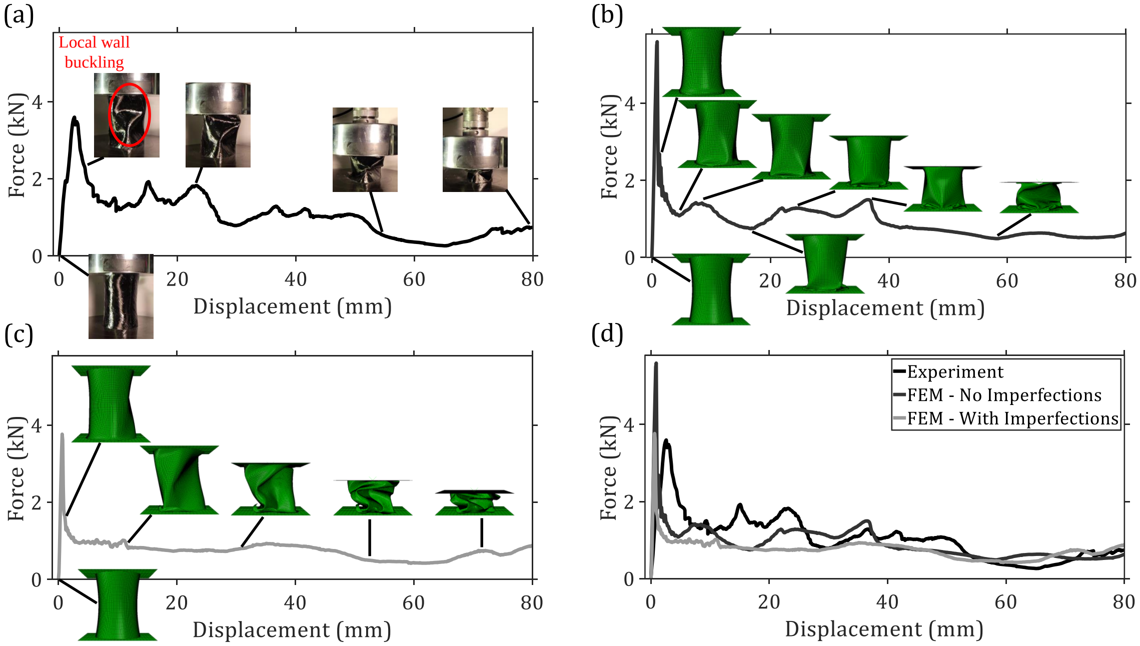

Figure 4.9: Experimental force-displacement behavior of the $\beta = 60°$ cylinder with significant deformation modes, including the initial local wall buckling mode, depicted.

as some of the cylinder that is not damaged assists in recovering the stiffness. The cylinder does eventually slide a small amount at the bottom, most likely due to asymmetries in the wall thickness around the cylinder. This results in the force-displacement curve dropping in value.

This cylinder was easier to simulate numerically. As shown in Fig. 4.10b, imperfections were not needed to capture the presence of two peaks after initial failure which allows for a more elevated region before about 30 mm of displacement. In the numerical case, the drop in load is not due to sliding but is explained by the walls beginning to buckle and fold inward. Additionally, the top cross-section also undergoes a similar widening and folding behavior as the bottom cross-section which can be explained by the absence of sliding. From Fig. 4.10c, it appears that the numerical model does exhibit overall good agreement with the experimental collapse. This suggests that the cylinder is not as imperfection sensitive as the other cylinders tested.

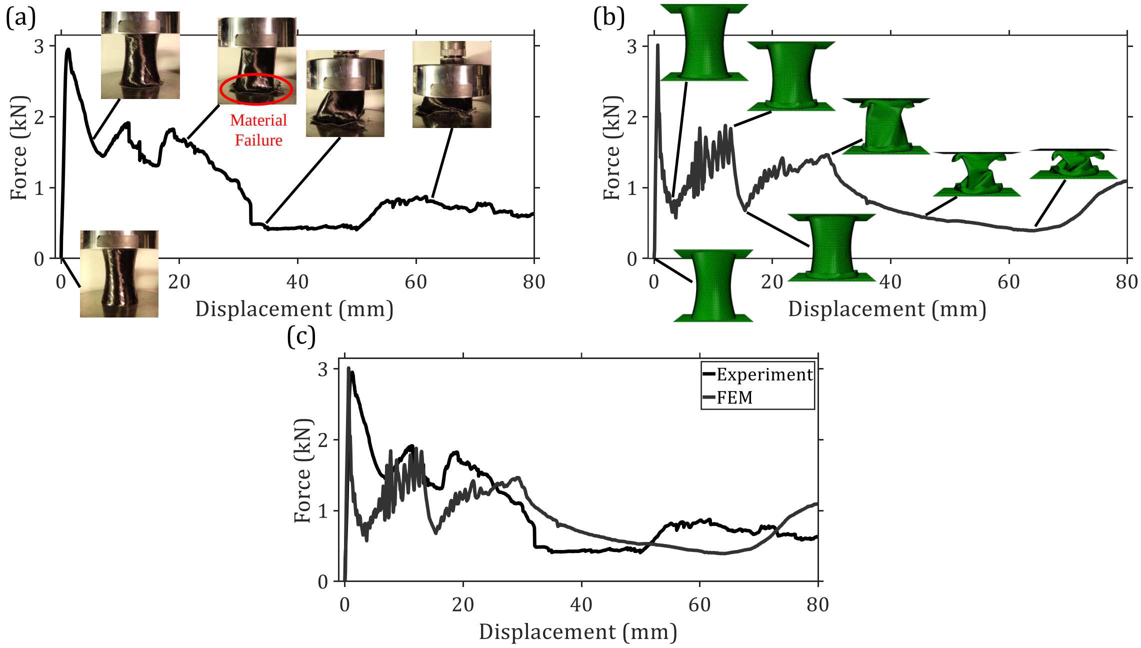

Figure 4.10: Experimental force-displacement behavior of the $\beta = 80^\circ$ cylinder with significant deformation modes, including the initial local wall buckling mode, depicted.

4.4.2 Extracted Parameters

We now compare the compressive behavior of the cylinders using both their force-displacement curves and their axial indicators extracted from the curves. The experimental force-displacement curves are superimposed in Fig. 4.11a. We can observe that the initial peak force, where initial failure occurs, appears to get smaller as concavity is increased. Also, the larger concavity Kresling cylinders possess more elevated regions after the initial peak when compared with the $\beta = 40^\circ$ and straight-walled cylinders. This implies the collapse is less progressive for smaller concavities initially. The initial peak decreasing with concavity also appears to occur in the numerical results (Fig. 4.11b). Note that in this figure, all numerical results include imperfections as these cylinders behave more closely to their experimental counterparts. Interestingly, the superimposed numerical results, with the exception of the $\beta = 80°$ cylinder, appear to behave very similar qualitatively and quantitatively. This actually appears to happen in certain displacement ranges of the experimental curves as well. Particularly up to about 35 mm of compression for the $\beta = 40°$ and straight-walled cylinders but also in different ranges after 35 mm of compression for all of the Kresling cylinders. The variability can be explained by non-uniform thickness and material property distribution in the cylinders. Additionally, the boundary conditions, especially friction, can considerably change the numerical results. Finally, although we attempt to maintain the correct fiber winding angle around the tubes, there will be some variability and the winding angle has a large role in the force-displacement response. For the model to be more predictive, we either need to have better knowledge of all imperfections to seed in the cylinders, or we need a more precise manufacturing process that can provide better consistency. The latter seems more appropriate to pursue in future work as the former requires measurements for every cylinder manufactured and simulations to be reran.

Finally, we look at the axial indicator data. From Fig. 4.11b, a few interesting trends can be noted. It appears that as the concavity is increased, the initial peak crushing force is decreased. The model even captures the values with good agreement. Despite both approaches given similar results, it should be noted that the imperfection-free simulations did not show this trend. It is possible that more developed manufacturing techniques may alter the behavior.

With the possible exception of the $\beta = 80°$ Kresling cylinder, the specific energy absorption also appears well captured by our model. The experimental trend implies that changing the concavity, at least within the bounds investigated, does not affect the specific energy absorption of the cylinders very much. Although the cylinder appears to have the largest specific energy absorption, it is only a 10% difference with the result for the $\beta = 40°$ cylinder. Therefore, no real advantage is achieved with or without the concavities tested in terms of this axial indicator. The $\beta = 80°$ cylinder does show a major advantage numerically. This is attributed to the differences in mass between the experimental and numerical versions of

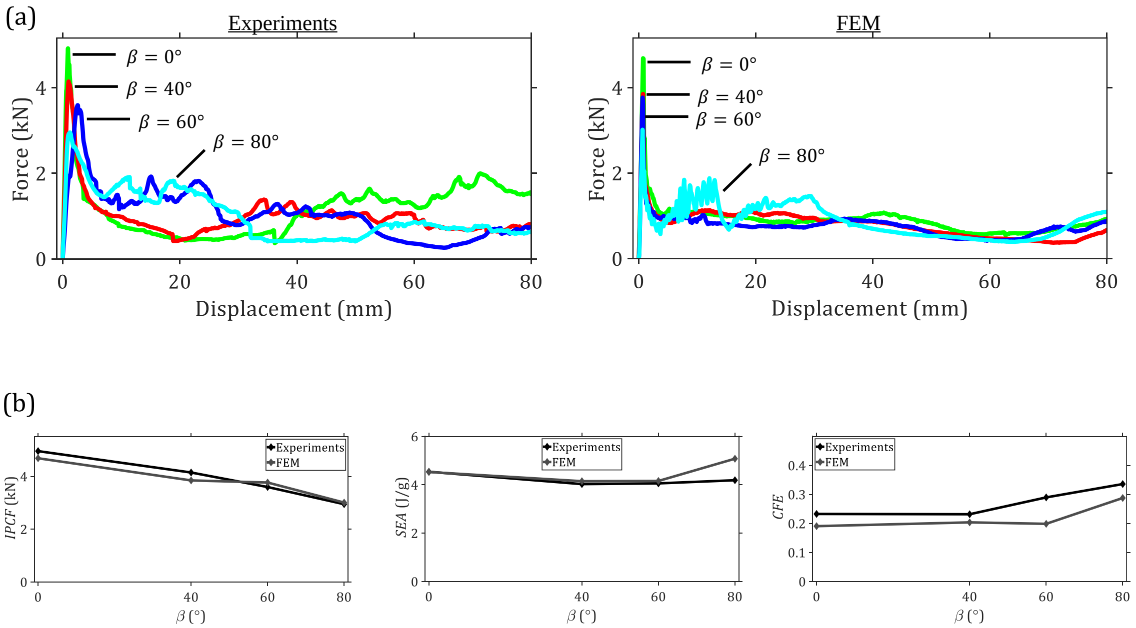

Figure 4.11: (a) Superimposed force-displacement plots for the Kresling cylinders tested. (b) The variation of each axial indicator with respect to the β values tested.

the cylinder. The experimental cylinder is about 30% heavier than the numerical cylinder while the energy absorption amounts are similar.

It is in the final axial indicator that we see the potential for an advantage for Kresling cylinders. Experimentally, the efficiency increases with more concavity after the $\beta = 40°$ Kresling cylinder. Numerically, the crushing force efficiency does not change much from $\beta = 0°$ to $60°$. There is a large discrepancy with the $\beta = 60°$ cylinder and this can be explained by the inability of the model to capture the elevated region at the beginning of its force-displacement curve. What is agreed upon is the $\beta = 80°$ cylinder achieving the most efficient collapse. It would appear that triggering a collapse due to a structural instability is not as stable as the material failure approach. It would appear that there is a critical concavity that transitions the cylinders from a less stable local instability to a more stable material failure. More experimental data needs to be collected to fully verify this claim but this result may provide insight for further research.

4.5 Conclusions

In this investigation, we explored the compressive behavior of filament wound CFRP Kresling cylinders which are derived from standard Kresling origami unit cells whose sides are increased to infinity. We observed the effects of concavity on the collapse of the cylinders and compared the energy absorption behavior of each concavity tested to that of a straight-walled cylinder. Both experiments and a finite element model were employed for this endeavour. The finite element model revealed that the cylinders are more imperfection sensitive with smaller concavities and so imperfections are required to properly model their collapse. In most of the tubes, the mechanism that triggers the collapse of the cylinders is that of local wall buckling, a structural instability. The current results suggest that larger concavities can change the initial collapse mechanism from structural instability to material failure. Ultimately, this provided a more stable collapse compared with the straight-walled cylinder that does not sacrifice the energy absorption per mass.

Although this initial finding shows potential for Kresling cylinders to act as efficient energy absorption devices, more work should be conducted to confirm this. Future work should include further development and maturing of the manufacturing process, perhaps with an actual filament winding machine. Therefore, imperfections such as non-uniform thickness, fiber misalignment, and excess resin and can be mitigated and the results more deterministic. Local wall buckling is heavily influenced by these imperfections and the current modelling scheme does have difficulty capturing experimental results. Additionally, parametric studies concerning geometric parameters, layup sequences, and material properties should be conducted with varying boundary conditions.

Chapter 5

DYNAMIC CRASH BEHAVIOR OF CFRP KRESLING ORIGAMI TUBES

From the results of Chapter 3, CFRP Kresling origami tubes have only been shown to absorb similar amounts of energy to straight-walled cylinders. However, the benefit from Kresling origami is the ability to provide a significantly more stable collapse, at least under quasi-static conditions. The crashworthiness of origami tubes is mostly studied quasi-statically, with some exceptions. Albert *et al.* looked at square tubes with origami designs milled into the walls and considered both the quasi-static and dynamic impact axial load cases on their geometries [87]. They found that the origami patterns were not enough to improve on the CFE and SEA on traditional square tubes. Additionally, the force response of the dynamic case appeared larger than the quasi-static case for all tubes tested. Zhou *et al.* conducted experimental dynamic crash tests on pre-folded square tubes with diamond-like creases with the goal to trigger their diamond collapse mode which is more stable and progressive [29]. It was found that the tubes were imperfection sensitive and did not always trigger this collapse mode. The collapse of crash boxes and composite structures have shown in other systems to have varying levels of dependency on load rate [88, 89]. Therefore, it is important to confirm that the cascading collapse of CFRP Kresling origami tubes is maintained under dynamic loading conditions that would be experienced under crash. Hagiwara studied crash conditions numerically with metal tubes and concluded that the Kresling origami tubes could be optimized to maintain elevated and stable force-displacement behavior that outperforms straight-walled tubes of similar size [49]. However, the model was not experimentally verified. This means the dynamic cascading collapse of Kresling origami tubes for crash applications has not been experimentally reported.

In this chapter's investigation, we will first propose a Kresling origami geometry that demonstrates superior crashworthiness to a straight-walled cylinder under quasi-static compression. Improved crashworthiness is defined in our case by exhibiting a significantly more stable collapse measured by the initial peak force, or the force at initial failure, and the crushing force efficiency, or the initial peak force divided by the average force of the collapse. The Kresling origami tube must also obtain similar amounts of energy absorption per mass. This is only confirmed quasi-statically due to the limitations of the load cell of the impact tester for this study as it is only rated for 15 kN and the straight-walled cylinder is capable of exceeding this limit. Finally, we confirm the cascading collapse of this tube under dynamic load conditions utilizing the aforementioned impact tester. A finite element model is also presented for predictions of the collapse behavior of the tube.

5.1 Kresling Origami Tubes and Geometric Parameters

In this section, we briefly introduce the geometry of the composite Kresling origami tubes utilized in this study.

A Kresling origami tube with four unit cells of uniform geometry is presented in Figure 5.1a. We select four unit cells for our study based on the results of our previous parametric study (Chapter 3) which suggested that at a minimum, four unit cells were necessary in a Kresling origami tube to outperform a straight-walled cylinder in terms of energy absorption per mass. The height of each unit cell is H_u and their circumscribed radius to R. The twist angle, β, of the unit cells dictates how much initial twist the unit cell has. In our study, to maintain an aspect ratio of one and to keep consistency with previous studies, we choose $H_u = R = 36$ mm. These tubes are longer than our previous parametric study as well to make them more consistent with the height of crash boxes in our previous investigation [70], which themselves are more consistent with the sizes of crash boxes in other studies. The tubes have nine sides as this was determined to have more energy absorption to cylinders [70].

As we will show, our tubes with unit cells that have the same geometry, or uniform unit cells, have difficulty either absorbing enough energy or collapsing without catastrophic collapse owed to sudden fracture along valley creases. Therefore, in this study, we propose a nonuniform unit cell design that utilizes a twist angle gradient so that β increases from top to bottom (Figure 5.1b). Table 5.1 provides the twist angle and height for each unit cell in this tube. These values will be justified later in the text. Additionally, we utilize filament winding to manufacture these tubes. Therefore, we require consistent convex regions to wrap around. We impose the following restriction to ensure that the angle valley creases, or creases that fold into the page, make with their horizontal, θ_v (see Figure 3.1b), are the same. Therefore, we use the following relationship to pick the height of the unit cell from a given β:

$$H_{u,i} = \sqrt{\left(\frac{b_{i-1}[sin(\beta_i + \frac{\pi}{n})]}{sin(\beta_{i-1} + \frac{\pi}{n}) + sin(\frac{\pi}{n})}\right)^2 - 4R^2 sin^2\left(\frac{\beta_i}{2} + \frac{\pi}{n}\right)} \tag{5.1}$$

i denotes the current unit cell whose height we are solving for. n is the number of sides of the unit cells. b_{i-1} is the length of the valley creases of the previous unit cell and can be calculated as:

$$b_{i-1} = \sqrt{H^2_{u,i-1} + 4R^2 sin^2\left(\frac{\beta_{i-1}}{2} + \frac{\pi}{n}\right)} \tag{5.2}$$

The Kresling origami tubes are compared with a straight-walled cylinder of similar height (144 mm) and radius (36 mm) that is wrapped with fibers that are +45° and −45° with respect to the axis of the tube. This cylinder serves as a benchmark that the Kresling tubes are compared against.

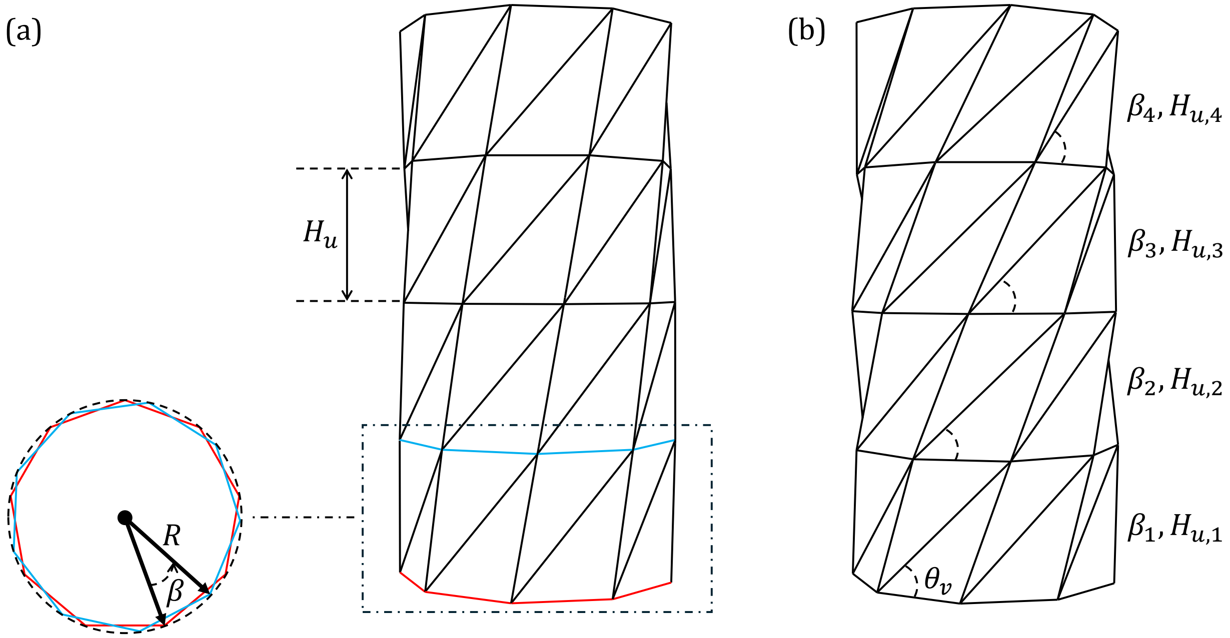

Figure 5.1: **Geometry of folded and unfolded Kresling tubes.** (a) A Kresling tube with N unit cells of height H_{unit}. (b) A cross-sectional cut of the tube showing its $n = 6$ sides, twist angle β, and circumscribed radius R. (c) Fold pattern of the Kresling tubes which depicts where mountain folds (fold outward) and valley folds (fold inward) are located. Bonding regions overlapped with facets on the other side of the fold pattern to generate a Kresling tube.

Table 5.1: Values of β and H_u in non-uniform tube

Twist Angles				Unit Cell Heights			
β_1(°)	β_2(°)	β_3(°)	β_4(°)	$H_{u,1}$ (mm)	$H_{u,2}$ (mm)	$H_{u,3}$ (mm)	$H_{u,4}$ (mm)
30	26.67	23.33	20	39.0	38.0	36.7	35.4

The fold patterns needed to generate the Kresling origami tubes are provided in Appendix

C. Also provided in Appendix C is a brief overview of the manufacturing process for our tubes.

5.2 Procedures for Investigation

In this section, we first provide a description of the performance indicators we utilized to assess the crashworthiness of the tubes in this study (Section 5.2.1). We then outline the experimental setups utilized to study the collapse behavior (both quasi-static and dynamic) of the tubes (Section 5.2.2). Finally, we describe the finite element model we developed to predict the collapse behavior of the tubes (section 5.2.3).

5.2.1 Performance Indicators

We evaluate the crashworthiness of the tubes with three parameters: The initial peak crushing force, $IPCF$, the crushing force efficiency, CFE, and the specific energy absorption, SEA. Each one can be extracted from the force-displacement curve of a tube. The $IPCF$ is the peak force at initial failure in the curve. It measures the load-carrying capacity of a tube and it provides an indirect measure of stiffness. We require this parameter to be reduced to minimize the average compressive force acting through an impact [68]. Additionally, it must be compared to the mean compressive force, F_{mean} via the $CFE = \frac{F_{mean}}{IPCF}$. The CFE is a measure of the load variations of the force-displacement curve. The smaller CFE is, the more variations there are in the curve and the less efficient the tube is at absorbing energy. We strive to increase the CFE as close to unity as possible to reduce load variations and generate a more stable and progressive collapse. However, we must not sacrifice energy absorption to reach this end. Energy absorption measures how well a structure dissipates crushing energy and found by calculating the area under the force-displacement curve. This value is affected significantly by material properties and geometry and so a direct comparison of the energy absorption between different structural designs with his parameter is difficult. Instead, we utilize the SEA which is the energy absorption divided by the mass of the tube. A tube should be designed to make this parameter as large as possible.

5.2.2 Experimental Setup

In order to compare the crashworthiness behavior of the Kresling origami tubes with straight-walled cylinders, we utilize quasi-static axial compression tests. The apparatus for our quasi-static experiments is seen in Figure 5.2a. The load frame in the apparatus is an Instron 5585H electro-mechanical load frame which measures force with a 50 kN load cell. The compression load rate is 20 mm/min and is displacement-controlled with a closed loop control system. The CFRP composite tubes have large stiffness and low mass so we can assume this load rate provides a quasi-static collapse. The bottom platen supporting the tube is fixed while the top platen which provides the compression is only allowed to translate vertically.

Dynamic compression tests are conducted with an Instron Dynatup 9250HV impact tester as shown in the left image of Figure 5.2b. The purpose of these tests are to demonstrate that the Kresling origami tubes can also provide a stable and cascading unit cell collapse under larger load rate conditions and to determine how the collapse may differ from quasi-static conditions. The drop mass of the impact tester, with the drop plate installed (see right image of Figure 5.2b) is about 8.5 kg and we set the potential energy of the drop mass to 250 J which we determined was necessary to collapse most of the tube. The initial velocity at impact is around 7.80 m/s. Only three unit cells are fully collapsed in these experiments. The load cell has a maximum rating of 15 kN and triggering a compression larger than this may damage the load cell. Therefore, safety poles are put in place to prevent the drop mass from falling far enough to trigger densification in the tube. Due to a lack of the necessary precision, we can only lower them enough for three unit cells to be fully collapsed. Additionally, this 15 kN max load prevents us from testing straight-walled cylinders in this apparatus since the thickness we are tested at triggers failure loads in these tubes very close to 15 kN even in lower energies than 250 J. As with the quasi-static apparatus, the bottom platen is not able to move and the top platen provides the compression. Their respective surface finishes are different from their quasi-static counterparts. It should also be noted that the top platen material is plastic, not metal and generates more friction along the tube and is capable of being scratched. The collapse is captured initially with a camera with a capture rate of 960 fps. We eventually switched to a Kirana high-speed camera that captured video at 5,000 fps and is triggered by a signal sent from the drop tower right before impact. Although the force applied to the top platen is measured with a load cell, the displacement is not measured directly. The software for the impact tester utilizes the initial velocity at impact and the force data to back calculate the displacement and this is the measurement we will report. Finally, the collection of data is triggered by a flag that is placed just above the top of the load cell during the point of the drop when the impact plate is about to make contact with the tube.

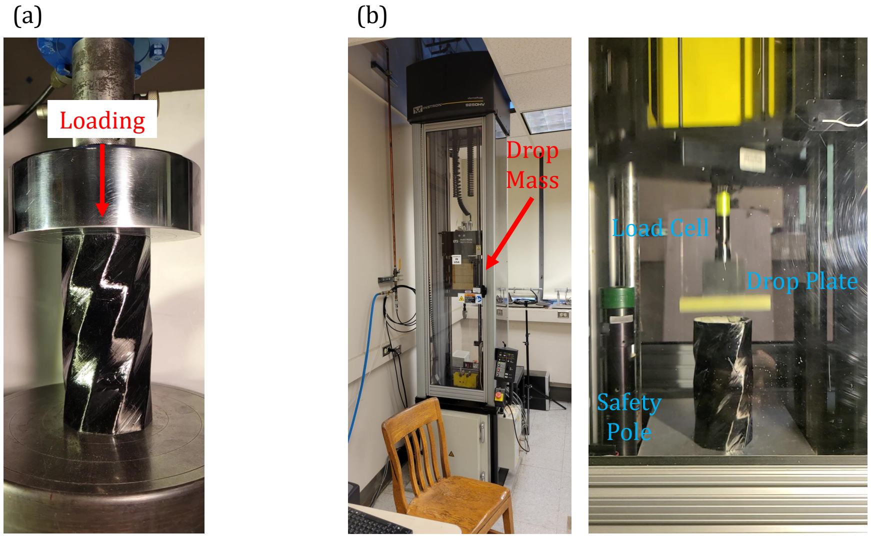

Figure 5.2: **The experimental apparatuses of this investigation.** (a) The setup for quasi-static tests. (b) The setup for dynamic crash tests.

5.2.3 *Numerical Simulation*

We utilized a finite element model that was developed in our previous research (Chapter 3) with the commercial software ABAQUS/EXPLICIT to predict the quasi-static behavior of the Kresling origami tubes. It is slightly modified for prediction of the dynamic collapse behavior of the tubes. We will provide a brief description of the finite element model.

The setup for the model is given in Figure 5.3. As with experiments, the Kresling origami tube rests on a fixed bottom platen and is compressed by a top platen that is restricted in all degrees of freedom except for vertical translation. In the quasi-static simulations, the friction coefficient $\mu_{f,top}$, which is the friction coefficient between the top cross-section of the tube and top platen, is set to 0.2. The bottom friction coefficient, $\mu_{f,bottom}$, or the friction coefficient between the bottom cross-section of the tube and bottom platen, is 0.3. The general contact coefficient is 0.15 which prevents numerical instabilities during compression. The dynamic simulations only have a general contact coefficient of 0.3 due to different boundary conditions in the drop tower. In quasi-static simulations, it was determined that a load rate of 65 mm/s was sufficient to maintain kinetic energy at less than 5% of the internal energy. Dynamic simulations apply a predefined velocity that is the same as experiments of 7.8 m/s. A mass scaling factor of 10 is applied to the quasi-static simulations.

In both cases, the tubes are meshed with four-node reduced integration shell elements (S4R) since their thickness is sufficiently smaller than their other geometric dimensions. Additionally, these elements can efficiently capture the overall collapse behavior while being less computationally expensive than solid elements. In quasi-static simulations, element deletion is not enabled as fracture is not significant in the nonuniform tubes in quasi-static compression. Element deletion is re-enabled in dynamic simulations. Additionally, tubes have a global mesh size of 3 mm in the quasi-static case as this is the minimum size that can be utilized to capture the full compression without resulting in unrealistically long stable time increments. A mesh convergence study shows that 2 mm is sufficient for dynamic simulations. The platens are meshed with four-node rigid R3D4 elements of global mesh size 4.6 mm.

The section definition of the tubes assumes perfect cohesion between all materials utilized. The materials from the innermost to outermost regions of the walls include PET, composite layer, and excess resin. The PET is given a thickness of 0.254 mm while the excess resin is given 0.2 mm. The composite layer is given a thickness of 0.5 mm in the bottom unit cell and is reduced linearly in each unit cell until 5% overall at the top unit cell that assists in producing a cascading collapse in quasi-static sims. The measured thickness of the fabricated tubes is about 1.42±0.11 mm. The reduced thickness from experiments is an indirect way to account for the randomized thickness of the tubes.

The mechanical properties for each material are taken from our previous investigation [70] and summarized in Tables 5.2 and 5.3. As with that investigation, composite damage initiation is governed by the Hashin failure criteria. It is assumed the resin is elastic-perfectly plastic and the stress-strain curve of PET is utilized in the simulation. The resin and PET have damage initiation by the built-in ductile damage scheme. In all materials, we apply a energy-based linear damage evolution scheme to capture the damage in the materials.

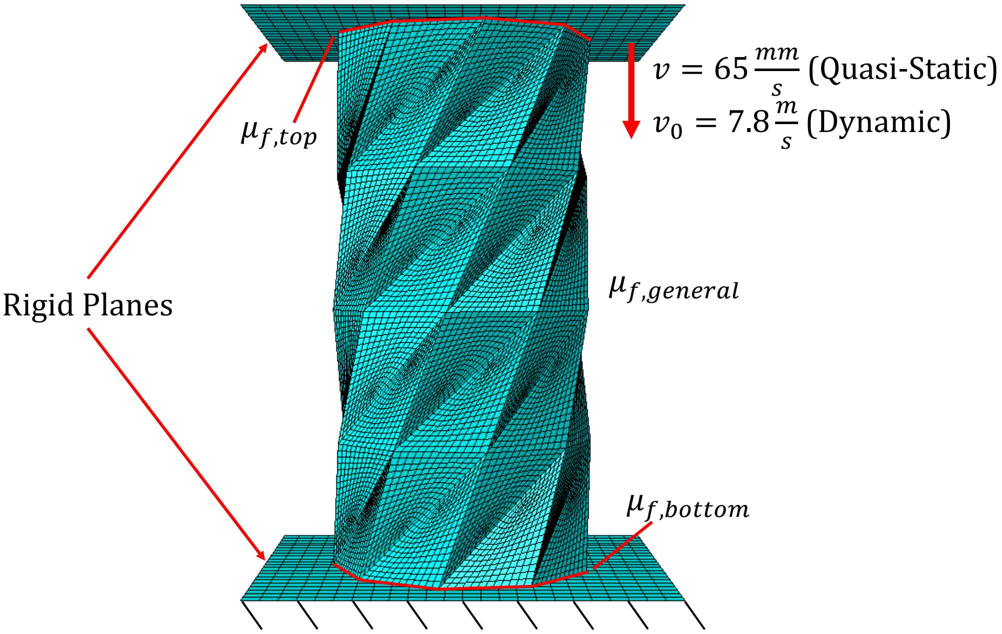

Figure 5.3: **The finite element model utilized for this study.** The assembly is the same for both the quasi-static and dynamic simulations. Only the friction parameters, boundary conditions of the top plate, and whether element deletion is enabled change between the two cases.

Table 5.2: Elastic properties and thickness of each material

<table>
<tr><td colspan="8">Composite</td></tr>
<tr><td colspan="2">Tensile Moduli</td><td colspan="2">Shear Moduli</td><td colspan="2">Poisson's Ratios</td><td>Ply Thickness</td><td>Density, ρ_c</td></tr>
<tr><td>E_1 (GPa)</td><td>$E_2 = E_3$ (GPa)</td><td>$G_{12} = G_{13}$ (GPa)</td><td>G_{23} (GPa)</td><td>$\nu_{12} = \nu_{13}$</td><td>ν_{23}</td><td>(mm)</td><td>(kg/m^3)</td></tr>
<tr><td>74.4</td><td>6.33</td><td>1.97</td><td>2.09</td><td>0.264</td><td>0.510</td><td>0.5</td><td>1220</td></tr>
<tr><td colspan="8">PET</td></tr>
<tr><td colspan="4">Tensile Moduli</td><td colspan="2">Poisson's Ratio</td><td>Ply Thickness</td><td>Density, ρ_c</td></tr>
<tr><td colspan="4">E (GPa)</td><td colspan="2">ν</td><td>(mm)</td><td>(kg/m^3)</td></tr>
<tr><td colspan="4">2.25</td><td colspan="2">0.33</td><td>0.254</td><td>1900</td></tr>
<tr><td colspan="8">Resin</td></tr>
<tr><td colspan="4">Tensile Moduli</td><td colspan="2">Poisson's Ratio</td><td>Ply Thickness</td><td>Density, ρ_c</td></tr>
<tr><td colspan="4">E (GPa)</td><td colspan="2">ν</td><td>(mm)</td><td>(kg/m^3)</td></tr>
<tr><td colspan="4">2.90</td><td colspan="2">0.33</td><td>0.2</td><td>1110</td></tr>
</table>

Table 5.3: Failure Properties of each material

Description	Variable	Value
CFRP Longitudinal Tensile Strength (MPa)	X_{1t}	1500
CFRP Longitudinal Compressive Strength (MPa)	X_{1c}	1200
CFRP Transverse Tensile Strength (MPa)	X_{2t}	50
CFRP Transverse Compressive Strength (MPa)	X_{2c}	200
CFRP In-Plane Shear Strength (MPa)	S	70
CFRP Longitudinal Tensile Fracture Energy (N/mm)	G_{1t}^c	90
CFRP Longitudinal Compressive Fracture Energy (N/mm)	G_{1c}^c	60
CFRP Transverse Tensile Fracture Energy (N/mm)	G_{2t}^c	1
CFRP Transverse Compressive Fracture Energy (N/mm)	G_{2c}^c	1.71
PET Yield Strength (MPa)	σ_y	28.85
PET Plastic Fracture Strain (mm/mm)	$\varepsilon_{fracture,PET}$	0.0872
PET Fracture Energy (MPa)	$G_{f,PET}$	3.18
Resin Yield Strength (MPa)	σ_y	68
Resin Fracture Energy (MPa)	$G_{fracture,R}$	1
Resin Density (kg/m^3)	ρ_R	1110

5.3 Results and Discussion

We begin this section by describing the crushing behavior of the straight-walled cross-ply cylinder acting as our control in this study (Section 5.3.1). This will be followed by a description of the quasi-static behavior of our Kresling origami tubes (Section 5.3.2). Finally, we will demonstrate that the cascading collapse of the Kresling origami tubes can be captured dynamically (Section 5.3.3).

5.3.1 Crushing behavior of the cylinder

The cylinder in this study acts as a control to compare our Kresling origami tubes against. The cross-ply layup prevents any twisting in the tube as well as isolated fracture parallel to fibers that propagates suddenly along the length of the tube. The quasi-static collapse of the cylinder is depicted in Figure 5.4 along with the force-displacement behavior. The cylinder initially undergoes local wall buckling that results in the sides of the cylinder compressing inward near the top. This structural instability significantly reduces the load-carrying capacity of the cylinder and the force drops considerably. Around 60 mm of compression, the force increases a relatively small amount as the bottom portion of the cylinder slides into a stiffer configuration. This leads to additional local wall buckling which brings down the force response until densification. Structural instabilities such as local wall buckling can reduce the stability of a collapse which explains the relatively small CFE of the cylinder of 0.201. However, its SEA is relatively large when compared to previous tubes we have tested ([70] and Chapter 3).

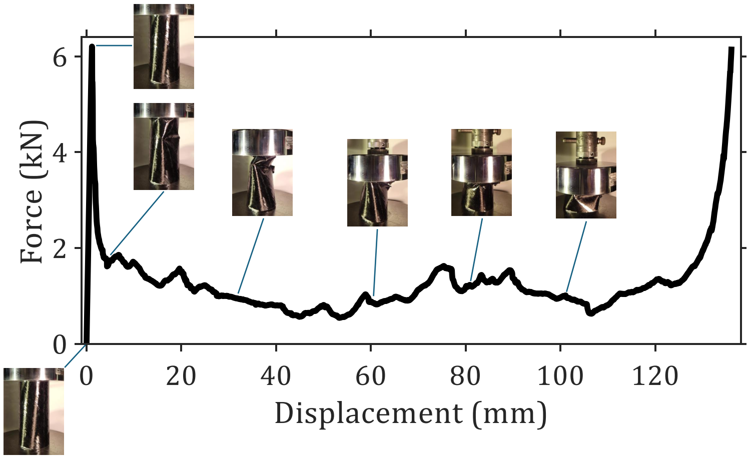

Figure 5.4: **Experimental quasi-static collapse of the cylinder.** Depicted is the force-displacement curve of the tested cylinder as well as its collapse modes.

5.3.2 Quasi-static behavior of Kresling origami tubes

We first quasi-statically test Kresling origami tubes with unit cells that all have the same geometry. The results are shown in Figure 5.5. The goal is to trigger a progressive cascading collapse that has been observed in our previous tubes ([70] and Chapter 3) while achieving superior SEA and CFE values compared to the cylinder. The cascading unit cell collapse can be characterized by the full collapse of one unit cell before the next one collapses. Typically, the first unit cell to collapse will be at the boundaries as its outer vertices are kinematically constrained by friction. At these vertices, the epoxy resin will fail first in both tension and compression. As the unit cell is compressed, the matrix will continue to fail along the valley creases and the composite layer itself will eventually fail due to facet bending. After failure, as the unit cell collapses, the force response of the tube drops as the unit cell's stiffness decreases. Eventually, the unit cell will densify and press on the tube resulting in the presence of another peak. When a sufficient force is achieved to initiate failure, another unit cell will collapse. This continues until full densification. The peak-to-peak behavior provides a more stable collapse compared with the tested cylinder.

It was determined from our previous research (Chapter 3) that a smaller twist angle results in more energy absorption for Kresling origami tubes. However, the number of sides of the tube must be properly balanced with the number of unit cells to prevent the tube from becoming stiffer than the cylinder. We started our study with a Kresling origami tube with nine sides and four unit cells to achieve as much energy absorption as possible. The tube would have a twist angle of 10° and if needed, we would decrease the twist angle. Figure 5.5a shows that this tube succeeded in producing a smaller $IPCF$ compared with the cylinder. Despite this, the tube experienced catastrophic failure in the form of sudden fracture along a continuous line of valley creases. Most likely this represented a region of the tube with the least amount of stiffness. The tube eventually opened up and could not proceed to full compression. A similar result occurred with the Kresling origami tube with $\beta = 20°$ (see Figure 5.5b). The tube was less stiff in comparison as indicated but the smaller initial peak. The final tube tested with $\beta = 30°$ did achieve a full collapse and by the peak-to-peak behavior was progressive (see Figure 5.5c). However, the final two unit cells appear to have failed in a non-cascading manner. Despite this, there is the presence of two peaks suggesting that portions of both tubes had not completely failed before densification.

Figure 5.5d compares the force-displacement performance of each Kresling origami tube as well as the cylinder. We notice the elevated response of the tube with $\beta = 30°$ compared to the cylinder after their initial peaks. This Kresling tube achieves most of the desired behaviors: smaller $IPCF$ and larger CFE compared to the cylinder as shown in Table 5.4. However, it does not achieve the same amount of energy absorption per mass. In the table, we provide a cutoff compression for measuring the CFE and SEA values. For curves with densification regions, we cut this parameter off when the densification force is the same value as the largest peak force which the Kresling origami tube achieves sooner in its compression. Additionally, the thickness of the cylinder is similar to the Kresling origami tubes but its surface area is smaller which results in a smaller mass (see Table 5.4). So although the Kresling origami tube can achieve more energy absorption, it is still less efficient on a per mass basis compared with the cylinder. The mass only grows with more twist angle due to the increased surface area of the facets. With the limited ability to improve our manufacturing to reduce the effects of imperfections, and with limited material choice, we do not see a way to outperform the straight-walled cylinder in terms of crashworthiness with the current Kresling origami design.

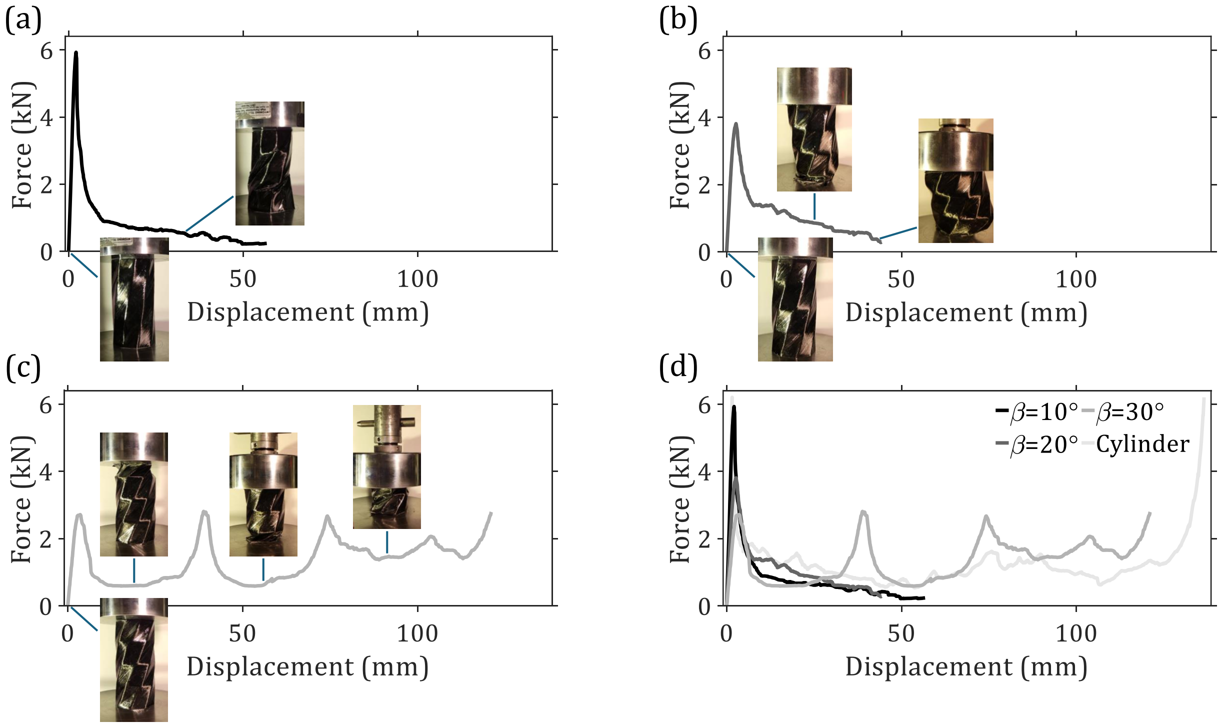

Figure 5.5: **Collapse results of uniform Kresling origami tubes.** Results for a tube with β of (a) 10°, (b) 20°, and (c) 30°. (d) All of the tube force-displacement results with the cylinder force-displacement.

It is here that we propose a modification to the Kresling origami tube design. Smaller twist angles will provide more energy absorption but we also need ones smaller than 30° for reduced mass. However, we must recognize that smaller twist angles can result in sudden catastrophic fracture. Therefore, rather than utilizing unit cells that all possess the same twist, we utilize unit cells with varying twist angles. The twist angles are graded so that they decrease from top to bottom as described in Section 2. The goal is to maintain a reduced

$IPCF$ with the larger twist angles at the top of the tube while enforcing cascading collapse due to the increasing stiffness of the unit cells that follow. Additionally, the energy absorption capability should increase due to smaller twist angles. We first simulate this geometry with the results presented in Figure 5.6. The tube achieves a cascading collapse and has peak to peak behavior. The last two unit cells do not have well defined peaks as portions of their walls fail at the same time (position 4). The resulting plateau like region still provides a stable collapse. The Kresling force response is also larger than the cylinder's. This translates into superior SEA as shown in Table 5.4 while maintaining a larger CFE. The $IPCF$ is larger than the uniform tube with $\beta = 30°$. However, manufacturing imperfections can bring down the $IPCF$ by about 30% in a manufactured tube. It should be noted that the densification region is not simulated. This is due to an element achieving a stable time step too small to realistically finish the full collapse. It is expected that manufacturing imperfections will bring down the energy absorption of the Kresling origami tube. Therefore, we experimentally test to ensure the tube will still exhibit superior qualities to the cylinder.

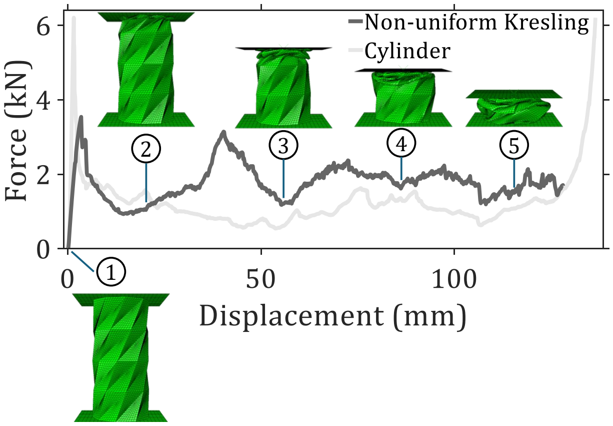

Figure 5.6: **Numerical quasi-static behavior of non-uniform Kresling origami tubes.** The simulated non-uniform Kresling origami force-displacement is superimposed with the tested cylinder's force-displacement. The collapse modes of the Kresling origami tube are also provided.

The results of the quasi-static test on the non-uniform design are shown in Figure 5.7. The collapse modes are similar to their numerical counterparts. As in the numerical collapse, the experimental collapse showed that the last two unit cells have components that fail around the same displacement. Despite this, the model overestimates the initial peak and valleys of the manufactured tube. Additionally, there is a well-defined third and fourth peak experimentally. This means the damage in the final unit cell was not as severe as the third unit cell to collapse. These discrepancies can be explained by manufacturing imperfections. Ultimately, the overall energy absorption per mass was reduced by 20%, giving the tube almost the exact same SEA as the cylinder. Despite this, the CFE is larger than predicted and shows a far more stable collapse with the same amount of SEA. Therefore, we have shown that this design exhibits superior crashworthiness.

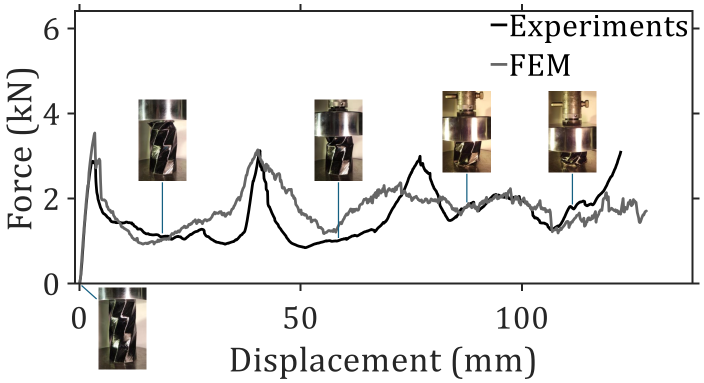

Figure 5.7: **Experimental verification of non-uniform tube quasi-static behavior.** Experimental and numerical force-displacement curves with experimental collapse modes.

5.3.3 *Dynamic collapse of Kresling origami tubes*

Our previous research only considered quasi-static load rates to determine the ideal collapse of the Kresling origami tubes. Therefore, we seek to confirm that the cascading collapse

Table 5.4: Summary of performance indicators

Quasi-Static					
Tube	Mass (g)	$IPCF$ (kN)	Max Displacement (mm)	SEA (J/g)	CFE
Cylinder	40.0	6.21	136.5	4.26	0.201
Uniform ($\beta = 30^\circ$)	49.7	2.72	121.1	3.25	0.487
Non-uniform (FEM)	44.5	3.54	128.1	5.11	0.501
Non-uniform (FEM)	44.5	3.54	110.8	4.45	0.505
Non-uniform (Exp)	46.1	2.88	122.4	4.21	0.551
Non-uniform (Exp)	46.1	2.88	110.8	3.67	0.531
Dynamic					
Tube	Mass (g)	$IPCF$ (kN)	Max Displacement (mm)	SEA (J/g)	CFE
FEM (before densification)	44.5	4.05	110.8	4.69	0.466
Exp (Trial 1)	47.7	4.48	110.8	3.90	0.373
Exp (Trial 2)	46.9	4.83	110.8	3.90	0.278
Exp (Trial 3)	46.7	4.72	110.8	3.90	0.274
Exp (Trial 4)	46.7	4.34	110.8	3.90	0.208
Exp (Trial 5)	46.3	4.45	110.8	3.35	0.312
Exp (Average)	46.9±0.5	4.57±0.21	110.8	3.14±0.65	0.289±0.061

behavior of the Kresling origami tubes is maintained under larger dynamic load rates. Otherwise, it is not a suitable option for crash crash box designs. We simulated the crash conditions described earlier (Section 3.2) for the non-uniform tube and compared it with the quasi-static case (Figure 5.8). A cascading collapse is observed and it appears in the dynamic loading case, components of the final two unit cells do not fail simultaneously, resulting in a well-defined third peak. The force-displacement curves of both cases exhibit similar behavior up to about 60 mm of compression. This suggests that the progressive collapse behavior is maintained. The performance indicators of the simulated dynamic case is given in Table 5.4 and it appears that up to the same compression as the quasi-static case, it has a larger specific energy absorption due to the cascading collapse in the final two unit cells. Its collapse is slightly less stable due to the larger initial peak which is caused by different boundary conditions and the larger load rate.

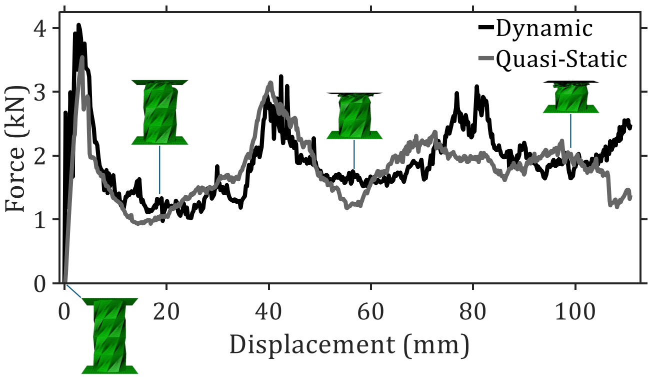

Figure 5.8: **Numerical dynamic behavior of non-uniform Kresling origami tubes.** The simulated dynamic force-displacement is compared with the numerical quasi-static curve. The dynamic collapse modes are also depicted.

We experimentally tested a non-uniform tube and compared the results with the simulation as shown in Figure 5.9. The experimental collapse is captured at a rate of 960 fps. The experimental tube exhibits the cascading collapse and shows good qualitative agreement with the numerical simulation. The experimental force response is not as elevated, possibly due to the presence of manufacturing imperfections and slightly different boundary conditions. Table 5.4 reveals that the FEM response is more stable based on its larger CFE and absorbs more energy per mass. The cascading collapse is still confirmed to be present in the dynamic case. Given the large strain rate behavior of the test, we decided to conduct four more trials to determine the repeatability of the result.

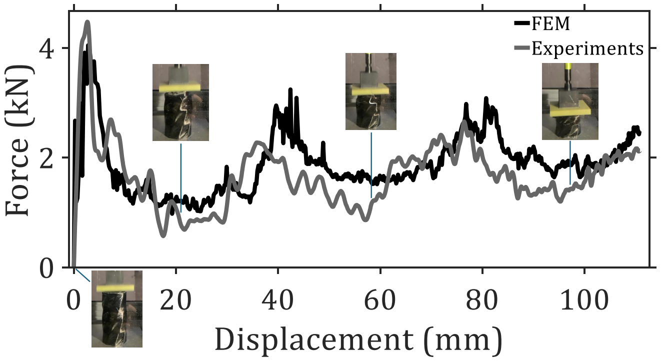

Figure 5.9: **Numerical dynamic behavior of non-uniform Kresling origami tubes.** The simulated dynamic force-displacement is compared with the numerical quasi-static curve. The dynamic collapse modes are also depicted.

From Figure 5.10a-b, it is evident that the cascading effect from unit cell to unit cell is not always repeatable. To see if we could better capture the collapse modes, we switched to using a camera with a capture rate of 5,000 fps. For the tube in Figure 5.10a, there is significant fracture that damages the unit cell below the top one which results in a larger drop in force that is not significantly picked up at 40 mm of compression. Eventually, the third unit cell from the top recovers some of the stiffness. The tube in Figure 5.10b leans a bit after the first unit cell collapse which reduces the second unit cell's force response. However, the cascading collapse is recovered by the third unit cell. Therefore, the collapse is observed in Figure 5.9 is not reliably captured each time. The manufacturing may need to be improved for more consistency.

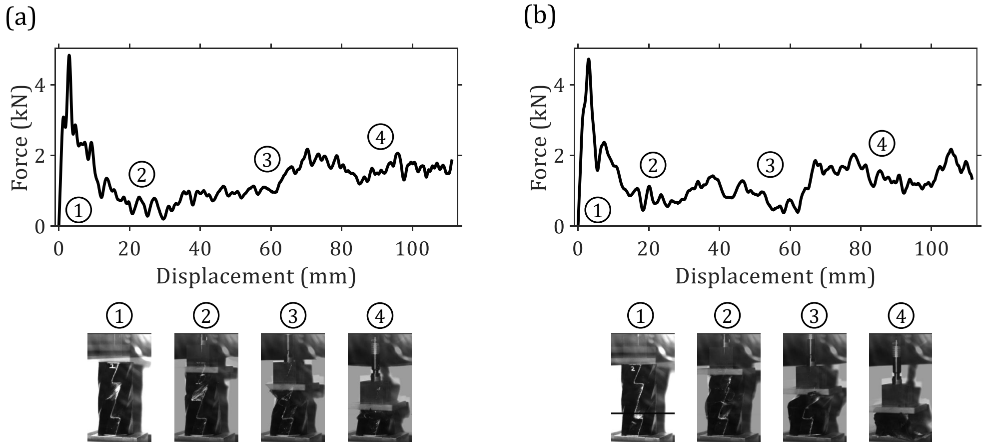

Figure 5.10: **Less progressive dynamic collapse in Kresling origami tubes.** These tubes are examples of potential collapse which is not as progressive as expected but some cascading behavior is witnessed.

We provide the force-displacement and force-time curves for each tested tube in the left hand side of Figures 5.11a-b. The averaged data with standard deviation for these tubes is provided in the right hand side of Figure 5.11a-b. In both force-displacement and force-time, we see relatively small deviation in the first peak and larger deviations in the rest of the curves. This is reasonable as the damage propagation will be affected by imperfections and exact boundary conditions. The presence of individual peak regions does suggest that the cascading effect overall, is triggered under dynamic loading conditions. Although the numerical curve appears to be captured within the standard deviation envelope from the initial peak to about 70 mm of compression in the force-displacement, the rest of it is overestimated. This may suggest a strain-rate effect on the materials or significant effects from imperfections. The apparatus itself may need to be improved. The experimental force-time curve exhibits oscillations in the first peak. The oscillations occur at a period of approximately 0.7 ms. This is the result of a rarefaction wave travelling through the load cell which may affect our experimental results. The drop plate is attached to the load cell with screws that tighten up against the load cell. So there may be some vibration between the two components. Additionally, Table 5.4 provides the performance indicators of each tested tube as well as the average of these indicators. We see that the mass does not vary much and neither does the $IPCF$. There is considerable variation in the SEA and CFE. Overall, we demonstrate that cascading collapse can be maintained in Kresling origami tubes under dynamic conditions.

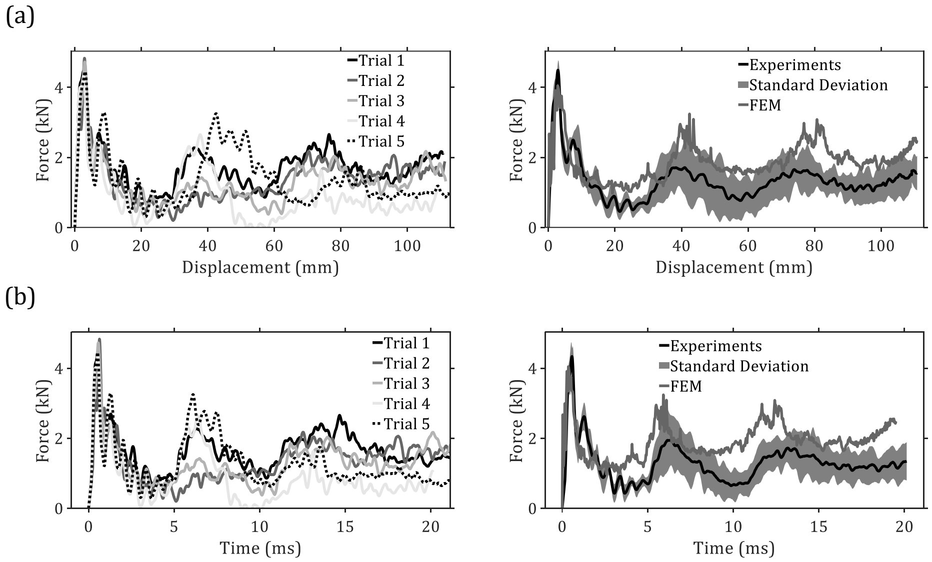

Figure 5.11: **Averaged dynamic force results.** (a) The force-displacement data for the Kresling origami tubes (left) and their average result superimposed with the numerical result (right). (b) The force-time data for the Kresling origami tubes (left) and their average result superimposed with the numerical result (right).

Finally, Figure 5.12 shows the experimental quasi-static and dynamic curves together. They qualitatively match up well with the exception of the fourth peak corresponding to the pre-mature damage of the bottom unit cell in the quasi-static case. The peaks in the quasi-static case are a larger than the dynamic case but are nearly captured by the variation envelope. Evidently, Table 5.4 shows that the quasi-static SEA falls within the variation of the dynamic case which means the dynamic case is capable of maintaining similar amounts of energy absorption per mass. The collapse is less stable than the quasi-static case when considering that the dynamic CFE is smaller than the quasi-static CFE even if the larger end of the range is used. Part of this is owed to the larger $IPCF$ of the dynamic case. In summary, we showed the cascading collapse is maintained under crash conditions but the crashworthiness is diminished as the load rate is increased.

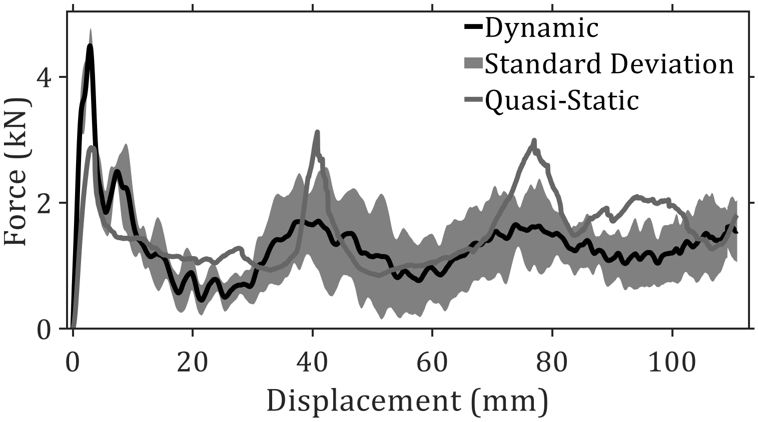

Figure 5.12: **Comparison of experimental quasi-static and dynamic results.** The experimental force-displacement results from the quasi-static and dynamic cases are provided.

5.4 Conclusions

In this investigation, we proposed a non-uniform CFRP Kresling origami design that reduced the twist angle of each unit cell linearly from top to bottom while maintaining the same angle the valley creases make with respect to the horizontal in each unit cell. We showed that the design can prevent sudden fracture along valley creases and provide superior crashworthiness compared with a cross-ply straight-walled cylinder with the same height and radius. The tube can absorb the same amount of energy per mass while providing a significantly more stable collapse. Additionally, we confirmed that the progressive cascading collapse inherent to Kresling origami tubes is present in both the quasi-static and dynamic crash cases. Finite element simulations were utilized to predict the collapse behaviors and experiments with a load frame and impact tester verified the results.

The collapse behavior of the Kresling origami tubes was determined to be affected by the load rate. The average dynamic collapse behavior showed similar levels of energy absorption per mass but their collapse was less stable compared to the quasi-static case, as could be seen with its reduced crushing force efficiency. It has been thoroughly demonstrated that Kresling origami tubes can be efficient replacements for straight-walled cylinders. However, more rigorous research must be conducted to determine the effects of imperfections on the collapse of the CFRP Kresling origami tubes.

Chapter 6

SUMMARY AND FUTURE WORK

6.1 Summary

We have demonstrated the superior crashworthiness of CFRP Kresling origami tubes compared to conventional straight-walled crash boxes. Finite element modelling and experimental testing were utilized to verify this result. We first developed a novel filament winding approach for efficiently fabricating these Kresling origami tubes that can eventually be automated for industrial applications. From preliminary findings of its corresponding investigation, we observed the following of the quasi-static axial collapse behavior of our CFRP Kresling origami tubes:

- They exhibit a cascading cell-by-cell progressive collapse.
- They possess a smoother and more efficient collapse than traditional straight-walled tubes.
- Their geometry must be tailored for superior energy absorption per mass.

In order to determine the important geometric parameters needed for superior energy absorption to straight-walled cylinders without sacrificing efficiency, we conducted a parametric study on our Kresling origami tubes. The resulting findings are as follows:

- The twist angle has the largest impact on the energy absorption and stiffness of the tubes.
- The unit cell height only contributes significantly to the stiffness of the tube.

- Increasing the number of sides of the cross-section increases the energy absorption but it can over-stiffen the tube compared with straight-walled cylinders.
- Increasing the number of unit cells increases efficiency and energy absorption by providing a smoother cascading collapse but shows diminishing results after about four unit cells in the tubes tested.

As an extension of the investigation into how the number of sides affects the crashworthiness, we derived a concave cylinder (Kresling cylinder) when we let the number of sides approach infinity. We investigated their compressive behavior and we summarize our results as follows:

- At smaller concavities, the Kresling cylinders were imperfection sensitive and failed due to local-wall buckling.
- At larger concavities, the failure is due to stress in the material.
- All Kresling cylinders collapse more efficiently than a straight-walled cylinder. The collapse is smoother with more concavity.

Finally, we proposed a non-uniform unit cell design with a fiber layer that is not parallel to the valleys. It was found to have a significantly more progressive collapse than a straight-walled cylinder which provided the same amount of energy absorption per mass. We then confirmed its progressive cascading collapse under dynamic impact tests. Although the crashworthiness is slightly diminished, the overall collapse behavior is present.

6.2 Future Work

This research demonstrated the superior crashworthiness of CFRP Kresling origami tubes compared to straight-walled composite cylinders and that their progressive cascading collapse can be maintained under dynamic conditions. However, there are still some areas of the research that can be improved on to gather a deeper understanding of the collapse of the tubes and potentially improve their crashworthiness further.

The first is to mature the manufacturing. Winding the tubes by hand inherently introduces geometrical imperfections such as significant thickness variations in the walls, distorted unit cell geometries from folding, and fiber misalignments. These are added to the imperfections from prepping the tubes for testing that include excess resin from discrete rotations during curing and uneven top and bottom cross-sections from removing the ends of the tubes with the wet tile saw. There could also be a non-uniform distribution of material properties throughout the tube due to the imprecision of the manufacturing technique utilized. We have shown with our finite element model that the tubes are imperfection sensitive to a degree and so minimizing these imperfections will be beneficial for better predictions and more consistent collapse behavior. A filament winding machine and a 3D printer that can generate the mandrels would significantly help in reducing these imperfections.

On the topic of imperfections, even if the manufacturing process is improved, imperfections will always be present. More studies should be conducted on the imperfection sensitivity of the Kresling origami tubes and should rigorously explore how each imperfection contributes to the crashworthiness. If any imperfections are significant, it may be necessary to include them in any numerical models for predicting the collapse behavior.

The effect of thickness on the collapse behavior of the tubes (origami and cylinders) was not considered in our parametric study due to manufacturing limitations. If these limitations could be circumvented, this study should be conducted. Additionally, a more complete geometric parameter study for the Kresling cylinders should be conducted to further understand how the initial failure can be made more stable with more energy absorption. It would also be interesting to observe if they also achieve superior energy absorption when unit cells are stacked. Finally, other fiber materials (glass, aramid, etc.), matrix materials (thermoplastic, SMA, polyester, etc.), and different combinations of these materials could be explored to determine which are more suitable for this application.

BIBLIOGRAPHY

[1] N. A.Z. Abdullah, M. S.M. Sani, M. S. Salwani, and N. A. Husain. A review on crashworthiness studies of crash box structure. *Thin-Walled Structures*, 153:106795, 2020.

[2] Shubham Bhutada and M. D. Goel. Crashworthiness parameters and their improvement using tubes as an energy absorbing structure: an overview. *International Journal of Crashworthiness*, 27:1569–1600, 2022.

[3] J.M. Alexander. An approximate analysis of the collapse of thin cylindrical shells under axial loading. *The Quarterly Journal of Mechanics and Applied Mathematics*, 13(1):10–15, 1960.

[4] W. Abramowicz. The effective crushing distance in axially compressed thin-walled metal columns. *International Journal of Impact Engineering*, 3(3):309–317, 1983.

[5] W. Abramowicz and N. Jones. Dynamic axial crushing of square tubes. *International Journal of Impact Engineering*, 2(2):179–208, 1984.

[6] Mehmet A. Guler, Muhammed E. Cerit, Bertan Bayram, Bora Gerçeker, and Emrah Karakaya. The effect of geometrical parameters on the energy absorption characteristics of thin-walled structures under axial impact loading. *International Journal of Crashworthiness*, 15(4):377–390, 2010.

[7] A. G. Mamalis, W. Johnson, and G. L. Viegelahn. The crumpling of steel thin-walled tubes and frusta under axial compression at elevated strain-rates: Some experimental results. *International Journal of Mechanical Sciences*, 26(11-12):537–547, 1984.

[8] S. R. Reid and T. Y. Reddy. Static and dynamic crushing of tapered sheet metal tubes of rectangular cross-section. *International Journal of Mechanical Sciences*, 28(9):623–637, 1986.

[9] Athanasios G Mamalis, DE Manolakos, GA Demosthenous, and MB Ioannidis. *Crashworthiness of composite thin-walled structures.* CRC Press, 2017.

[10] Robert M Jones. *Mechanics of composite materials.* CRC Press, 1999.

[11] S. Ramakrishna. Microstructural design of composite materials for crashworthy structural applications. *Materials and Design*, 18(3):167–173, 1997.

[12] D. Hull. A unified approach to progressive crushing of fibre-reinforced composite tubes. *Composites Science and Technology*, 40:377–421, 1991.

[13] A.G. Mamalis, M. Robinson, D.E. Manolakos, G.A. Demosthenous, M.B. Ioannidis, and J. Carruthers. Review Crashworthy capability of composite material structures. *Composite Structures*, 37(1997):109–134, 1997.

[14] P.H. Thornton and P.J. Edwards. Energy absorption in composite tubes. *Journal of Composite Materials*, 16:521–545, 1982.

[15] Gary L. Farley. Effect of Specimen Geometry on the Energy Absorption Capability of Composite Materials. *Journal of Composite Materials*, 20(4):390–400, 1986.

[16] Kai Yang, Shanqing Xu, Shiwei Zhou, Jianhu Shen, and Yi Min Xie. Design of dimpled tubular structures for energy absorption. *Thin-Walled Structures*, 112:31–40, 2017.

[17] Saijod T.W. Lau, M. R. Said, and Mohd Yuhazri Yaakob. On the effect of geometrical designs and failure modes in composite axial crushing: A literature review. *Composite Structures*, 94(3):803–812, 2012.

[18] Ngoc San Ha and Guoxing Lu. Thin-walled corrugated structures: A review of crashworthiness designs and energy absorption characteristics. *Thin-Walled Structures*, 157, 2020.

[19] X. M. Xiang, G. Lu, and Z. You. Energy absorption of origami inspired structures and materials. *Thin-Walled Structures*, 157, 2020.

[20] Degao Hou, Yan Chen, Jiayao Ma, and Zhong You. Axial crushing of thin-walled tubes with kite-shape pattern. *Proceedings of the ASME 2015 International Design Engineering Technical Conferences & Computers and Information in Engineering Conference*, 2015.

[21] Jiayao Ma, Degao Hou, Yan Chen, and Zhong You. Quasi-static axial crushing of thin-walled tubes with a kite-shape rigid origami pattern: Numerical simulation. *Thin-Walled Structures*, 100:38–47, 2016.

[22] Shizhao Ming, Caihua Zhou, Tong Li, Zhibo Song, and Bo Wang. Energy absorption of thin-walled square tubes designed by kirigami approach. *International Journal of Mechanical Sciences*, 157-158:150–164, 2019.

[23] Hairui Wang, Chunfang Guo, Li Yujie, Yahua Liu, Minjie Wang, Zhong You, and Danyang Zhao. Structural design and forming method of single-curved surface structure based on Miura-origami. *Proceedings of the ASME 2016 International Design Engineering Technical Conferences & Computers and Information in Engineering Conference*, 2016.

[24] Hairui Wang, Danyang Zhao, Yifei Jin, Minjie Wang, Zhong You, and Guangrui Yu. Study of collapsed deformation and energy absorption of polymeric origami-based tubes with viscoelasticity. *Thin-Walled Structures*, 144, 2019.

[25] Haitao Ye, Jiayao Ma, Xiang Zhou, Hai Wang, and Zhong You. Energy absorption behaviors of pre-folded composite tubes with the full-diamond origami patterns. *Composite Structures*, 221, 2019.

[26] A. Ciampaglia, D. Fiumarella, C. Boursier Niutta, R. Ciardiello, and G. Belingardi. Impact response of an origami-shaped composite crash box: Experimental analysis and numerical optimization. *Composite Structures*, 256:113093, 2021.

[27] Zhibo Song, Shizhao Ming, Kaifan Du, Caihua Zhou, Yan Wang, Shengli Xu, and Bo Wang. Energy absorption of metal-composite hybrid tubes with a diamond origami pattern. *Thin-Walled Structures*, 180(August):109824, 2022.

[28] Shizhao Ming, Zhibo Song, Caihua Zhou, Kaifan Du, Chenghao Teng, Yan Wang, Shengli Xu, and Bo Wang. The crashworthiness design of metal/CFRP hybrid tubes based on origami-ending approach: Experimental research. *Composite Structures*, 279, 2022.

[29] Caihua Zhou, Bo Wang, Jiayao Ma, and Zhong You. Dynamic axial crushing of origami crash boxes. *International Journal of Mechanical Sciences*, 118:1–12, 2016.

[30] Jiayao Ma, Huaping Dai, Mengyan Shi, Lin Yuan, Yan Chen, and Zhong You. Quasi-static axial crushing of hexagonal origami crash boxes as energy absorption devices. *Mechanical Sciences*, 10(1):133–143, 2019.

[31] Kai Yang, Shanqing Xu, Jianhu Shen, Shiwei Zhou, and Yi Min Xie. Energy absorption of thin-walled tubes with pre-folded origami patterns: Numerical simulation and experimental verification. *Thin-Walled Structures*, 103:33–44, 2016.

[32] B. Kresling. Natural Twist Buckling in Shells: From the Hawkmoth's Bellows to the Deployable Kresling-Pattern and Cylindrical Miura-Ori. *6th International Conference on Computation of Shell & Spatial Structures (IASSIACM 2008)*, 2008.

[33] Antonio A. Deleo, James O'Neil, Hiromi Yasuda, Marco Salviato, and Jinkyu Yang. Origami-based deployable structures made of carbon fiber reinforced polymer composites. *Composites Science and Technology*, 191:108060, 2020.

[34] S.D. Guest and S. Pellegrino. The Folding of Triangulated Cylinders, Part I: Geometric Considerations. *Journal of Applied Mechanics*, 61:773–777, 1994.

[35] S.D. Guest and S. Pellegrino. The Folding of Triangulated Cylinders, Part II: The Folding Process. *Journal of Applied Mechanics*, 61:778–783, 1994.

[36] S.D. Guest and S. Pellegrino. The Folding of Triangulated Cylinders, Part III: Experiments. *Journal of Applied Mechanics*, 63:77–83, 1996.

[37] Hiromi Yasuda and Jinkyu Yang. The International Association for Shell and Spatial. 56(3):185–198, 2017.

[38] Kangfan Yu, Yunwei Chen, Chuanyun Yu, Pan Li, Zihao Ren, Jianrun Zhang, and Xi Lu. Origami-inspire quasi-zero stiffness structure for flexible low-frequency vibration isolation. *International Journal of Mechanical Sciences*, 276, 2024.

[39] Cai Jianguo, Deng Xiaowei, Zhou Ya, Feng Jian, and Tu Yongming. Bistable behavior of the cylindrical origami structure with kresling pattern. *Journal of Mechanical Design, Transactions of the ASME*, 137, 2015.

[40] Hiromi Yasuda, Koshiro Yamaguchi, Yasuhiro Miyazawa, Richard Wiebe, Jordan R. Raney, and Jinkyu Yang. Data-driven prediction and analysis of chaotic origami dynamics. *Communications Physics*, 3(1), 2020.

[41] Lee Wilson, Sergio Pellegrino, and Rolf Danner. Origami Sunshield Concepts for Space Telescopes. *54th AIAA/ASME/ASCE/AHS/ASC Structures, Structural Dynamics, and Materials Conference*, 2013.

[42] C. Jianguo, D. Xiaowei, Z. Yuting, F. Jian, and Z. Ya. Folding behavior of a foldable prismatic mast with Kresling origami pattern. *Journal of Mechanisms and Robotics*, 8(3), 2016.

[43] Ji Zhang and Changguo Wang. Deployment behavior and mechanical property analysis of kresling origami structure. *Composite Structures*, 341, 2024.

[44] Hiromi Yasuda, Tomohiro Tachi, Mia Lee, and Jinkyu Yang. Origami-based tunable truss structures for non-volatile mechanical memory operation. *Nature Communications*, 8(1), 2017.

[45] Hui Yun Hwang. Effects of perforated crease line design on mechanical behaviors of origami structures. *International Journal of Solids and Structures*, 230-231:111158, 2021.

[46] Mojtaba Moshtaghzadeh, Ehsan Izadpanahi, and Pezhman Mardanpour. Prediction of fatigue life of a flexible foldable origami antenna with Kresling pattern. *Engineering Structures*, 251(113399), 2022.

[47] Z. Wu, I. Hagiwara, and X. Tao. A Consideration of Function and Design for Application Using Origami Structure and Subdivision Technology. *Dynamics and Design Conference*, (4-5), 2004.

[48] Z. Wu, I. Hagiwara, and X. Tao. Optimisation of crush characteristics of the cylindrical origami structure. *International Journal of Vehicle Design*, 43(1/2/3/4):66, 2007.

[49] Xilu Zhao, Yabo Hu, and Ichiro Hagiwara. Shape Optimization to Improve Energy Absorption Ability of Cylindrical Thin-Walled Origami Structure. 5(3):148–162, 2011.

[50] J. Li, Y. Chen, X. Feng, J. Fend, and P. Sareh. Computational modeling and energy absorption behavior of thin-walled tubes with the Kresling origami pattern. *Journal of the International Association for Shell and Spatial Structures*, pages 71–81, 2021.

[51] C. H. Kong, X. L. Zhao, and I. R. Hagiwara. A new local thickening reverse spiral origami thin-wall construction for improving of energy absorption. *IOP Conference Series: Materials Science and Engineering*, 307(1), 2018.

[52] Xilu Zhao and Ichiro Hagiwara. Designing and manufacturing a super excellent and ultra-cheap energy absorber by origami engineering. *Proceedings of the ASME 2019 International Design Engineering Technical Conferences and Computers and Information in Engineering Conference*, 2019.

[53] Shiming Wang, Yong Peng, Tiantian Wang, Xuanzhen Chen, Lin Hou, and Honghao Zhang. The origami inspired optimization design to improve the crashworthiness of a multi-cell thin-walled structure for high speed train. *International Journal of Mechanical Sciences*, 159:345–358.

[54] Fibertow. `https://www.fibreglast.com/product/24K_Carbon_Tow_2293`, 2021. Accessed: 2021-05-07.

[55] Moisture-resistant polyester film. `https://www.mcmaster.com/8567K94/`, 2021. Accessed: 2021-05-07.

[56] Resin. https://www.fibreglast.com/product/System_2000_Epoxy_Resin_2000, 2021. Accessed: 2021-05-07.

[57] A. Esnaola, B. Elguezabal, J. Aurrekoetxea, I. Gallego, and I. Ulacia. Optimization of the semi-hexagonal geometry of a composite crush structure by finite element analysis. *Composites Part B: Engineering*, 93:56–66, 2016.

[58] J.C. Halpin. Effects of environmental factors on composite materials. *AFML TR 67-423*, 1969.

[59] J.C. Halpin and J.L. Kardos. The Halpin-Tsai Equations: A Review. *Polymer Engineering and Science*, 16(5), 1976.

[60] Zhengdong Han, Huaguan Li, Xiaocun Xu, Hao Wang, Hongli Li, and Jie Tao. Crushing characteristics of aluminum/CFRP/aluminum hybrid tubes prepared by spinning forming. *Composite Structures*, 249:112551, 2020.

[61] Z.P. Bažant and B.H. Oh. Crack band theory for fracture of concrete. *Matériaux et construction*, 16(3):155–177, 1983.

[62] M. Salviato, K. Kirane, S.E. Ashari, Z.P. Bažant, and G. Cusatis. Experimental and numerical investigation of intra-laminar energy dissipation and size effect in two-dimensional textile composites. *Composites Science and Technology*, 135:67–75, 2016.

[63] M. Salviato, S.E. Ashari, and G. Cusatis. Spectral stiffness microplane model for damage and fracture of textile composites. *Composite Structures*, 137:170–184, 2016.

[64] K. Kirane, M. Salviato, and Z.P. Bažant. Microplane-triad model for elastic and fracturing behavior of woven composites. *Journal of Applied Mechanics*, 83(4), 2016.

[65] M. Salviato, K. Kirane, Z.P. Bažant, and G. Cusatis. Mode I and II interlaminar fracture in laminated composites: a size effect study. *Journal of Applied Mechanics*, 86(9), 2019.

[66] Gang Zheng, Zhen Wang, and Kai Song. Energy absorption on metal-composite hybrid structures: Experimental and numerical simulation. *Thin-Walled Structures*, 150, 2020.

[67] Sandhya Gupta, Kananbala Sharma, and NS Saxena. Temperature dependent mechanical analysis of chalcogenide (cds, zns) coated pet films. *International Scholarly Research Notices*, 2013, 2013.

[68] F. Djamaluddin, S. Abdullah, A. K. Ariffin, and Z. M. Nopiah. Optimization of foam-filled double circular tubes under axial and oblique impact loading conditions. *Thin-Walled Structures*, 87:1–11, 2015.

[69] Sukhvarsh Jerath. *Structural stability theory and practice: buckling of columns, beams, plates, and shells*. John Wiley & Sons, 2020.

[70] James O'Neil, Marco Salviato, and Jinkyu Yang. Energy Absorption Behavior of Filament Wound CFRP Origami Tubes Pre-folded in Kresling Pattern. *Composite Structures*, 304:116376, 2023.

[71] Hiromi Yasuda, Yasuhiro Miyazawa, Efstathios G. Charalampidis, Christopher Chong, Panayotis G. Kevrekidis, and Jinkyu Yang. Origami-based impact mitigation via rarefaction solitary wave creation. *Science Advances*, pages 1–9, 2019.

[72] Eun Ho Kim, In Lee, and Tae Kyung Hwang. Low-velocity impact and residual burst-pressure analysis of cylindrical composite pressure vessels. *AIAA Journal*, 50(10):2180–2193, 2012.

[73] Eun Ho Kim, Mi Sun Rim, In Lee, and Tae Kyung Hwang. Composite damage model based on continuum damage mechanics and low velocity impact analysis of composite plates. *Composite Structures*, 95:123–134, 2013.

[74] Performance Composites LTD. *Mechanical Properties of Carbon Fibre Composite Materials, Fibre / Epoxy resin (120°C Cure)*.

[75] Donghyun Yoon, Sangdeok Kim, Jaehoon Kim, and Youngdae Doh. Prediction of failure behavior for carbon fiber reinforced composite bolted joints using progressive failure analysis. *Composites Research*, 34:101–107, 2021.

[76] C. Bisagni. Numerical analysis and experimental correlation of composite shell buckling and post-buckling. *Composites: Part B*, 31:655–667, 2000.

[77] Mark W Hilburger and James H Starnes. Effects of imperfections on the buckling response of compression-loaded composite shells. *International Journal of Non-Linear Mechanics*, 37:623–643, 2002.

[78] M. Broggi and G. I. Schuëller. Efficient modeling of imperfections for buckling analysis of composite cylindrical shells. *Engineering Structures*, 33:1796–1806, 2011.

[79] Jendi Kepple, Manudha Herath, Garth Pearce, Gangadhara Prusty, Rodney Thomson, and Richard Degenhardt. Improved stochastic methods for modelling imperfections for buckling analysis of composite cylindrical shells. *Engineering Structures*, 100:385–398, 2015.

[80] Manuel Stein and John A McElman. Buckling of segments of toroidal shells. *AIAA Journal*, 3(9):1704–1709, 1965.

[81] John W Hutchinson. Initial post-buckling behavior of toroidal shell segments. *International Journal of Solids and Structures*, 3(1):97–115, 1967.

[82] Haluk Yilmaz and Ibrahim Kocabas. Elastic limit load prediction and equivalent cylinder proposal for circular concave shells subjected to axial compression. *Thin-Walled Structures*, 159, 2021.

[83] Robert Millard Jones. *Buckling of bars, plates, and shells.* Bull Ridge Corporation, 2006.

[84] Ahmad Baroutaji, Arun Arjunan, Gurpal Singh, and John Robinson. Crushing and energy absorption properties of additively manufactured concave thin-walled tubes. *Results in Engineering*, 14(100424), 2022.

[85] Qiaoguo Wu, Lei Zu, Qian Zhang, Guiming Zhang, Shijun Chen, Huabi Wang, Debao Li, and Honghao Liu. Filament winding analysis and experimental verification of a combined revolution body with a concave surface. *Composite Structures*, 280, 2022.

[86] Fibre Glast. *System 2000 Laminating Epoxy Resin*, 2020.

[87] Prescilla Christy Albert, Amir Radzi Ab Ghani, Mohd Zaid Othman, and Ahmad Mujahid Ahmad Zaidi. Axial Crushing Behavior of Aluminum Square Tube with Origami Pattern. *Modern Applied Science*, 10(2):90–108, 2016.

[88] Peter Azor Okorugbo, Ali Evcil, Mehmet Ali Guler, and Mahmut A. Savas. Investigation of the effect of impact velocity on the energy absorption characteristics of crash boxes. *3rd International Symposium on Multidisciplinary Studies and Innovative Technologies, ISMSIT 2019 - Proceedings*, pages 1–7, 2019.

[89] Jinbong Kim, Mungyu Jeong, Holger Böhm, Jonas Richter, and Niels Modler. Experimental investigation into static and dynamic axial crush of composite tubes of glass-fiber mat/pa6 laminates. *Composites Part B: Engineering*, 181, 2020.

Appendix A

MORE EXPERIMENTAL AND NUMERICAL RESULTS FOR CFRP TUBES

A.1 Superimposed Force-Displacement Plots

To obtain a better visualization of how the experimental responses of the conventional tubes compare, their force-displacement curves are superimposed in Figure A.1a. The experimental force-displacement responses of the Kresling origami tubes are superimposed in Figure A.1b.

The numerical compression results for the conventional tubes are superimposed together in Figure A.1c. We also superimpose the numerical plots of the Kresling origami tubes in Figure A.1d. Besides larger initial peaks from the conventional tubes and some qualitative differences in the Kresling origami responses, the numerical model predicts the experimental trends satisfactorily.

A.2 Final Numerical Deformations

Figures A.2a-b depict the final deformations for both conventional tubes with side- and top-views as well as a legend showing the max in-plane principal stresses. Figures A.3a-c provide the same information for the simulated Kresling origami tubes. Most notable for the Kresling origami tubes is that the maximum in-plane principal stresses also remain in the creases or in the bottom facets that are in a bending state.

A.3 Specific Energy Absorption with Mandrel Mass

In the main text, we showed results for the specific energy absorption for all of the tubes without accounting for the mandrel mass. Figures A.4a and A.4b show the variations of the specific energy absorption for each tube based on experimental and numerical results respectively with the mandrel mass accounted for. Only the conventional tubes show qualitative difference in their numerical plots when compared to the specific energy absorption plots without the mandrel mass accounted for. Between 45-60 mm, the circular and square SEA plots intersect twice when the mandrel mass is not accounted for. Numerically, the mandrel mass of the circular tube was 36.7% of the total mass while the mandrel mass of the square tube was 32.7%. Therefore, when the mandrel masses were not accounted for, the circular tube's SEA increased more than the square tube's SEA resulting in the intersection.

The final specific energy absorption values accounting for the mandrel mass are presented in Figure A.4c. We see the same qualitative results as in the bar plot of specific energy absorption not accounting for the mandrel mass. In both versions of the SEA, the Kresling origami tubes do not gain an advantage in terms of specific energy absorption throughout the compression of the tubes. On average, the specific energy absorption for the manufactured tubes increases by approximately 48% when the mandrel mass is not accounted for. Numerically, this value is about 44%.

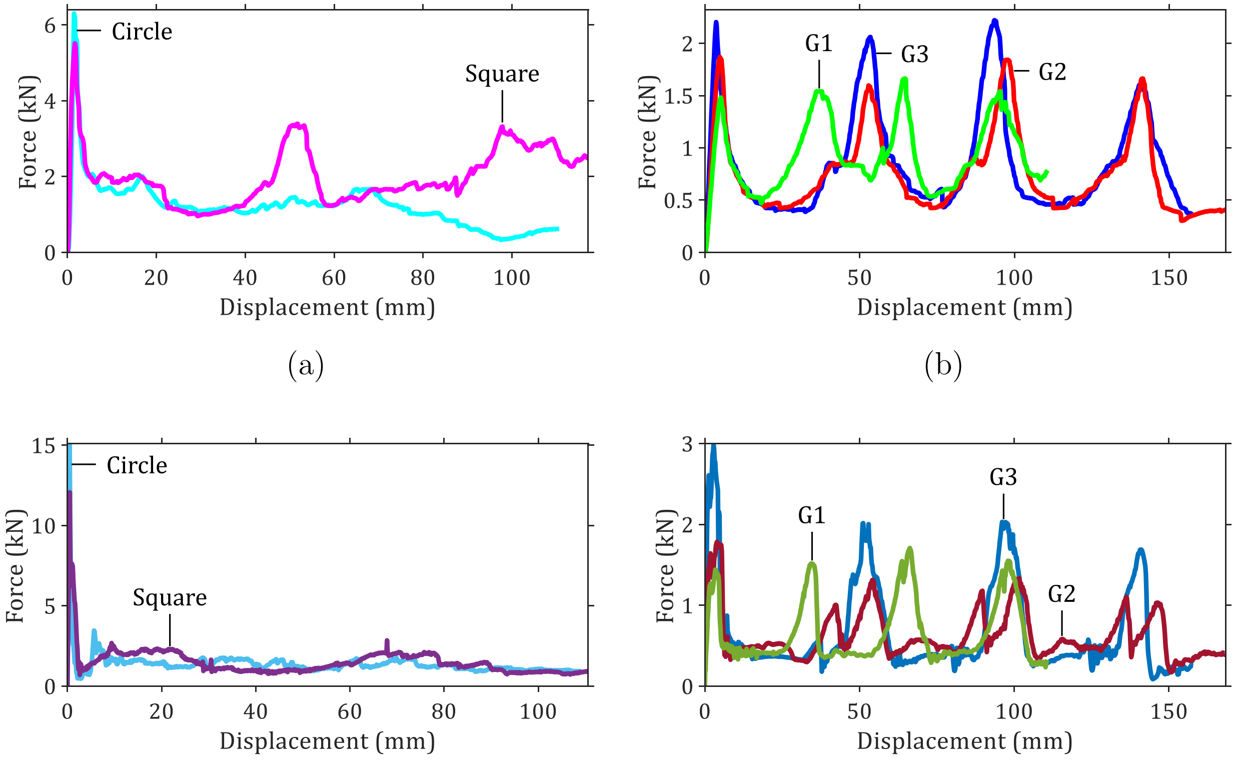

(a) (b)

(c) (d)

Figure A.1: (a) and (b) are the experimental force-displacement plots of the conventional tubes superimposed together and the Kresling origami tubes superimposed together respectively. (c) and (d) are the numerical force-displacement plots of the conventional tubes superimposed together and the Kresling origami tubes superimposed together respectively.

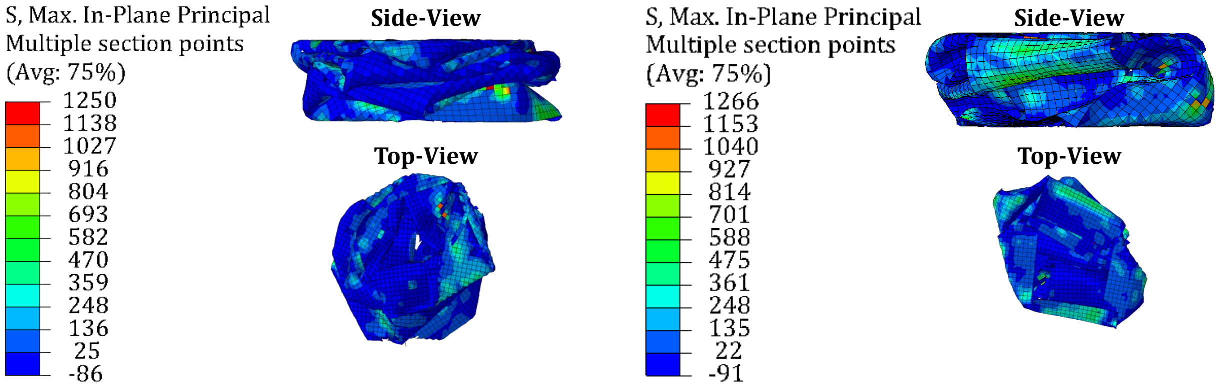

(a) (b)

Figure A.2: Final numerical deformations for: a) The tube with the circular cross-section and b) the tube with the square cross-section. Stresses are in units of MPa.

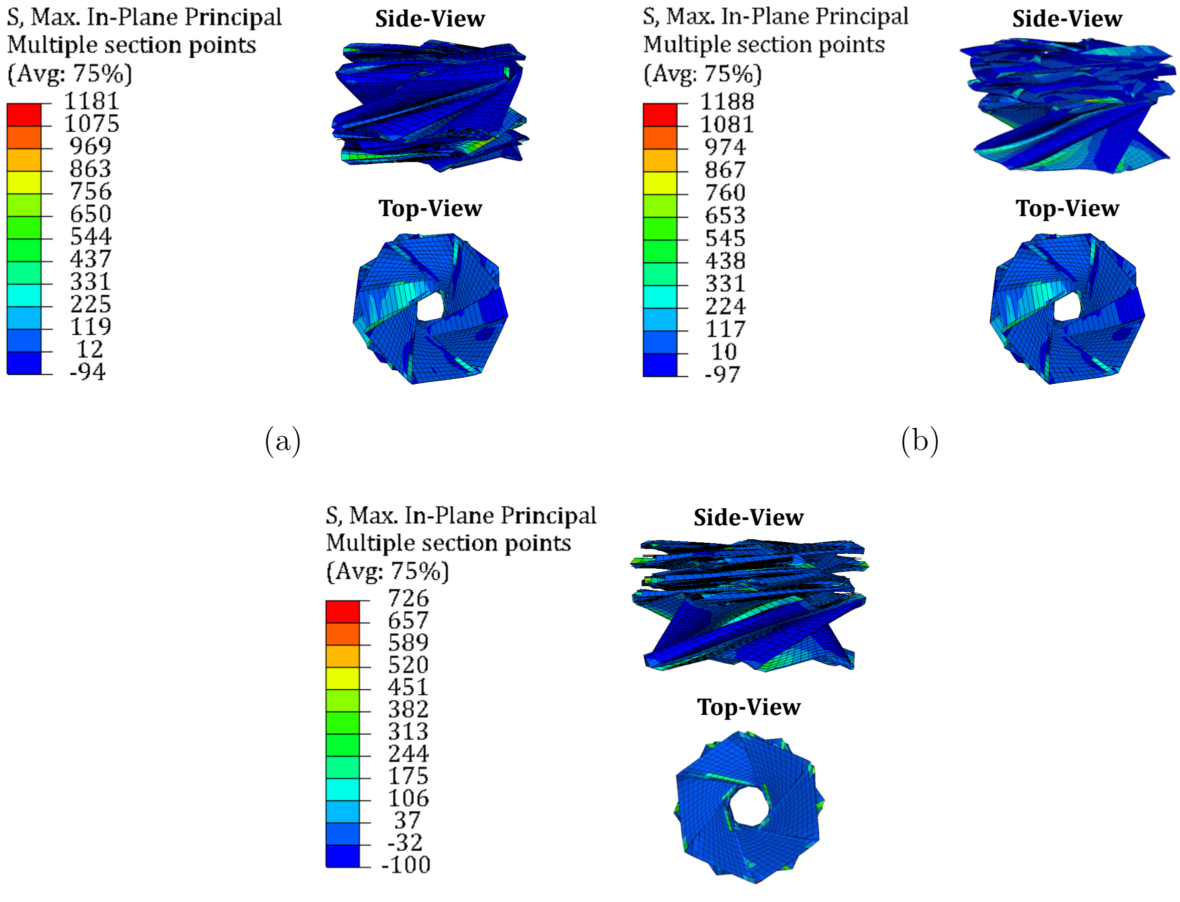

(a) (b) (c)

Figure A.3: Final numerical deformations for: a) G1, b) G2, and c) G3. Stresses are in units of MPa.

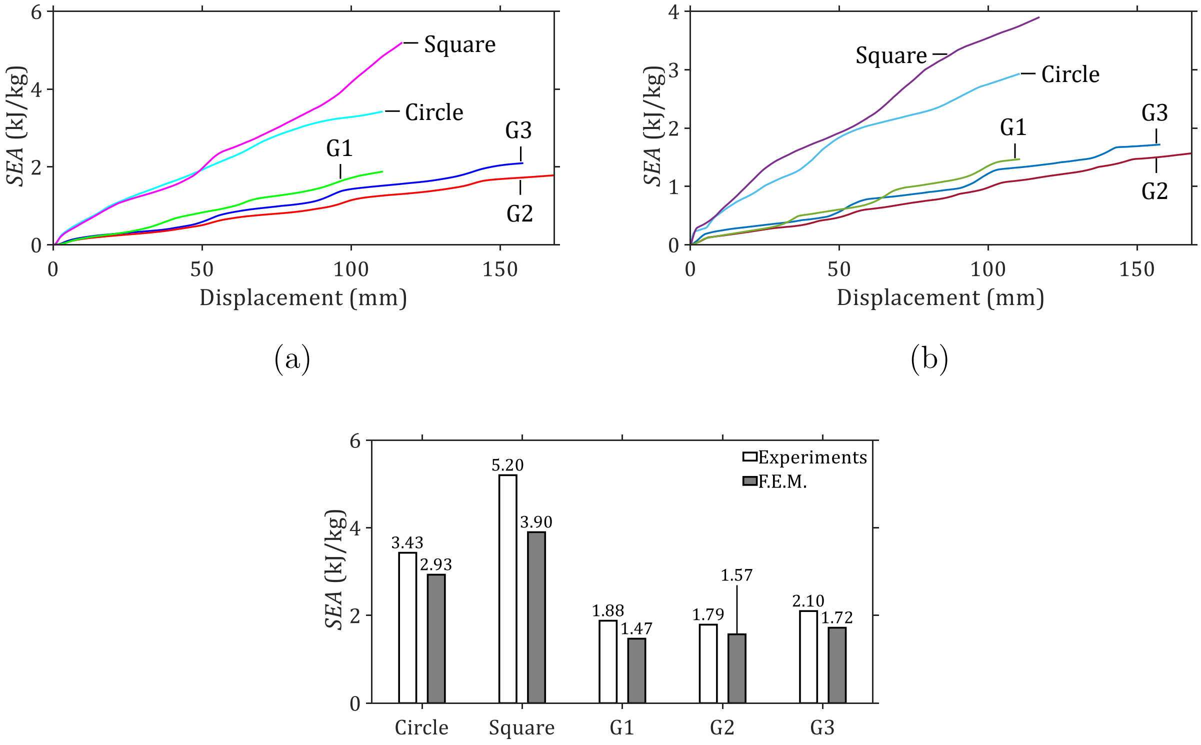

(a)

(b)

(c)

Figure A.4: (a) and (b) show the variation of the specific energy absorption accounting for the full mass of the tubes from experimental and numerical results respectively. (c) shows a comparison of the final SEA for all tubes both experimentally and numerically.

Appendix B

ADDITIONAL PARAMETRIC STUDY DETAILS AND RESULTS

B.1 Manufacturing

We utilize the same filament winding techniques described in O'Neil [70] to fabricate the CFRP tubes in this study. As in O'Neil [70], a 0.254 mm thick PET[55] mandrel is folded and then closed with double-sided tape (Scotch® Permanent) applied at the bonding regions. Additionally, a mandrel is coated with the double-sided tape to avoid fiber slipping during a layup. Additional details of the mandrel preparation can be found in O'Neil [70]. Note that the fabricated mandrels initially start with an additional two unit cells, one on each end of the tube. These will be removed after the tube is cured and are there to ensure fibers are properly aligned at the ends of the tube and allow us to secure fibers with masking tape.

The layup of our tubes is shown in Figure B.1. As shown the carbon fibers [54] are aligned parallel to valley creases on the PET mandrel. The valley creases represent the 1-direction within a given facet. A layer of fibers is wrapped around the tube and secured with masking tape. The fibers are coated with a room-temperature epoxy resin [56] and another layer of fibers are wrapped around the tube and secured in the same way as before. The fiber layer is then coated with more epoxy resin and the tube is placed in an oven for six hours. The tube is rotated during this time as explained in O'Neil [70]. After curing is finished, the tube is allowed to cool down and sit outside of the oven for twelve hours. The unit cells at the ends of the tube are removed with a wet tile saw. At this point the tube is ready to be compressed.

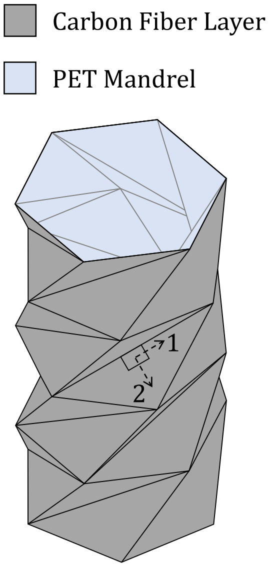

Figure B.1: A schematic of the components of the Kresling tubes: the PET mandrel and the carbon fiber layer of the walls. The fiber orientation 1- is also labelled here with the perpendicular direction being labelled as 2-.

B.2 Mass Data

We provide information about the masses of all tubes tested in each study here. The masses of the thin-walled cylinders that the Kresling origami tubes are compared to are given shown in Figure B.2.

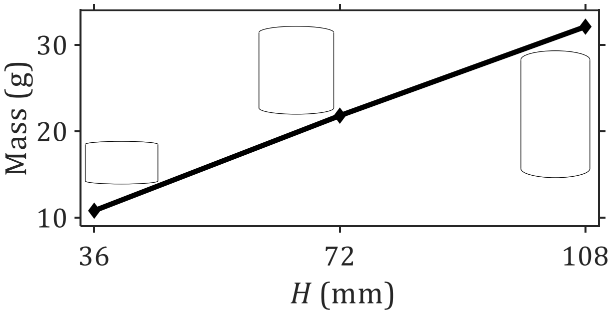

Figure B.2: **Mass curves for the tested cylinders in this investigation.** Insets showing the geometry of each tube are provided.

B.2.1 β and H_{unit} Study

The masses of the experimentally tested tubes in the β and H_{unit} studies are provided in Figure B.3 where they are also compared with their numerical counterparts. The masses of the numerical tubes are smaller than the fabricated tubes due to the PET not having exactly the same thickness in the fabricated tubes as well as the composite walls having a reduced thickness to account for thickness imperfections. It should be noted as well that the fabricated $\beta = 20°$ tube is greater than the other tubes due to having a slightly greater thickness than the other tubes. It maintained more of its excess resin during curing.

The masses of all of the numerical tubes in the β and H_{unit} study are provided in Figure B.4. As the unit cell twist angle increases, so does its total surface area which increases its mass.

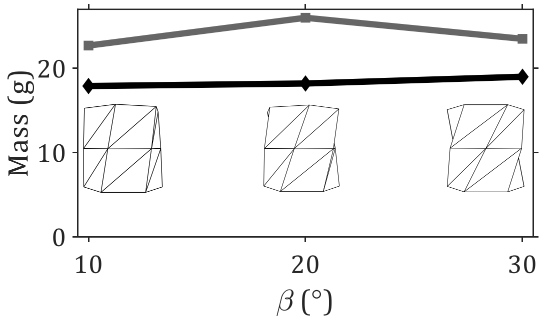

Figure B.3: **Mass curves for the tested Kresling origami tubes in the β and H_{unit} study.** The masses of the experimentally tested tubes (gray curve) are compared with the numerical versions (black curve) of the tube. Insets showing the geometry of each tube are provided.

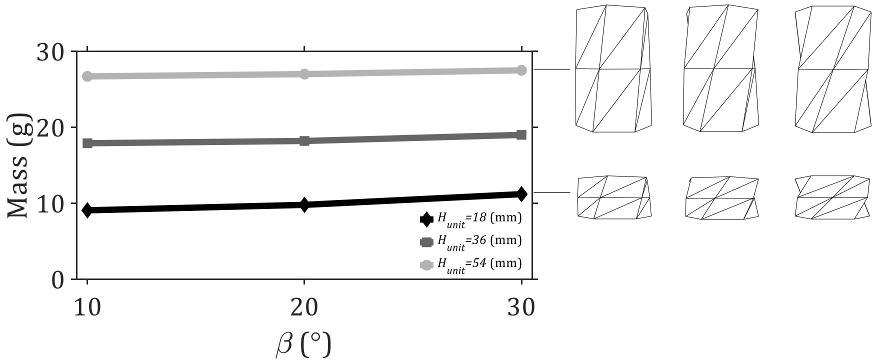

Figure B.4: **Mass curves of all of the numerical Kresling origami tubes in the β and H_{unit} study.** The masses of all of the numerical Kresling origami tubes are shown and compared. Insets showing the geometry of each tube are provided.

B.2.2 n Study

The masses of the tubes in the varying n study are given in Figure B.5.

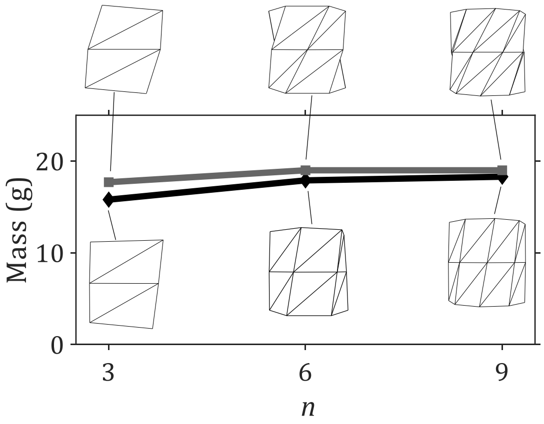

Figure B.5: **Mass curves for the Kresling origami tubes in the n study.** Insets showing the geometry of each tube are provided.

B.2.3 N Study

All of the Kresling origami tubes tested in the N study, both the varying and constant twist rate cases, have their masses plotted in Figure B.6. We see an increase in the mass in the varying twist rate case because as the overall twist rate of the tube increases, so does its surface area. The constant twist rate case does not change much since the surface area is not changing, only the thickness from unit cell to unit cell.

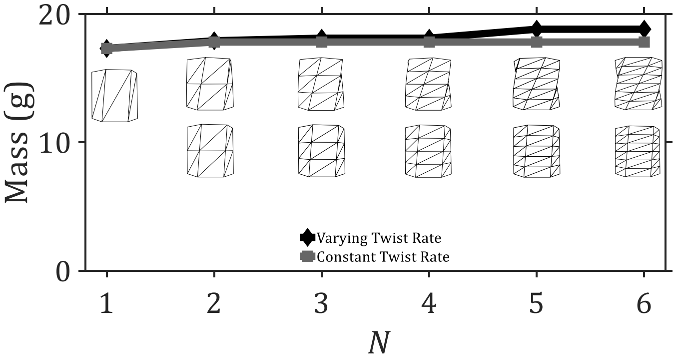

Figure B.6: **Numerical mass curves for Kresling origami tubes with varying N.** (a) The twist rate of the whole tube changes since $\beta = 10°$. (b) The twist rate of the whole tube is constant since $\beta = \frac{10}{N}$ (°). In both cases, $H_{unit} = 72/N$ (mm). In the first case, the mass increases as more unit cells are added. In the second case, the mass does not vary.

Appendix C

NON-UNIFORM KRESLING TUBE FOLD PATTERN

Figure C.1 depicts the fold patterns necessary for both versions of the Kresling origami tubes studied in this paper. In this study, we manufacture polyethylene terephthalate (PET) mandrel by following these fold patterns. They are cut from PET sheets using a laser cutter. Double-sided tape is applied at the bonding regions which closes the tube and forms the volumetric form of Kresling. Double-sided tape is applied around the mandrel and one layer of fibers is wrapped around the tube. If the tube has uniform unit cell geometry, the first fiber layer is wrapped parallel to the valley creases. If the tube has non-uniform unit cell geometry, the first layer is wrapped 20° off of the valley creases. The first fiber layer is then wetted with resin. The second fiber layer is wrapped parallel to the valley creases. Resin is applied one more time to the tube and then it is cured in an oven while being rotated periodically. After cooling for a day, the two ends of the tube are removed with a wet tile saw and the tube is ready for testing.

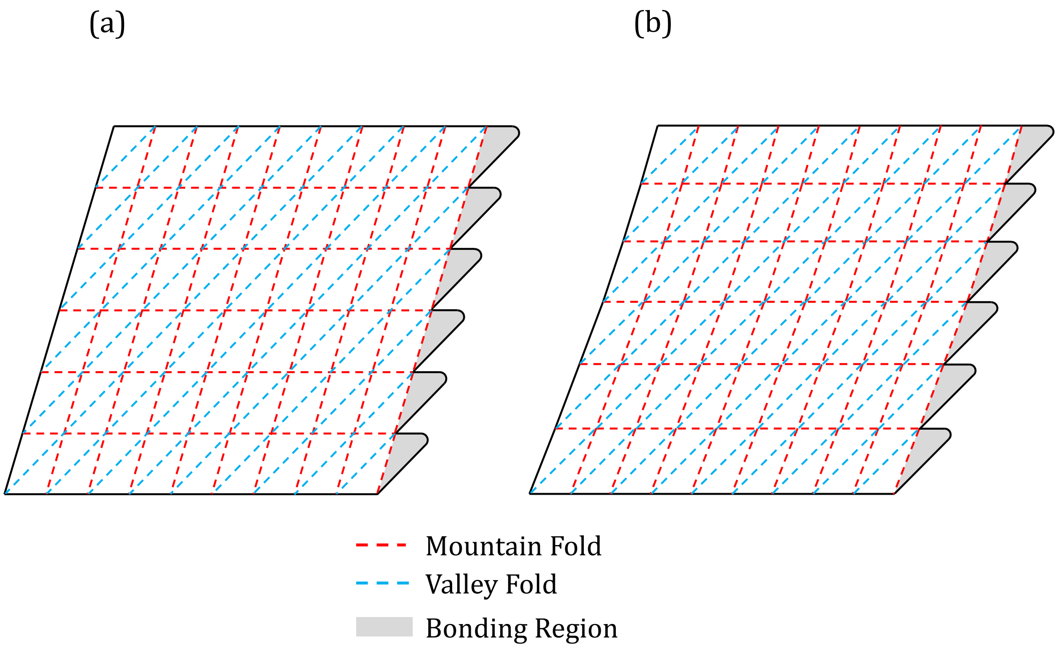

Figure C.1: **Fold patterns of the Kresling origami tubes in this investigation.** (a) Fold pattern for uniform unit cell tubes. (b) Fold pattern for the nonuniform unit cell tube.